Universidade de São Paulo
Instituto de Física

Restrições sobre a gravidade de Horndeski a partir do sinal de 21-cm

Daniel Souza Correia

Orientador: Prof. Dr. Elcio Abdalla

Dissertação de mestrado apresentada ao Instituto de Física da Universidade de São Paulo, como requisito parcial para a obtenção do título de Mestre em Ciências.

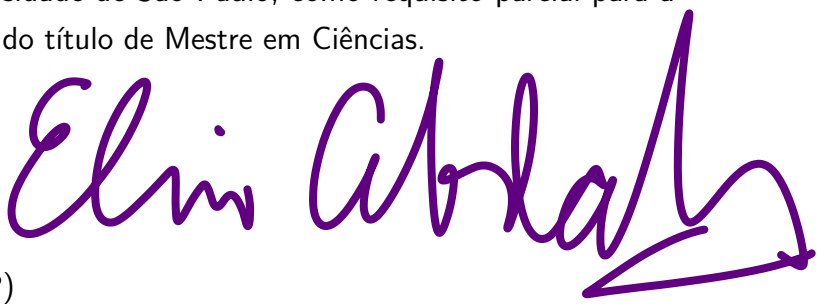

Banca Examinadora:
Prof. Dr. Elcio Abdalla - Orientador (IFUSP)
Prof. Dr. José Ademir Lima (IAG-USP)
Prof. Dr. Alberto Vazquez Saa (UNICAMP)

São Paulo
2022

FICHA CATALOGRÁFICA
Preparada pelo Serviço de Biblioteca e Informação do Instituto de Física da Universidade de São Paulo

Correia, Daniel Souza

Restrições sobre a gravidade de Horndeski a partir do sinal de 21-cm. São Paulo, 2022.

Dissertação (Mestrado) – Universidade de São Paulo. Instituto de Física. Depto. de Física Geral

Orientador: Prof. Dr. Elcio Abdalla

Área de Concentração: Física

Unitermos: 1. Cosmologia; 2. Teorias de Horndeski; 3. Linha de 21-cm do Hidrogênio;

USP/IF/SBI-028/2022

University of São Paulo
Physics Institute

Constraints on Horndeski gravity from the 21-cm signal

Daniel Souza Correia

Supervisor: Prof. Dr. Elcio Abdalla

Dissertation submitted to the Physics Institute of the University of São Paulo in partial fulfillment of the requirements for the degree of Master of Science.

Examining Committee:
Prof. Dr. Elcio Abdalla - Supervisor (IFUSP)
Prof. Dr. José Ademir Lima (IAG-USP)
Prof. Dr. Alberto Vazquez Saa (UNICAMP)

São Paulo
2022

Acknowledgements

Ao Prof. Dr. Elcio Abdalla, pela proposta do projeto de pesquisa e pela orientação; ao Prof. Dr. Filipe Abdalla, por ter coorientado a pesquisa;

Aos colaboradores do projeto BINGO, pelas proveitosas discussões. Em especial, Gabriel Hoerning, Pablo Motta, e Rafael Ribeiro pela ajuda com os códigos; Ricardo Landim e Camila Novaes pelas dicas e sugestões nas reuniões do grupo de Cls; Gustavo Silva e Juliana Fernandes pela colaboração com algumas análises nos estudos da gravitação modificada;

À equipe de professores dos Laboratórios de Física 1 e 2, Dr. Alexandre Correia, Dr. José Chubaci, Dr. Marco Bregant, Dr. Raphael Liguori, e Dr. Zwinglio Guimarães pelo aprendizado nesses dois anos;

Às secretárias Bianca, Edineusa e Fátima pelo suporte na transição para o Departamento de Física Geral, e aos meus colegas de sala, Júlio Costa e Leonardo Werneck;

Ao Laboratório Nacional de Computação Científica, pela disponibilização de alguns recursos do supercomputador Santos Dumont;

Aos amigos presentes nas diferentes fases dessa pesquisa: Antônio Ferreira, Cheick Doumbia, Daniel Moitinho, Eder Huamani, Edwin Larico, Herculano da Silva, Ivo Aloide Ié, Leandro Franco e Nathália Pinheiro. À Francieli Lopes, pelas palavras de incentivo e conversas;

À minha família: Maria da Conceição Luzia, Gabriel Correia, Bárbara Daniela Correia, e Aroldo Luzia, pelo apoio durante todos esses anos.

Resumo

Nesta dissertação, estudamos as teorias de Horndeski, uma forma de Gravitação Modificada (MG), alternativa à Relatividade Geral (GR), que tem o propósito de explicar a recente expansão acelerada do universo. Predições de medidas de parâmetros cosmológicos foram realizadas a partir de mapas de 21-cm, planejadas para serem feitas em breve pelo radiotelescópio BINGO. Tais mapas foram gerados a partir de espectros de potência angulares teóricos, calculados levando em conta a cosmologia do WMAP5, e definindo o bias e o parâmetro de densidade do hidrogênio neutro a partir de simulações de N-corpos. Inicialmente, estabelecemos vínculos cosmológicos para uma subclasse de Horndeski em que as ondas gravitacionais (GWs) se propagam à velocidade da luz. A partir do sinal de 21-cm, não encontramos um desvio significativo da GR para ambas as parametrizações utilizadas. Considerando os dados de CMB, os valores dos parâmetros cosmológicos da MG se reduzem em uma ordem 10, sendo a constante de Hubble e o parâmetro de matéria escura fria compatíveis com aqueles do WMAP5. As medidas com os dados combinados (BINGO+CMB) fornecem as melhores estimativas dos parâmetros. Para uma classe mais geral de Horndeski, em que se permite a variação do parâmetro que descreve o desvio da velocidade das GWs, os dados (BINGO+CMB) indicam que as mesmas se propagam a uma velocidade abaixo da velocidade da luz, de acordo com previsões teóricas.

Palavras-chaves: Cosmologia. Energia Escura. Teorias de Horndeski. BINGO. Hidrogênio Neutro.

Abstract

In this dissertation, we study the Horndeski theories, a form of Modified Gravity (MG), alternative to General Relativity (GR), that has the purpose of explaining the recent accelerated expansion of the universe. We forecast measurements of cosmological parameters from the 21-cm signal, planned to be made soon by BINGO radiotelescope. Such maps were built from theoretical angular power spectrum, computed taking into account the WMAP5 cosmology, and defining the bias and the neutral hydrogen energy density from N-body simulations. Initially, we placed constraints on a sub-class of Horndeski with luminally propagating gravitational waves (GWs). From the 21-cm signal, we did not find a significant departure from GR for both α_i parameterizations. Considering the CMB data, the MG parameters are reduced to 10^{-1} order, and we recovered the Hubble constant and the cold dark matter energy density, measured by WMAP5 experiment. The parameter measurements with the combined data (BINGO+CMB) provide the best estimates. Finally, for a more general class of Horndeski in which the tensor speed excess is allowed to vary, the dataset BINGO+CMB favour sub-luminal propagating GWs, as predicted theoretically.

Keywords: Cosmology. Dark Energy. Horndeski Theories. BINGO. Neutral Hydrogen.

List of Figures

List of Tables

List of abbreviations and acronyms

ADM	Arnowitt-Deser-Misner
BAO	Baryon Accoustic Oscillations
BBN	Big Bang Nucleosynthesis
BINGO	BAO from Integrated Neutral Gas Observations
CAMB	Code for Anisotropies in the Microwave Background
CDM	Cold Dark Matter
CLASS	Cosmological Linear Anisotropy Solving System
CL	Confidence Level
CMB	Cosmic Microwave Background
CP	Charge Parity
DE	Dark Energy
DM	Dark Matter
EFT	Effective Field Theory
EW	Electroweak Interaction
FLASK	Full-sky Lognormal Astro-fields Simulation Kit
FLRW	Friedman-Lemaitre-Robertson–Walker
GR	General Relativity
GW	Gravitational Wave
HAM	Halo Abundance Matching
HI	Neutral Hydrogen
HI_CLASS	Horndeski in the Cosmological Linear Anisotropy Solving System
HIR4	Horizon Run 4
HOD	Halo Occupation Distribution
IGM	Intergalactic Medium
IM	Intensity Mapping
ISW	Integrated Sachs–Wolfe
LHC	Large Hadron Collider
LRG	Luminous Red Galaxies
LSS	Large-Scale Structure
MCMC	Monte Carlo Markov Chain
MG	Modified Gravity
QS	Quasi-Static
RSD	Redshift-Space Distortions
SDSS	Sloan Digital Sky Survey
SNIa	Supernova Type Ia
SW	Sachs–Wolfe
UCLC_l	Unified Cosmological Library for C_l
WIMP	Weakly Interacting Massive Particle
WL	Weak Lensing
WMAP	Wilkinson Microwave Anisotropy Probe

Contents

Introduction

One of the greatest challenges that remain in modern physics is to explain the recent accelerated expansion of the universe. This fact was first detected by Supernova Type Ia (SNIa) observations in the late 1990s [1, 2], and later confirmed by many independent observations such as temperature anisotropies of the Cosmic Microwave Background (CMB) [3], Baryon Acoustic Oscillations (BAO) [4], etc. Within the framework of General Relativity (GR), the simplest explanation to the cosmic acceleration demands the existence of Dark Energy (DE), an unusual new matter component, whose physical properties lead to repulsive gravity. In fact, the observational data seem to favor the Λ-Cold Dark Matter (ΛCDM) model, which assigns the cosmological constant, Λ, as the origin of DE, corresponding to most of the cosmic budget ($\sim$68%).

The ΛCDM model also describes the baryonic matter content ($\sim$5%) according to the standard model of Particle Physics, and accounts for another unknown dark component called Dark Matter (DM) ($\sim$27%). DM is a non-baryonic form of matter proposed to explain the observed rotation galaxies curves, greater than the expected one by classical mechanics [5], and has as particle candidates Weakly Interacting Massive Particles (WIMPs), axions, sterile neutrinos, and others, which were not detected so far. Although ΛCDM gives a great description of the universe, the model is not satisfactory: it presents an unnatural value for the cosmological constant, smaller than Particle Physics predictions by $\sim$121 order of magnitude; furthermore, an observational tension among different datasets emerge in this model on the value of the Hubble constant, showing, for instance, a 4.4σ discrepancy with Planck satellite from local measurements [6].

Such shortcomings have lead the search for new physics beyond the standard model: instead of a cosmological constant, the cosmic acceleration is driven by an exotic matter species, or even by modifications to GR itself on large scales. Following the latter, such Modified Gravity (MG) proposals are actually departures from GR made by invoking Lovelock's theorem [7]. The simplest modification to Einstein's theory is the introduction of a scalar field in the Einstein-Hilbert action, adding an extra dynamical degree of freedom in equations. Horndeski theories provide the most general scalar-tensor modification to gravity that does not suffer from theoretical instabilities, with the scalar field playing the role of DE [8–10]. As such, the cost of altering GR via Horndeski theories is the modification of how fast structures grow, which can be measured in a model-independent manner at the level of linear perturbation theory.

A promising survey of Large-Scale Structure (LSS) is BAO from Integrated Neutral Gas

Observations (BINGO) radiotelescope, which will soon provide a robust dataset that can be used, among others goals, to place bounds on MG theories such as Horndeski [11–17]. BINGO will map the Neutral Hydrogen (HI) over the redshift range $z = 0.127 - 0.449$ through a technique called Intensity Mapping (IM). In this work, we forecast cosmological parameters measurements from BINGO data by building 21-cm maps from theoretical angular power spectra, computed taking into account the fiducial values from WMAP5 experiment, and defining the bias and the density parameter of HI, Ω_{HI}, from the Horizon Run 4 (HIR4) mock [16]; the covariance matrix was computed by Full-sky Lognormal Astro-fields Simulation Kit (FLASK) code from Lognormal random distributions of HI [18]. We will use the Unified Cosmological Library for C_l (UCLC_l) to compute the 21-cm angular power spectrum to the correspondent 30 frequencies of the radiotelescope, constraining cosmological parameters by implementing a nested sampling algorithm in Markov Chain Monte Carlo (MCMC) processes.

Outline: The dissertation is organized as follows: in Chap. 1 we introduce the standard cosmological model, passing through its main characteristics, and we end up discussing some problems of this model; in Chap. 2 we present Horndeski gravity, establishing a phenomenological α-basis for coefficients arise from second-order linear perturbations of Horndeski action, and we close this chapter providing two parameterizations for α_i functions; in Chap. 3 we describe some observables used in this work to constrain the MG parameters − CMB and the 21-cm signal −, including the angular power spectrum formalism; in Chap. 4 we present the necessary resources from Bayesian statistics for cosmological parameter inferences; in Chap. 5 we show results for parameter constraints, recovered from MCMC processes; and in Chap. 6 we present the conclusion and perspectives.

Remarks & Conventions:

In this work we follow the most used books of Cosmology:

◇ S. Weinberg, *Gravitation and Cosmology*. Wiley (1973);

◇ S. Dodelson, *Modern Cosmology*. Academic Press (2003);

We adopt the S. Dodelson's (D) definition conventions in most parts of this dissertation; in Chap. 1 we especially follow S. Weinberg's (W) conventions in some step calculations. It is worth mentioning their differences, namely:

◇ Riemann tensor definition

$$\begin{aligned} (D) \qquad R_{\mu\nu} &= \Gamma^{\alpha}_{\mu\nu,\alpha} - \Gamma^{\alpha}_{\mu\alpha,\nu} + \Gamma^{\alpha}_{\mu\nu}\Gamma^{\beta}_{\alpha\beta} - \Gamma^{\alpha}_{\mu\beta}\Gamma^{\beta}_{\alpha\nu} \\ (W) \qquad R_{\mu\nu} &= \Gamma^{\alpha}_{\mu\alpha,\nu} - \Gamma^{\alpha}_{\mu\nu,\alpha} + \Gamma^{\alpha}_{\mu\beta}\Gamma^{\beta}_{\alpha\nu} - \Gamma^{\alpha}_{\mu\nu}\Gamma^{\beta}_{\alpha\beta} \end{aligned}$$

which yields $R^{(D)}_{\mu\nu} = -R^{(W)}_{\mu\nu}$ and $R^{(D)} = -R^{(W)}$.

◇ Perturbed variables definition (FLRW in Newtonian gauge)

$$\begin{aligned} (D) \qquad ds^2 &= -(1+2\Psi)dt^2 + a^2(1+2\Phi)dx^2 \\ (W) \qquad ds^2 &= -(1+2\Phi)dt^2 + a^2(1-2\Psi)dx^2 \end{aligned}$$

The conversion is $\Psi^{(D)} = \Phi^{(W)}$ and $\Phi^{(D)} = -\Psi^{(W)}$.

Our metric signature is $(-,+,+,+)$, and we consider the usual convention of Latin letters i, j, k running over the three spatial coordinates, assuming values 1,2,3, while Greek indices $\alpha, \mu, \nu, \ldots$ run from 0 to 3.

1 The Standard Cosmological Model

We start considering relativistic cosmology with a derivation of the classical gravitational field equations, the dynamic equations of GR. As a motivation, let us make an observation about the Newton theory of gravity, follow the Einstein path, and see how gravity can be understood from physical-geometric considerations.

In the Newtonian theory, the gravitational force $\vec{F}$ on a (test) particle of gravitational and inertial masses m_G, m_I, respectively, at some position with gravitational potential Φ, leads to the dynamic equation

$$\vec{F} = m_G \vec{g} = -m_G \vec{\nabla}\Phi \qquad \Rightarrow \qquad \frac{d^2\vec{x}}{dt^2} = -\frac{m_G}{m_I}\vec{\nabla}\Phi. \tag{1.1}$$

It is a well-established experimental fact that the ratio m_G/m_I appearing in the equation of motion is *the same and equal to unity for all particles*. There is no reason in the Newtonian theory for this remarkable coincidence: the quantity that determines the magnitude of the gravitational force on the particle should be equal to the quantity that determines the particle "resistance" to an applied force in general.

The equality of the gravitational and inertial masses of a particle led Einstein to his classic "elevator" thought experiment, resulting in the postulate that follows.

Strong Equivalence Principle[1]:

In a freely falling (non-rotating) laboratory occupying a small region of spacetime, the laws of physics are those of Special Relativity.

From this postulate, Einstein made a profound proposal that provides a relativistic description of gravity and incorporates naturally the equivalence postulate (and consequently the equivalence of gravitational and inertial mass).

Einstein proposed that *gravity should no longer be regarded as a force in the conventional sense but rather as a manifestation of the curvature of the spacetime, this curvature being induced by the presence of matter*. This is the central idea of GR theory.

[1] The *weak equivalence principle* refers only to the trajectories of freely falling particles, and not to all the Laws of physics.

1.1 Einstein Field Equations

Following the variational principle approach, we must define a Lagrangian density $\mathcal{L}$ which is a scalar under global coordinate transformations. From the knowledge of gravitation as a manifestation of spacetime curvature, we might expect $\mathcal{L}$ to be derived from the components $g_{\mu\nu}$ of the metric tensor (the dynamical fields here), its first and second-order derivatives, and the curvature tensor.

The simplest non-trivial candidate for this purpose is the *scalar curvature* R (the only scalar derivable from the metric tensor that depends on derivatives no higher than second order), which allows us to write the Lagrangian density $\mathcal{L} = \sqrt{-g}R$. So, the gravitational action, also known as *Einstein-Hilbert action*, therefore is

$$S_{EH} = \int d^4x\sqrt{-g}R. \tag{1.2}$$

Explicitly, R is written as

$$R = g^{\mu\nu}R_{\mu\nu}, \tag{1.3}$$

where the *Riemann-Christoffel curvature tensor*, $R_{\mu\nu}$, is defined by

$$R_{\mu\nu} = \Gamma^{\alpha}_{\mu\nu,\alpha} - \Gamma^{\alpha}_{\mu\alpha,\nu} + \Gamma^{\alpha}_{\mu\nu}\Gamma^{\beta}_{\alpha\beta} - \Gamma^{\alpha}_{\mu\beta}\Gamma^{\beta}_{\alpha\nu}, \tag{1.4}$$

with the *Christoffel symbols*

$$\Gamma^{\alpha}_{\mu\nu} = \frac{1}{2}g^{\alpha\rho}(g_{\rho\mu,\nu} + g_{\rho\nu,\mu} - g_{\mu\nu,\rho}). \tag{1.5}$$

Looking at $g^{\mu\nu}$ as an independent dynamical variable, the variation of Eq. (1.2) with respect to this quantity gives the Einstein equations in vacuum (see Apend. A.1 for a detailed derivation)

$$R_{\mu\nu} - \frac{1}{2}Rg_{\mu\nu} = 0. \tag{1.6}$$

To obtain the full field equations, we must to add to the gravitational action a matter term, S_M,

$$S = \frac{1}{2\kappa}S_{EH} + S_M. \tag{1.7}$$

where $\kappa = 8\pi G/c^4$ is a normalization constant. Defining the *energy-momentum tensor* as

$$T_{\mu\nu} = -2\frac{1}{\sqrt{-g}}\frac{\delta S_M}{\delta g^{\mu\nu}}, \tag{1.8}$$

and, by following the principle of stationary action,

$$\frac{1}{\sqrt{-g}}\frac{\delta S}{\delta g^{\mu\nu}} = \frac{1}{2\kappa}\left(R_{\mu\nu} - \frac{1}{2}Rg_{\mu\nu}\right) + \frac{1}{\sqrt{-g}}\frac{\delta S_M}{\delta g^{\mu\nu}} = 0, \tag{1.9}$$

we get the full field equations

$$G_{\mu\nu} \equiv R_{\mu\nu} - \frac{1}{2} R g_{\mu\nu} = \frac{8\pi G}{c^4} T_{\mu\nu}. \tag{1.10}$$

where $G_{\mu\nu}$ is the *Einstein tensor*.

1.1.1 Cosmological Constant Term

In deriving the Eq.s (1.6) and (1.10), we assumed that the tensor $R_{\mu\nu}$ should contain only terms that are linear in the second-order derivatives of metric tensor. Thus, we can add any constant multiple of $g_{\mu\nu}$ to the left-hand side of these equations and still obtain a consistent set of field equations. Denoting this multiple by Λ, the field equations become

$$R_{\mu\nu} - \frac{1}{2} R g_{\mu\nu} + \Lambda g_{\mu\nu} = \frac{8\pi G}{c^4} T_{\mu\nu} \, . \tag{1.11}$$

Λ is known as the *cosmological constant*, which was proposed by Einstein in order to obtain a static universe. Nowadays, the cosmological constant plays an important role in Cosmology, and has been proposed as an exotic fluid responsible for the late-time accelerated expansion of the universe[2].

1.1.2 The Source Term

Now, we must express explicitly the source term (Eq. 1.8) which describes the matter distribution at each event in spacetime. Let us consider some general time-dependent distribution of non-interacting particles, each of rest mass m.

At each event in spacetime, we can characterize the distribution completely by giving the matter density, ρ, and the 3-velocity, $\vec{u}$, as a measured in some inertial frame. For simplicity, let us consider the fluid in its instantaneous rest frame S, in which $\vec{u} = \vec{0}$, with the proper density $\rho = mn$, where n is the number of particles in a unit volume.

At some other frame S', moving with speed v relative to S, the volume containing a fixed number of particles is Lorentz contracted along the direction of motion. Hence, in S' the number density of particle is $n' = \gamma n$ and the mass of each particle $m' = \gamma m$, with γ the Lorentz factor $\gamma = (1 - v^2/c^2)^{-1/2}$. Thus, the matter density in S' is

$$\rho' = \gamma^2 \rho, \tag{1.12}$$

[2] Notice that in writing the Einstein field equations (Eq. 1.11) we adopted the S. Dodelson's convention in defining the Riemann tensor, which differs from that of S. Weinberg by a minus sign. The Weinberg case can be recovered by doing the replacements: $R_{\mu\nu} \to -R_{\mu\nu}$ and $R \to -R$. See the remarks at the end of Introduction.

from which we can conclude that it does not transform as a scalar but as the 00-component of a rank-2 tensor. We may identify that tensor as $T_{\mu\nu}$, given in some arbitrary coordinate system x_μ, by

$$T_{\mu\nu} = \rho u_\mu u_\nu, \tag{1.13}$$

with $u_\mu = \gamma(c, \vec{u})$.

Considering *real fluids*, we must take into account the facts that (i) each particle has some random (thermal) velocity and (ii) there may be various forces between the particles that contribute to the total potential energies. Thus, the physical meaning of the components of $T_{\mu\nu}$ is

- $\diamond$ T_{00}: the total energy density, including any potential energy contributions from forces between the particles and kinetic energy from their random thermal motions;
- $\diamond$ T_{0i}: although there is no bulk motion, energy might be transmitted by heat conduction, so this is basically a heat conduction term in the rest frame;
- $\diamond$ T_{i0}: again, although the particles have no bulk motion, if heat is being conducted then the energy will carry momentum;
- $\diamond$ T_{ij}: the random thermal motions of the particles will give rise to momentum flow, so that T_{ii} is the *isotropic pressure* in the i-direction and the T_{ij} (with $i \neq j$) are the *viscous stresses* in the fluid.

These identifications are valid for a general fluid. However, in order to obtain solutions of Einstein field equations, for simplicity, we will idealize the universe and model the matter by a *perfect fluid*.

A perfect fluid is defined as one for which there are no forces between the particles, and no heat conduction or viscosity in the rest frame. Thus, in the rest frame, $T_{\mu\nu}$ reads

$$T_{\mu\nu} = \begin{pmatrix} \rho c^2 & 0 & 0 & 0 \\ 0 & p & 0 & 0 \\ 0 & 0 & p & 0 \\ 0 & 0 & 0 & p \end{pmatrix}. \tag{1.14}$$

For any frame, this tensor is generalized as

$$T_{\mu\nu} = (\rho + p/c^2) u_\mu u_\nu + p g_{\mu\nu}. \tag{1.15}$$

From this last equation, we see that $T_{\mu\nu}$ is symmetric, and made up of two scalar fields ρ, p and the vector field $\vec{u}$ that characterize the perfect fluid. Also, in the limit $p \to 0$ a perfect fluid becomes dust.

1.1.3 Weak-Field Limit

Let us check the consistency of the Einstein field equations with the Newtonian result. For this purpose, we must consider all velocities $u^i = dx^i/dt$ are small relative to the velocity of light, *i.e.* $|\vec{u}| \ll c$, and that the metric tensor is time-independent, $g_{\mu\nu}(\vec{x}) = g_{\mu\nu}(\vec{x}, t)$. Since we are interested in small effects of gravity, we will consider $h_{\mu\nu}$ as the correction to the Minkowski metric tensor, with $|h_{\mu\nu}| \ll 1$,

$$g_{\mu\nu} = \eta_{\mu\nu} + h_{\mu\nu}. \tag{1.16}$$

The Eq. (1.11) can be rewritten as

$$R_{\mu\nu} = \kappa \left(T_{\mu\nu} - \frac{1}{2} T g_{\mu\nu} \right) - \Lambda g_{\mu\nu}, \tag{1.17}$$

where T is the trace $T^\mu_\mu = g^{\mu\nu} T_{\nu\mu}$. The 00-component of the last equation, in the weak-field limit ($g_{00} \approx -1$) reads

$$\begin{aligned} R_{00} &= \partial_0 \Gamma^\mu_{0\mu} - \partial_\mu \Gamma^\mu_{00} + \Gamma^\nu_{0\mu} \Gamma^\mu_{\nu 0} - \Gamma^\nu_{00} \Gamma^\mu_{\nu\mu} \\ &\approx -\partial_i \Gamma^i_{00} = \frac{1}{2} \delta^{ij} \partial_i \partial_j h_{00}, \end{aligned} \tag{1.18}$$

where, in the first line, the product of the Christoffel symbols drop out, and the time derivatives are null, since we are considering the metric tensor time-independent. The 00-component of the matter source is $T_{00} = \rho c^2$. Then,

$$\frac{1}{2} \delta^{ij} \partial_i \partial_j h_{00} = \kappa \left(\rho c^2 - \frac{1}{2} \rho c^2 \right) + \Lambda \qquad \Rightarrow \qquad \frac{1}{2} \nabla^2 h_{00} = \frac{\kappa}{2} \rho c^2 + \Lambda. \tag{1.19}$$

Comparing the geodesic equation of a particle moving in the curved spacetime[3],

$$\frac{d^2 x^\mu}{d\tau^2} + \Gamma^\mu_{\nu\sigma} \frac{d^2 x^\nu}{d\tau^2} \frac{d^2 x^\sigma}{d\tau^2} = 0, \tag{1.20}$$

with the Newton law of gravity, we get in weak-field limit[4] $h_{00} = -2\Phi/c^2$. Thus, we obtain the *Poisson equation*

$$\nabla^2 \Phi = 4\pi G \rho + \Lambda c^2, \tag{1.21}$$

and, considering the Newtonian potential $\Phi = -M/r$, the gravitational field strength reads

$$\vec{g} = -\vec{\nabla} \Phi = -\frac{GM}{r^2} \hat{r} + \frac{\Lambda c^2}{3} r \hat{r}. \tag{1.22}$$

[3] Here, τ is the proper time.

[4] Notice that now we followed the S. Weinberg's convention in writing the perturbed variable Φ. Such a choice differs from that of S. Dodelson who instead writes Ψ. See the remarks at the end of Introduction.

Looking at this equation, we see that the cosmological constant term corresponds to a gravitational repulsion whose strength increases linearly with r. Also, in the absence of matter, this term is related to the vacuum energy: $\Lambda > 0$ defines a spacetime known as *de Sitter*, with curvature constant equal or greater than zero; whilst $\Lambda < 0$ provides a spacetime called *anti-de Sitter*, with negative curvature constant (see the discussion about the cosmological constant problem at the end of this chapter). From now on we will employ natural units in the calculations, restoring physical quantities whenever it becomes necessary.

1.2 Friedmann Equations

1.2.1 Cosmological Principle

When we look up at the sky, we see that the stars around us are grouped into a large-density concentration − the Milk Way. On a slightly *large scale* ($\gtrsim 100$ Mpc[5]), we see that our Galaxy belongs to a small group of galaxies − the Local Group. Evidently, on *small scales* ($\lesssim 10$ Mpc), matter is distributed in a highly irregular way, but as we look on larger and larger scales, the matter distribution looks more and more uniform.

In fact, we have very good evidence − particularly from the constancy of CMB temperature − that the universe is *isotropic* on the largest scales. This indicates that the space-time describing the observable universe should have a spherical symmetry around us. If the universe has no preferred center, then isotropy also implies *homogeneity*. To study simple cosmological models it is reasonable then to assume the *Cosmological Principle*, which supposes that the universe is spatially isotropic and homogeneous. The Cosmological Principle makes predictions about all unobservable regions beyond the observable universe, which makes it a very strong hypothesis.

1.2.2 FLRW Metric

The geometric structure and evolution of the universe can be studied from a distance element on the Minkowski space written as

$$ds^2 = g_{\mu\nu} dx^\mu dx^\nu = -dt^2 + a^2 \left[\frac{dr^2}{1 - kr^2} + r^2 \left(d\theta^2 + \sin^2 \theta d\phi^2 \right) \right], \tag{1.23}$$

where $a = a(t)$ is the scale factor that holds the spacetime expansion. This equations is known as Friedmann-Lemaitre-Robertson-Walker (FLRW) metric with the values of curvature constant $k < 0$, $k = 0$ and $k > 0$, representing the geometry of an spacetime *open*, *flat*, and *closed*, respectively.

[5] A parsec (pc) is 3.26 light-years.

It will be useful to write this metric in matrix form, which reads

$$g_{\mu\nu} = \begin{pmatrix} -1 & 0 & 0 & 0 \\ 0 & \frac{a^2}{1-kr^2} & 0 & 0 \\ 0 & 0 & a^2r^2 & 0 \\ 0 & 0 & 0 & a^2r^2\sin^2\theta \end{pmatrix}. \tag{1.24}$$

The Eq. (1.5), for this metric, results in zero if $\alpha \neq \mu \neq \nu$. Defining the *Hubble parameter* as $H(t) \equiv \dot{a}/a$ − where dot means the derivative in cosmic time −, the non-vanishing connections are

i) $\alpha = 0$

$$\Gamma^0_{\mu\nu} = \frac{1}{2}g^{00}(g_{0\mu,\nu} + g_{0\nu,\mu} - g_{\mu\nu,0})$$

$$\begin{aligned} \Gamma^0_{00} &= 0 & \qquad \Gamma^0_{22} &= a\dot{a}r^2 = Hg_{22} \\ \Gamma^0_{11} &= \frac{a\dot{a}}{1-kr^2} = Hg_{11} & \qquad \Gamma^0_{33} &= a\dot{a}r^2\sin^2\theta = Hg_{33} \end{aligned}$$

$$\Gamma^0_{ij} = Hg_{ij} \tag{1.25}$$

ii) $\alpha = 1$

$$\Gamma^1_{\mu\nu} = \frac{1}{2}g^{11}(g_{1\mu,\nu} + g_{1\nu,\mu} - g_{\mu\nu,1})$$

$$\begin{aligned} \Gamma^1_{00} &= 0 & \qquad \Gamma^1_{33} &= r\sin^2\theta(kr^2-1) \\ \Gamma^1_{11} &= \frac{kr}{1-kr^2} & \qquad \Gamma^1_{01} &= \Gamma^1_{10} = H \\ \Gamma^1_{22} &= r(kr^2-1) \end{aligned}$$

iii) $\alpha = 2$

$$\Gamma^2_{\mu\nu} = \frac{1}{2}g^{22}(g_{2\mu,\nu} + g_{2\nu,\mu} - g_{\mu\nu,2})$$

$$\begin{aligned} \Gamma^2_{00} &= \Gamma^2_{11} = \Gamma^2_{22} = 0 & \qquad \Gamma^2_{20} &= \Gamma^2_{02} = H \\ \Gamma^2_{33} &= -\sin\theta\cos\theta & \qquad \Gamma^2_{12} &= \Gamma^2_{21} = \frac{1}{r} \end{aligned}$$

iv) $\alpha = 3$

$$\Gamma^3_{\mu\nu} = \frac{1}{2} g^{33} (g_{3\mu,\nu} + g_{3\nu,\mu} - g_{\mu\nu,3})$$

$$\begin{aligned} \Gamma^3_{00} &= \Gamma^3_{11} = \Gamma^3_{22} = \Gamma^3_{33} = 0 \\ \Gamma^3_{30} &= \Gamma^3_{03} = H \end{aligned} \qquad \begin{aligned} \Gamma^3_{32} &= \Gamma^3_{23} = \cot\theta \\ \Gamma^3_{31} &= \Gamma^3_{13} = \frac{1}{r} \end{aligned}$$

Writing some terms in a compact way, we get

$$\Gamma^\alpha_{00} = 0, \qquad \Gamma^i_{0j} = \delta^i_j H \tag{1.26}$$

The time-time component of the Ricci tensor (Eq. 1.4) is

$$\begin{aligned} R_{00} &= \Gamma^\alpha_{00,\alpha} - \Gamma^\alpha_{0\alpha,0} + \Gamma^\alpha_{00}\Gamma^\beta_{\alpha\beta} - \Gamma^\alpha_{0\beta}\Gamma^\beta_{\alpha 0} \\ &= -3\partial_t H - 3H^2 \\ &= -3\frac{\ddot{a}}{a}. \end{aligned} \tag{1.27}$$

On the other hand, using the results for non-zero connections, the spatial components of the same tensor are of the form

$$R_{ij} = g_{ij}\left(2H^2 + \frac{\ddot{a}}{a} + \frac{2k}{a^2}\right). \tag{1.28}$$

Thus, the Ricci scalar (Eq. 1.3) is

$$R = g^{\mu\nu} R_{\mu\nu} = g^{00} R_{00} + g^{ij} R_{ij} = 6\left(\frac{\ddot{a}}{a} + H^2 + \frac{k}{a^2}\right). \tag{1.29}$$

Combine Eq.s (1.14) and (1.29), the time components of Einstein equations give the *first Friedmann equation*

$$\left(\frac{\dot{a}}{a}\right)^2 = \frac{1}{3}\frac{\rho}{M_{Pl}^2} + \frac{\Lambda}{3} - \frac{k}{a^2}. \tag{1.30}$$

where $M_{Pl} \equiv 1/\sqrt{8\pi G} = 2.4 \times 10^{18}$ GeV is the *Planck mass*. On the other hand, considering the same set of equations, the spatial components of Einstein equations give the *second Friedmann equation*

$$\frac{\ddot{a}}{a} = -\frac{1}{6M_{Pl}^2}(\rho + 3p) + \frac{\Lambda}{3}. \tag{1.31}$$

As we shall see later, the cosmological constant can be absorbed in the right-hand side of Eq. (1.30) as an exotic fluid, providing the simplest explanation of the present-time accelerated expansion of the universe (see Eq. 1.59).

1.2.3 Energy Conservation Equation

The conservation of the energy-momentum tensor implies the vanishing of the covariant derivative

$$\nabla_\mu T^\mu_\nu \equiv \frac{\partial T^\mu_\nu}{\partial x^\mu} + \Gamma^\mu_{\alpha\mu} T^\alpha_\nu - \Gamma^\alpha_{\nu\mu} T^\mu_\alpha = 0. \tag{1.32}$$

The vanishing of $\nabla_\mu T^\mu_\nu$ is four separate equations; let us consider the $\nu = 0$ component

$$\frac{\partial T^\mu_0}{\partial x^\mu} + \Gamma^\mu_{\alpha\mu} T^\alpha_0 - \Gamma^\alpha_{0\mu} T^\mu_\alpha = 0. \tag{1.33}$$

Assuming the isotropy condition, T^i_0 vanishes. Then,

$$\frac{\partial \rho}{\partial t} + \Gamma^\mu_{0\mu}\rho - \Gamma^\alpha_{0\mu} T^\mu_\alpha = 0. \tag{1.34}$$

From Eq. (1.26), $\Gamma^\alpha_{0\mu}$ vanishes unless α, μ are spatial indices equal to each other. This gives

$$\dot{\rho} + 3H\left(\rho + p\right) = 0. \tag{1.35}$$

However, if the energy-momentum tensor is not conserved, the Eq. (1.32) no longer holds. Instead, considering the case where i fluids are couple conserved and can interact with each other, with $\sum_i Q^{(i)}_\nu = 0$, we then get

$$\nabla_\mu T^{\mu(i)}_\nu = Q^{(i)}_\nu. \tag{1.36}$$

1.3 Cosmological Redshift

In an expanding universe the galaxies are receding from us. Once the wavelength of light emitted from a receding object is stretched out so that the observed wavelength is larger than the emitted one. We can use the FLRW metric (1.23) to derive this stretching factor called *cosmological redshift*, denoted by z.

Suppose that a photon is emitted at position r_{em} and time t_{em} by a comoving observer, and that the photon is received at position $r_{ob} = 0$ and time t_{ob} by another observer at origin of coordinates system. Since this particle propagates along a geodesic, $ds = d\theta = d\phi = 0$, Eq. (1.23) gives

$$dt = \pm a(t)\frac{dr}{\sqrt{1-kr}} \qquad \Rightarrow \qquad \int_{t_{em}}^{t_{ob}} \frac{dt}{a(t)} = \int_0^{r_{em}} \frac{dr}{\sqrt{1-kr}}, \tag{1.37}$$

where the minus sign was chosen in the last equation, once the spatial coordinate r decreases and the cosmic time t grows.

Now, if the emitter sends a second light pulse at time $t_{em} + \delta t_{em}$, which is received at time $t_{ob} + \delta t_{ob}$, then

$$\int_{t_{em}+\delta t_{em}}^{t_{ob}+\delta t_{ob}} \frac{dt}{a(t)} = \int_0^{r_{em}} \frac{dr}{\sqrt{1-kr}}, \tag{1.38}$$

from which we see that

$$\int_{t_{em}}^{t_{em}+\delta t_{em}} \frac{dt}{a(t)} = \int_{t_{ob}}^{t_{ob}+\delta t_{ob}} \frac{dt}{a(t)}. \tag{1.39}$$

Assuming that δt_{em} and δt_{ob} are small, so that $a(t)$ can be taken as constant in both integrals, we have

$$\frac{\delta t_{em}}{a(t_{em})} = \frac{\delta t_{ob}}{a(t_{ob})}. \tag{1.40}$$

Considering the pulses to be the successive wave crests, we find

$$1 + z \equiv \frac{\nu_{em}}{\nu_{ob}} = \frac{\delta t_{ob}}{\delta t_{em}} = \frac{a(t_{ob})}{a(t_{em})}. \tag{1.41}$$

We conclude that a measurement of the amount by which emission light sources are stretched (or "redshifted", once their wavelengths increase, tending to red color in the electromagnetic spectrum) is a direct measure of how fast the structures in which they reside are receding from us. It is common to define $a(t_{ob}) \equiv 1$ for the present-day cosmic time, t_0.

1.3.1 Hubble Diagram

In 1912, V. Slipher, measuring radial velocities of galaxies, detected that the light from them was redshifted, providing the empirical basis for the expansion of the universe [19]. After G. Lemaitre presented in 1922 a theoretical possibility of an expanding universe [20], E. Hubble found that distant galaxies are in fact receding from us [21]. Applying the discoveries of H. Leavitt concerning bright Cepheids [22], Hubble noticed that the radial velocity of those galaxies, $v = cz$, increases proportional to their distances, d_L, with the slope given by the *Hubble constant*, H_0

$$v = H_0 d_L. \tag{1.42}$$

It is common in literature to present the Hubble constant as the *reduced Hubble constant*, $h \equiv H_0/100\ km^{-1}\ s\ Mpc$. Some predictions for the present-day cosmic expansion rate have a small difference between different observations: $H_0 = 67.36 \pm 0.54$ km/s/Mpc from Planck satellite [23] and $H_0 = 73.5 \pm 1.4 km/s/Mpc$ from SH0ES collaboration [24]. Known as "Hubble tension", this problem has been widely discussed, suggesting that there could be some

new physics from the Standard Model, or that there are systematic effects in one or more of the datasets [25].

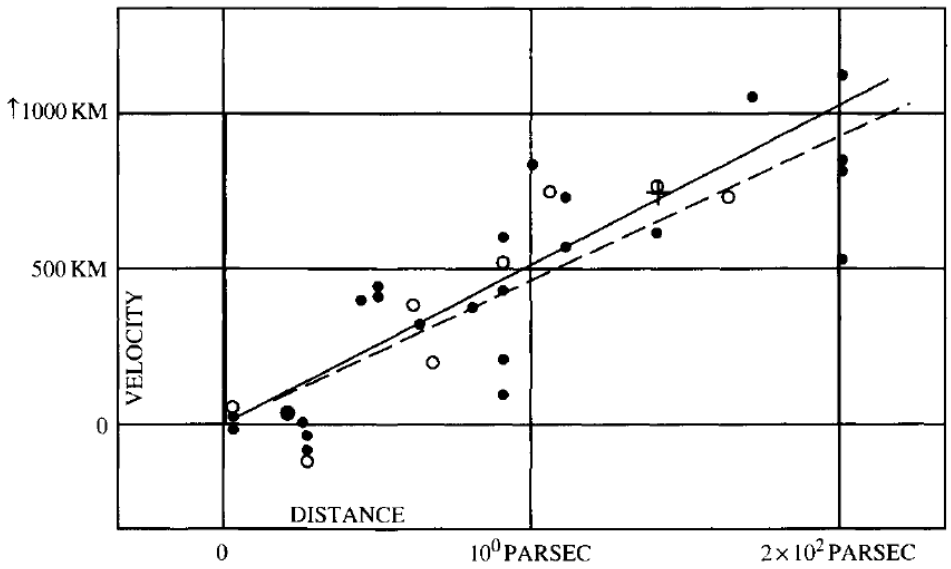

Figure 1 – The original Hubble diagram. Velocities of distant galaxies (units should be $km\ sec^{-1}$) are plotted vs distance (units should be Mpc). Extracted from [21].

1.4 Distances

1.4.1 Comoving Distance

The first distance we will define is the comoving distance. It will be useful to derive other operational distances, since this one is not observable in practice. From FRLW metric,

$$ds^2 = -dt^2 + a^2\left[d\chi^2 + S_k^2(\chi)d\Omega^2\right], \tag{1.43}$$

we have three possible spaces, varying accord to geometric value of curvature k

$$S_k^2(\chi) \equiv \begin{cases} \sinh(\chi) & k=-1 \\ \chi & k=0 \\ \sin(\chi) & k=1 \end{cases}. \tag{1.44}$$

In a flat universe, we define the *comoving distance* between us and a galaxy at redshift z as

$$\chi \equiv \int_0^z \frac{dz'}{H} = \int_{t_{em}}^{t_{ob}} \frac{dt}{a}, \tag{1.45}$$

where $H(z')$ depends on the universe content (see Eq. 1.62). The second equality is known as *conformal time*, which we will employ the symbol τ to denote it, and is equal to the comoving distance along the light path, $\chi = \tau$.

1.4.2 Luminosity Distance

Considering a source with absolute *luminosity*, L, (measured in Js^{-1}), such as SNIa. If we were in a static Euclidean space, we may define the *flux*, F, (measured in Wm^{-2}) as

$$F \equiv \frac{L}{4\pi\chi^2}. \tag{1.46}$$

However, the universe is actually expanding, meaning that the rate of photons we are receiving is reduced by a factor of $1/(1+z)$, and each photon also is redshifted by the same factor. Then, the fraction of light received will be

$$F = \frac{L}{4\pi\chi^2(1+z)^2} \equiv \frac{L}{4\pi d_L^2}, \tag{1.47}$$

where we have defined the *luminosity distance*, d_L, as:

$$d_L = (1+z)\chi = (1+z)\int_0^z \frac{dz'}{H}. \tag{1.48}$$

1.4.3 Angular Diameter Distance

Another important distance measure is based on the existence of "standard ruler" (see Sec. 3.2), *i.e.* objects of known physical size l, whose *angular diameter distance*, d_A, we can evaluate by measuring its angular size θ, using the Euclidean formula

$$d_A = \frac{l}{\theta}. \tag{1.49}$$

As the universe is expanding, the relation between the transverse size of the object, l, and its angular size on the sky, θ, when its light was emitted, is $l = d_A\theta = a(t_{em})\chi(z)\theta = \chi(z)\theta/(1+z)$. So, in a flat expanding universe, the angular diameter distance will be written as

$$d_A \equiv \frac{\chi(z)}{1+z} = \frac{1}{1+z}\int_0^z \frac{dz'}{H}. \tag{1.50}$$

The relation between the luminosity and angular diameter distances holds in any metric theory of gravity as long as photon number is conserved, and is given by

$$d_A = \frac{d_L}{(1+z)^2}. \tag{1.51}$$

1.5 Cosmological Components

Eq. (1.35) can be rewritten as

$$\frac{d(\rho a^3)}{dt} = -\frac{3p\dot{a}a^2}{c^2} \qquad \Rightarrow \qquad \frac{d(\rho a^3)}{da} = -\frac{3pa^2}{c^2}, \tag{1.52}$$

where the last equation was obtained by changing the variable $t \to a$. From thermodynamics, the energy density and pressure of a fluid are related by its equation of state,

$$p = \omega \rho c^2, \tag{1.53}$$

where ω is the *equation of state parameter*. Then, the Eq. (1.52) becomes

$$\frac{d(\rho a^3)}{da} = -3\omega \rho a^2. \tag{1.54}$$

Assuming the general case where ω_i of i fluids varies with the redshift (Eq. 1.41), the solution of the last equation can be written as

$$\rho_i(z) = \rho_{i,0} f(z), \tag{1.55}$$

where $\rho_{i,0}$ are the energy densities measured today, and $f(z)$ is given by

$$f(z) = exp\left[3\int_0^z \frac{1+\omega_i(z')}{1+z'} dz'\right]. \tag{1.56}$$

Considering a universe made up of matter (m), radiation (r), and an exotic fluid called DE, for each of these components the Eq. (1.54) gives the solutions that follow, with particular parameters of the equation of state

$$Matter \ \ (m) \ \ = \ \ \begin{cases} CDM \quad (c) \\ Baryons \quad (b) \end{cases} \qquad w = 0, \quad \rho_m(z) = \rho_{m,0}\,(1+z)^3 \tag{1.57}$$

$$Radiation \ \ (r) \ \ = \ \ \begin{cases} Photons \quad (\gamma) \\ Neutrinos \quad (\nu) \\ Gravitons \quad (g) \end{cases} \qquad w = \frac{1}{3}, \quad \rho_r(z) = \rho_{r,0}\,(1+z)^4 \tag{1.58}$$

$$Dark\ Energy \ \ (DE) \ \ = \ \ \begin{cases} Vacuum\ energy \\ Cosmo.\ constant \\ Modified\ gravity \end{cases} \qquad w = -1, \ \rho_\Lambda(z) = \rho_{\Lambda,0}\,(1+z)^0 \tag{1.59}$$

The case $\omega < -1/3$ is of interest because a fluid with this value provides a positive acceleration for the universe (see Eq. 1.31). The Eq. (1.59) is a special case of such fluid, when DE is just a cosmological constant ($\omega = -1$).

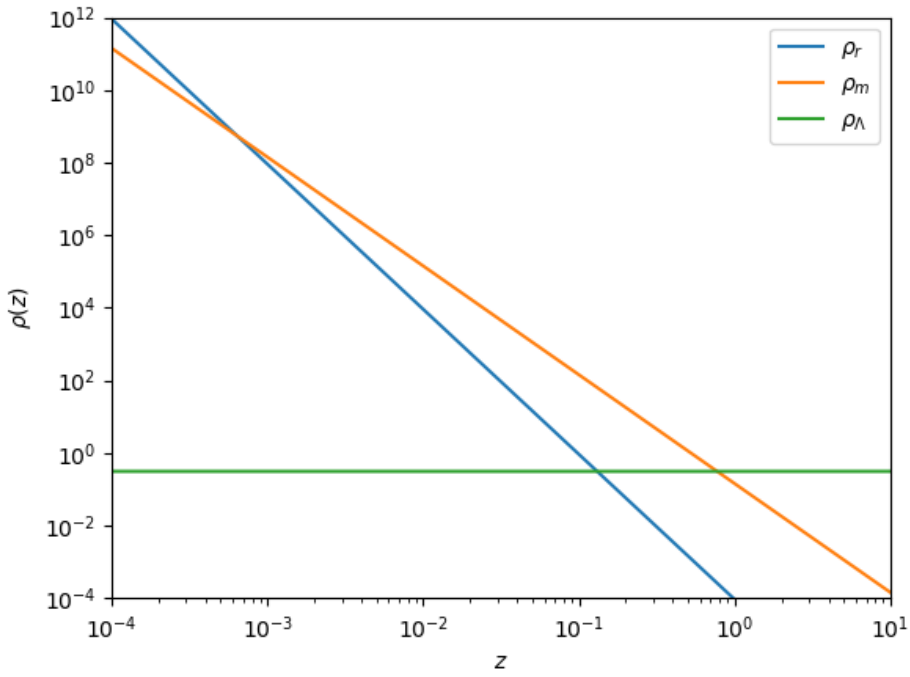

Figure 2 – Evolution of the matter specie densities.

1.6 Cosmological Parameters

The Friedmann equations (1.30) and (1.31) give the evolution of the universe once we specify the values of the cosmological density parameters $\rho_{i,0}$ at a specific cosmic time t. Specifying these quantities is sufficient to determine the scale factor a at all cosmic times.

However, it is convenient and a common practice in cosmology to work in terms of alternative dimensionless quantities, the *density parameters*. Dividing the first Friedmann Eq. (1.30) by H^2, we can write the coupled parameters equation

$$\Omega_i(t) + \Omega_k(t) = 1, \tag{1.60}$$

where we have defined

$$\Omega_i(t) \equiv \frac{1}{3}\frac{\rho_i(t)}{M_{Pl}^2 H^2(t)} \qquad \textit{and} \qquad \Omega_k(t) \equiv -\frac{k}{[a(t)H(t)]^2}, \tag{1.61}$$

with $i = m, r, DE$. Now, by specifying the four parameters H_0 and $\Omega_{i,0}$ we can get the evolution of the scale factor a (the link between ρ_i quantities and observations is discussed in Sec. 1.7.4). From Eq. (1.60), although the density parameters $\Omega_i(t)$ and $\Omega_k(t)$ are all function of the cosmic time, their sum cannot change sign. This means that the universe cannot evolve

from one form of FLRW geometry to another. With these definitions, the first Friedmann equation (1.30) gives the evolution of the Hubble parameter as a function of the redshift

$$H^2(z) = H_0^2 \left[\Omega_{m,0}\,(1+z)^3 + \Omega_{r,0}\,(1+z)^4 + \Omega_{DE,0} f(z) + \Omega_{k,0}\,(1+z)^2\right], \tag{1.62}$$

where the notation $\Omega_{i,0}$ means the density parameters are evaluated at the present-day.

1.7 Thermal Physics

In this section, we use thermodynamic principles to compute the relic abundance of particles that have been in thermal equilibrium at some stage of the universe's history. It will be useful to discriminate the contribution of radiation components to the cosmic inventory. Later, we will explore physics beyond equilibrium, presenting the Boltzmann equation and applying it to compute the relic abundance of a DM candidate.

1.7.1 Equilibrium

Consider a particle with g internal degrees of freedom in a box of volume $V = L^3$. The momentum eigenvalues have spacing h/L. So, the phase space density of states is given by

$$g \frac{1}{L^3} \frac{L^3}{h^3} = \frac{g}{h^3} = \frac{g}{(2\pi)^3}, \tag{1.63}$$

where the last equality makes use of the choice of units such that $\hbar = 1$.

A distribution function $f(\vec{x}, \vec{p}, t)$ tells us how the particles are distributed in the box. Assuming that f is

- ◇ Homogeneous (independent of $\vec{x}$),
- ◇ Isotropic (only dependent on $\vec{p}$ through $p = |\vec{p}|$),
- ◇ Time-dependent only through dependence on the temperature,

we can write $f = f(p)$, and densities of particle number, mass and pressure are given by

$$n = \frac{g}{(2\pi)^3} \int d^3p f(p), \tag{1.64}$$

$$\rho = \frac{g}{(2\pi)^3} \int d^3p E(p) f(p), \tag{1.65}$$

$$p = \frac{g}{(2\pi)^3} \int d^3p f(p) \frac{p^2}{3E(p)}, \tag{1.66}$$

where $E(p) = \sqrt{p^2 + m^2}$. The distribution function can be found by maximizing the entropy. In kinetic equilibrium it is given by

$$f(p) = \frac{1}{e^{(E-\mu)/T} \pm 1}, \tag{1.67}$$

where the + sign is for *fermions* and the − sign for *bosons*, and μ is the chemical potential (note we take $k_B = 1$), which corresponds to an asymmetry between particles and antiparticles.

If i species are in *chemical equilibrium*, then their chemical potential μ_i are related to the chemical potentials μ_j of the other species they interact with. For example, for a particles reaction of the form $1 + 2 \leftrightarrow 3 + 4$, the chemical equilibrium implies $\mu_1 + \mu_2 = \mu_3 + \mu_4$.

We will analyze the case where the particles are in *thermal equilibrium*, *i.e.* when the system is in both kinetic equilibrium and chemical equilibrium. This case applies when there is no asymmetry between particles-antiparticles. In particular, it applies to particles that are their own antiparticle (such as the photons or Majorana neutrinos).

Setting $\mu = 0$,

$$n = \frac{g}{(2\pi)^3} \int d^3p f(p) = \frac{g}{2\pi^2} \int_0^\infty dp p^2 f(p) = \frac{g}{2\pi^2} \int_0^\infty dp \frac{p^2}{e^{E/T} \pm 1}. \tag{1.68}$$

Defining $x = m/T$ and $y = p/T$, we get

$$n = \frac{g}{2\pi^2} T^3 \int_0^\infty dy \frac{y^2}{e^{\sqrt{x^2+y^2}} \pm 1} \equiv \frac{g}{2\pi^2} T^3 I_\pm(x), \tag{1.69}$$

where we have defined

$$I_\pm(x) \equiv \int_0^\infty dy \frac{y^2}{e^{\sqrt{x^2+y^2}} \pm 1}. \tag{1.70}$$

Similarly, for energy density we have (the calculus for pressure is analogous)

$$\rho = \frac{g}{(2\pi)^3} \int d^3p E(p) f(p) = \frac{g}{2\pi^2} T^4 \int_0^\infty dy \frac{y^2\sqrt{x^2+y^2}}{e^{\sqrt{x^2+y^2}} \pm 1} \equiv \frac{g}{2\pi^2} T^4 J_\pm(x), \tag{1.71}$$

with

$$J_\pm(x) \equiv \int_0^\infty dy \frac{y^2\sqrt{x^2+y^2}}{e^{\sqrt{x^2+y^2}} \pm 1}. \tag{1.72}$$

The integrals of Eq.s (1.70) and (1.72) cannot be performed exactly, but we can examine how they behave in certain limits (we solve them in A.2):

(i) Relativistic limit: $x \ll 1$

In the relativistic limit the temperature is bigger than the mass, and the results are

$$n = \frac{g\zeta(3)}{\pi^2}T^3 \times \begin{cases} 1 & \text{bosons} \\ \frac{3}{4} & \text{fermions} \end{cases}, \tag{1.73}$$

$$\rho = \frac{g\pi^2}{30}T^4 \times \begin{cases} 1 & \text{bosons} \\ \frac{7}{8} & \text{fermions} \end{cases}, \tag{1.74}$$

$$p = \frac{1}{3}\rho = \frac{g\pi^2}{90}T^4 \times \begin{cases} 1 & \text{bosons} \\ \frac{7}{8} & \text{fermions} \end{cases}, \tag{1.75}$$

where $\zeta(z)$ is the Riemann zeta-function.

(ii) Non-relativistic limit: $x \gg 1$

In the non-relativistic limit the temperature is much less than the mass, and since $E(p) \approx m$, for both bosons and fermions we have

$$n = g\left(\frac{mT}{2\pi}\right)^{3/2} e^{-m/T}, \tag{1.76}$$

$$\rho = mn = gm^{5/2}\left(\frac{T}{2\pi}\right)^{3/2} e^{-m/T}, \tag{1.77}$$

$$p = nT = g\left(\frac{m}{2\pi}\right)^{3/2} T^{5/2} e^{-m/T}. \tag{1.78}$$

We observe that, in the non-relativistic limit, the number, energy, and pressure densities of a particle species fall exponentially (are "Boltzmann suppressed") as the temperature drops below the mass of the particle. We can interpret this as the annihilation of particles and anti-particles.

At higher energies, these annihilations also occur, but they are balanced by particle-antiparticle pair production. At low temperatures, the thermal particle energies are not sufficient for pair production.

1.7.2 Effective Number of Relativistic Species

The radiation energy density is given as a sum of the energy density over all relativistic species

$$\rho_r = \sum_i \rho_i = \frac{\pi^2}{30} g_*(T) T^4, \tag{1.79}$$

where $g_*(T)$ is the effective number of *relativistic degrees of freedom* at temperature T. The sum over particle species may receive two types of contributions:

◇ Relativistic species that are not in thermal equilibrium with photons,

$$g_*(T) = \sum_{i=Boson} g_i \left(\frac{T_i}{T}\right)^4 + \frac{7}{8} \sum_{i=Fermion} g_i \left(\frac{T_i}{T}\right)^4 . \tag{1.80}$$

◇ Relativistic species that are in thermal equilibrium with photons ($T_i = T$),

$$g_*(T) = \sum_{i=Boson} g_i + \frac{7}{8} \sum_{i=Fermion} g_i. \tag{1.81}$$

In the relativistic regime, the matter content is dominated by radiation and the curvature is negligible. So, the first Friedmann equation is of the form

$$H^2 = \frac{1}{3M_{Pl}^2} \left(\frac{\pi^2}{30}\right) g_* T^4. \tag{1.82}$$

Numerically, this amounts to

$$H(T) = 0.33 g_*^{1/2} \frac{T^2}{M_{Pl}}, \tag{1.83}$$

or, equivalently,

$$\frac{T}{1\ MeV} \cong 1.5 g_*^{-1/4} \left(\frac{1\ sec}{t}\right)^{1/2}. \tag{1.84}$$

This equation tells us that the temperature of the universe 1 second after the Big Bang was about 1 MeV, and evolved as $t^{-1/2}$ before that.

1.7.3 Conservation of the Entropy

According to the second law of thermodynamics, the total entropy of the universe only increases or stays constant. Since there are more photons than baryons in the universe, the entropy of the universe is dominated by the entropy of the photon bath.

To a good approximation, we will treat the expansion of the universe as *adiabatic*, so that the entropy stays constant even beyond equilibrium. It can be shown that, in equilibrium and for $\mu = 0$,

$$\frac{\partial P}{\partial T} = \frac{\rho + P}{T}. \tag{1.85}$$

Now, considering the second law of thermodynamics, $TdS = dU + PdV$, and using $U = \rho V$, with $V = a^3(t)$ we get

$$\begin{aligned} dS &= \frac{1}{T}\left\{d\left[(\rho + P)V\right] - VdP\right\} = \frac{1}{T} d\left[(\rho + P)V\right] - \frac{V}{T^2}(\rho + P)\, dT \\ &= d\left(\frac{\rho + P}{T} V\right), \end{aligned} \tag{1.86}$$

from which

$$S = \frac{\rho + P}{T} V. \tag{1.87}$$

To show that entropy is conserved in equilibrium, we consider

$$\frac{dS}{dt} = \frac{d}{dt}\left(\frac{\rho + P}{T} V\right) = \frac{V}{T}\left[\frac{d\rho}{dt} + \frac{1}{V}\frac{dV}{dt}(\rho + P)\right] + \frac{V}{T}\left[\frac{dP}{dt} - \frac{\rho + P}{T}\frac{dT}{dt}\right] = 0, \tag{1.88}$$

where we have used the continuity equation (1.85) and (1.86). Defining the entropy density as $s \equiv S/V$, the total entropy for a collection of species is

$$s = \sum_i \frac{\rho_i + P_i}{T_i} = \frac{2\pi^2}{45} g_{*s}(T) T^3, \tag{1.89}$$

where g_{*s} is the effective number of *degrees of freedom in entropy*. Conservation in entropy implies that,

$$s \propto a^{-3} \qquad \textit{and} \qquad g_{*s}\,(Ta)^3 = const. \tag{1.90}$$

Following the thermal history of the universe, neutrinos (which were coupled to the thermal bath via weak interaction like $\nu_e + \bar{\nu}_e \leftrightarrow e^- + e^+$) decoupled and the temperature drops below the electron mass. This allows the electron-positron annihilation, and their energy and entropy are transferred only to photons $e^- + e^+ \leftrightarrow \gamma + \gamma$. At decoupling $T_\gamma = T_\nu$.

So, we can write

$$T_\gamma a|_{before} = T_\nu a|_{before} = T_\nu a|_{after}\,, \tag{1.91}$$

where the second equality follows from the fact that neutrinos, ν, are free streaming.

Before the process, we have $g_{*s}^{th} = 2 + \frac{7}{8}(2 \times 2) = 11/2$[6], and after $g_{*s}^{th} = 2$. So, by the conservation of entropy

$$g_{*s}^{th}(T_\gamma a)^3\Big|_{before} = g_{*s}^{th}(T_\gamma a)^3\Big|_{after}\,, \tag{1.92}$$

follows that

$$\frac{11}{2} T_\nu^3\Big|_{after} = 2T_\nu^3\Big|_{before} \qquad \Rightarrow \qquad \frac{T_\nu}{T_\gamma}\Big|_{after} = \left(\frac{4}{11}\right)^{1/3}. \tag{1.93}$$

This means that the temperature of neutrinos is slightly lower than the photon temperature after the positron-electron annihilation. Thus, for $T \ll m_e$, the effective number of relativistic species is

$$g_* = 2 + \frac{7}{8} N_{eff} \left(\frac{4}{11}\right)^{4/3} = 3.36, \tag{1.94}$$

where $N_{eff} = 3.046$ [23] is the *effective number of neutrino species* in the universe.

[6] Here, the superscript *th* denotes thermal equilibrium.

1.7.4 ΛCDM Model

ΛCDM is the simplest cosmological model: it requires only 6 independent parameters to describe the content and evolution of the universe. Fitted by the CMB power spectrum, such key parameters are baryon and cold dark matter densities, acoustic angular scale, optical depth, primordial power spectrum amplitude, and the spectral index, respectively denoted by Ω_b, Ω_{cdm}, θ, τ, A_s and n_s.

Other parameters may be derived from these last ones, providing some additional physical insights. The link between the first two model parameters and observations is givens as follows; the last four parameters will be discussed later (Chap. 3). First, let us consider the relativistic cosmic component, made up of the contributions of photons and neutrinos. The observational core of these quantities is based upon the mean CMB temperature measured today, given by $T_\gamma = 2.7255$ K [27]. Since photons has two spin states ($g_* = 2$ in Eq. 1.79), and using the Eq. (1.73) in the fermionic case for neutrinos (including anti-particles), their energy densities will be

$$\rho_\gamma = \frac{\pi^2}{15} T_\gamma^4 \qquad \textit{and} \qquad \rho_\nu = N_{eff} \frac{7\pi^2}{120} T_\nu^4. \tag{1.95}$$

From Eq. (1.61), the radiation parameter today is given by

$$\Omega_{r,0} = \Omega_{\gamma,0} + \Omega_{\nu,0} = 9.1 \times 10^{-5}. \tag{1.96}$$

Second, the matter density parameter splits into 26.7% of CDM, and only 4.9% of ordinary matter − baryons −,

$$\Omega_{b,0} = 0.0498, \qquad \Omega_{cdm,0} = 0.2673. \tag{1.97}$$

These values are also constrained by CMB observations. For baryons, the following property is explored: by increasing the baryon density, ρ_b, we get a smaller sound speed, c_s, of the photon-baryon plasma before recombination; as that plasma is described by the harmonic oscillator equation, its frequency kc_s decreases, generating a higher first CMB acoustic peak (see Eq. 3.43).

Observations also require the existence of another non-relativistic component in the universe − the CDM[7] −, since the baryonic matter alone is not sufficient to lead to structure formation, consistent with observations of galaxy clustering [28–33]. As the DM interacts very weakly with standard model particles, its existence can only be probed indirectly by gravitational effects on visible matter, having been measured also by the location of peaks

[7] Alternatively, DM can be 'hot' if it was relativistic at the photon decouple epoch, for which neutrino is a representative candidate. We focus on the cold one because the paradigm of structure formation is based on it.

in CMB anisotropies. The origin of CDM has not been identified yet; we discuss a possible particle candidate below.

From the closure Eq. (1.60), once the last observational results constraint $|\Omega_{k,0}| < 0.01$ [23] for the present universe, the sum of density components (Eq.s 1.96 and 1.97) does not exceed 0.3, and we are left with the remain ~ 0.7 cosmic component. So, in order to satisfy the closure equation, it is necessary to add an additional cosmic component called DE. If it were in fact a cosmological constant its present-day density parameter reads

$$\Omega_{\Lambda,0} = 0.6847. \tag{1.98}$$

1.7.5 Beyond Equilibrium

In order to describe the time evolution beyond the equilibrium of universe species, we must make use of the Boltzmann equation. Particularly, we will use it to describe the production of DM, and later to describe the freeze-out of electrons after Recombination (Sec. 3.1.1). The *Boltzmann equation*, in an expanding universe, is written as:

$$\frac{1}{a^3}\frac{d(n_i a^3)}{dt} = C_i[\{n_j\}], \tag{1.99}$$

where C_i is the collision term, which depends on the interactions under consideration. For a single process where the species 1 interacts with the specie 2 producing two new species, 3 and 4, via $1 + 2 \leftrightarrow 3 + 4$, we will have

$$\frac{1}{a^3}\frac{d(n_1 a^3)}{dt} = -\alpha n_1 n_2 + \beta n_3 n_4. \tag{1.100}$$

The first term of the right-hand side describes the annihilation of particles 1 and 2, while that second term accounts for the creation of particles 3 and 4. $\alpha = \langle\sigma v\rangle$ and β here are the *thermally averaged cross-section*; considering that, in chemical equilibrium, the collision term vanishes, we can write one of them in terms of other, such as:

$$\beta = \left(\frac{n_1 n_2}{n_3 n_4}\right)_{eq} \alpha, \tag{1.101}$$

and then,

$$\frac{1}{a^3}\frac{d(n_1 a^3)}{dt} = -\langle\sigma v\rangle \left[n_1 n_2 - \left(\frac{n_1 n_2}{n_3 n_4}\right)_{eq} n_3 n_4\right]. \tag{1.102}$$

In terms of the number of particles in a comoving volume, defined as $N_i = n_i/s$, we get

$$\frac{dN_1}{dlna} = -\frac{\Gamma_1}{H}\left[1 - \left(\frac{N_1 N_2}{N_3 N_4}\right)_{eq} \frac{N_3 N_4}{N_1 N_2}\right]. \tag{1.103}$$

In this equation, Γ_1/H is the *interaction efficiency*, with $\Gamma_1 = n_2\langle\sigma v\rangle$: for $\Gamma_1 \gg H$, the natural state of the system is in chemical equilibrium. If $N_1 \gg N_1^{eq}$, the r.h.s of that equation is negative; then particles 1 are destroyed and N_1 is reduced towards the equilibrium value N_1^{eq}. On the other hand, if $N_1 \ll N_1^{eq}$, the r.h.s of Eq. (1.103) is positive, and N_1 is driven toward N_1^{eq}. Finally, when the reaction rate drops below the Hubble scale, $\Gamma_1 < H$, the r.h.s of that equation gets suppressed, with the particles 1 approaching a constant relic density, $N_1 = const.$

1.7.6 WIMPs

As we discussed before, in order to form the presently observed galaxy structures a non-baryonic matter must be assumed in the universe: matter density fluctuations can start to grow much earlier, and have the amplitudes needed to form structures at the time of recombination. The first indications for the possible presence of DM in the universe are due to the astronomer J. Jeans, in 1922 [34], and later due to F. Zwicky, in 1933 [35]. A venerable history of DM can be found in this review [36].

The presence of DM in the universe was confirmed by many independent sources since the early 1980s: through dynamics of the galaxies and stars in the galaxies [37–39]; mass determinations based on gravitational lensing [42–45]; and X-ray studies of clusters of galaxies [40, 41]. An illustrative example comes from a well-studied spiral galaxy, NGC 3198, in 1985 [5]. The observed data are explained if some dark (invisible) matter exists, as shown in Fig. 3.

The curve labeled *disk* (lower panel) is the rotation curve that would be expected if the surface mass density in this galaxy were proportional to the light distribution (upper panel). The gas in the galaxy also contributes to the expected rotation curve, as shown by the curve labeled *gas*. The gas and the disk together cannot reproduce the observed flat rotation curve at a large radius; an extra gravitating component, the *dark halo*, is needed. The three labeled rotation curves, when added in quadrature, produce the total observed rotation curve.

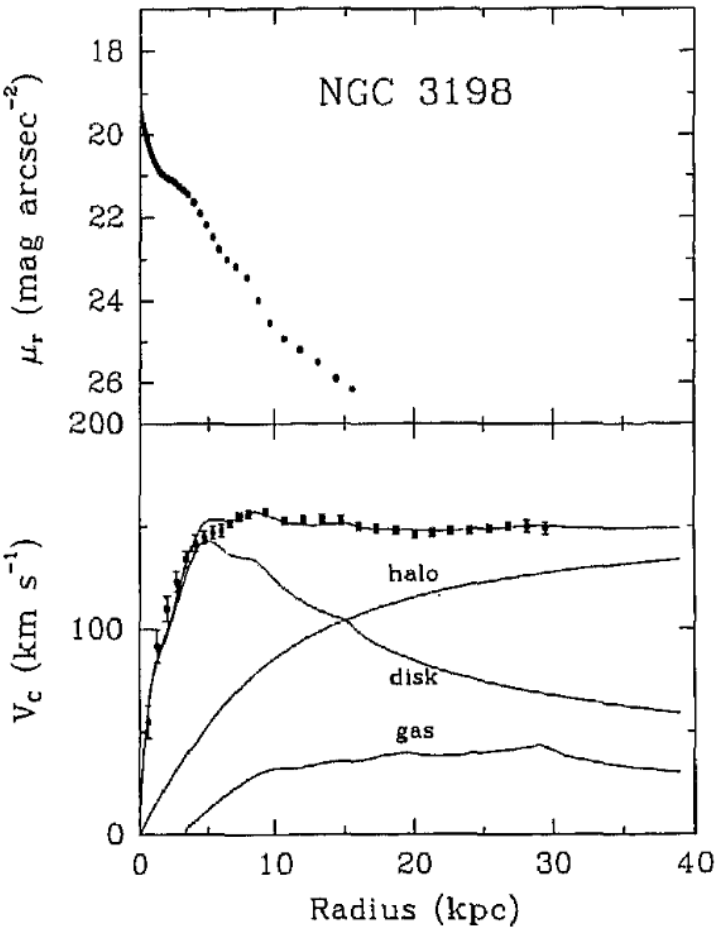

Figure 3 – (a) Upper panel: R-band radial surface brightness distribution of the spiral galaxy NGC 3198; (b) Lower panel: Neutral Hydrogen rotation curve (points) and the rotation curves of the individual mass components. Extracted from [5].

Particle DM candidates are proposed taking into account other open issues in particle physics, such as: WIMPs in connection with electroweak-scale new physics that address the hierarchy problem; *axions* in connection with frameworks that address the strong charge parity (CP) problem; sterile neutrinos in connection with the problem of neutrino masses and mixing [46]. A DM particle can be considered a good candidate only if pass the "ten tests" that follows [47]

1. Does it match the appropriate relic density?
2. Is it cold?
3. Is it neutral?
4. Is it consistent with Big Bang Nucleosynthesis (BBN)?
5. Does it leave stellar evolution unchanged?

6. Is it compatible with constraints on self-interactions?
7. Is it consistent with direct DM searches?
8. Is it compatible with gamma-ray constraints?
9. Is it compatible with other astrophysical bounds?
10. Can it be probed experimentally?

We will focus on WIMPs because they providing a simple mechanism to explain the expected DM relic abundance via the "WIMP miracle". To compute the relics of WIMPs we must assume some things about the DM particle, X: first, this particle and its antiparticle, $\bar{X}$ can annihilate to produce two massless particles, l and $\bar{l}$, through the process

$$X + \bar{X} \leftrightarrow l + \bar{l}. \tag{1.104}$$

Also, we assume that massless particles are tightly coupled to the cosmic plasma in order to maintain their equilibrium densities, $n_l = n_l^{eq}$, and we must assume that there is no initial asymmetry between X and $\bar{X}$, *i.e.* $n_X = n_{\bar{X}}$. With these assumptions, in a comoving volume, $N_X = n_X/s$, the Boltzmann equation (1.102) for WIMPs is written as

$$\frac{dN_X}{dt} = -s\langle\sigma v\rangle \left[N_X^2 - (N_X^{eq})^2\right]. \tag{1.105}$$

As the interesting dynamics will take place when the temperature is of order the particle mass, $T \sim M_X$, we make the change of variables

$$x \equiv \frac{M_X}{T}. \tag{1.106}$$

Considering the epoch of radiation domination, with $T \propto a^{-1}$ (*i.e.* $g_{\star s} \approx const.$), the Eq. (1.105) becomes the so called *Riccati equation*,

$$\frac{dN_X}{dx} = -\frac{\lambda}{x^2}\left[N_X^2 - (N_X^{eq})^2\right], \tag{1.107}$$

where we have defined

$$\lambda \equiv \frac{2\pi^2}{45} g_{\star s} \frac{M_X^3 \langle\sigma v\rangle}{H(M_X)}. \tag{1.108}$$

Here, we will consider λ as a constant. Even for this case, there is no analytic solution for Eq. (1.107). Let us determine the freeze-out density of dark matter as a function of λ. After freeze-out, N_X will be larger than N_X^{eq}. So that, we can drop N_X^{eq} in Eq. (1.107), obtaining which follows

$$\frac{dN_X}{dx} \backsimeq -\frac{\lambda N_X^2}{x^2} \qquad (x > x_f). \tag{1.109}$$

Integrating from x_f to $x = \infty$, we find:

$$\frac{1}{N_X^{\infty}} - \frac{1}{N_X^f} = \frac{\lambda}{x_f}, \tag{1.110}$$

where $N_X^f \equiv N_X(x_f)$. As $N_X^f \gg N_X^{\infty}$ (See Fig.4), an analytic approximation for Eq. (1.110) will be:

$$N_X^{\infty} \backsimeq \frac{x_f}{\lambda}. \tag{1.111}$$

This solution depends on the unknown freeze-out temperature, x_f, for which an estimate is $x_f \sim 10$ (see Fig. 4). We see that, as the interaction rate λ increases, the relic abundance N_X^{∞} decreases.

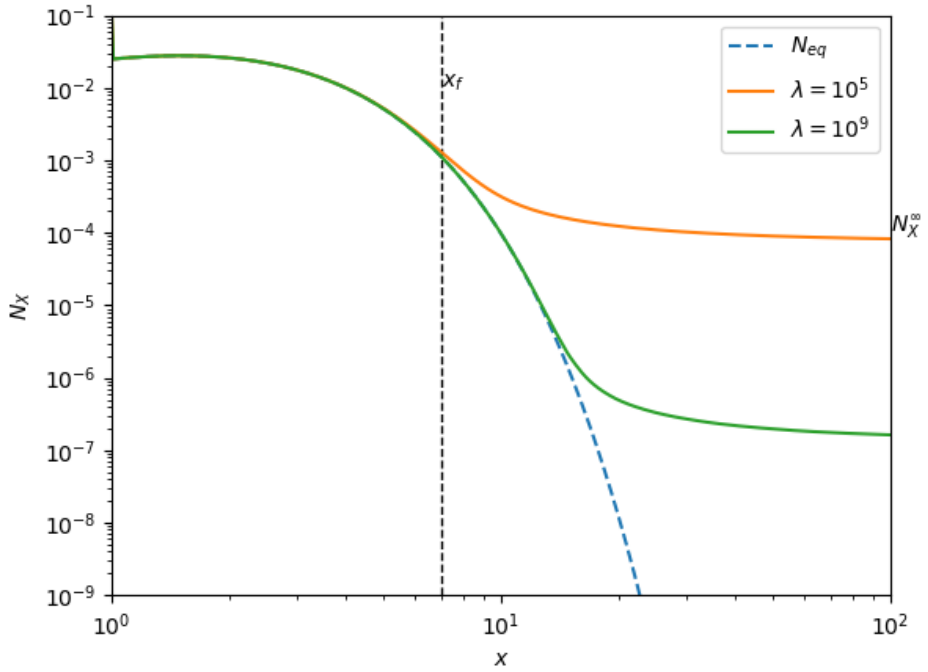

Figure 4 – Abundance of DM particles as the temperature drops below the mass.

Then, let us estimate the relic abundance of DM today. Using that the number of WIMPs is conserved after freeze out, *i.e.* $N_{X,0} = N_X^{\infty}$, we have

$$\Omega_{X,0} = \frac{8\pi G}{3H_0^2}\rho_{X,0} = \frac{8\pi G}{3H_0^2} M_X N_{X,0} s_0 = \frac{8\pi G}{3H_0^2} M_X N_X^{\infty} s_0. \tag{1.112}$$

Now, using Eq.s (1.89), (1.108), (1.111) and that $H = (8\pi G\rho_r/3)^{1/2} = (8\pi^3 G g_\star/90)^{1/2} T^2$ for radiation epoch, we can write

$$\Omega_{X,0} = \frac{8\pi G T_\gamma^3}{3H_0^2} \frac{H(M_X)}{M_X^2} \frac{x_f}{\langle\sigma v\rangle} \frac{g_{\star s}(T_\gamma)}{g_{\star s}(M_X)}. \tag{1.113}$$

Substituting the measured values of T_γ, H_0, using $g_{\star s}(T_\gamma) = 3.91$ and that $g_{\star s}(M_X) = g_\star(M_X)$, we get

$$\Omega_{X,0}h^2 \sim 0.1 \left(\frac{x_f}{10}\right) \left(\frac{10}{g_\star(M_X)}\right)^{1/2} \frac{10^{-8} GeV^{-2}}{\langle\sigma v\rangle} \tag{1.114}$$

It reproduces the DM density today if

$$\sqrt{\langle\sigma v\rangle} \sim 10^{-4} GeV^{-1} \sim 0.1\sqrt{G_F}, \tag{1.115}$$

which is in agreement with the cross-section of the weak interaction. The concordance of WIMPs relic abundance with the weak interaction scale is often called as "WIMP miracle".

DM particles have not been observed so far. Searches for these follow two directions: detection experiments, axion searches; and searches at accelerators and colliders. *pp* collisions are the experiments made by CMS and ATLAS collaborations at the LHC, including DM models that interact with the standard model via Higgs or Z boson exchange, Effective Field Theory (EFT) with heavy mediators, UV-complete models such as supersymmetry, and others [48–52].

On the other hand, detection experiments aim to observe elastic or inelastic scatters of Galactic DM particles with atomic nuclei, or with electrons in the detector material. The expected signals induced by DM particles are small and rare, mostly in the form of ionization, scintillation, or lattice vibrations. A set of astrophysical parameters are expected to detect, such as the local density ρ_0, the velocity distribution $f(\vec{v})$, the escape velocity v_{esc} as well as the DM mass and scattering cross-section. A review of the field including a list of ongoing direct detection experiments can be found here [53].

1.8 A good Standard Model, but an incomplete model

The ΛCDM model describes a homogeneous and isotropic expanding universe, assuming the (strong) Cosmological Principle, which is supported by CMB observations. Characterized by 6 independent parameters, this model provides a robust description of the history of the universe: since the Big Bang, in its dynamic evolution, the universe passed through different eras (radiation, matter, DE), with the elements decoupling as soon as their reaction rates become smaller than the expansion rate. Nevertheless, even the ΛCDM model is now established by various observations, it does not address some questions, some of them are listed below

◇ *Horizon problem*

The ΛCDM model is built on the pillar of the Cosmological Principle, which states

that we live in a homogeneous and isotropic universe. The model does not justify the origin of this homogeneity and isotropy, requiring an extra explanation given by *inflation* − a period of accelerated expansion which drives the primordial universe towards homogeneity and isotropy;

◇ *Cosmological constant problem*
As we saw in Eq. (1.18), the cosmological constant is a manifestation of the vacuum. Then, from particle physics, the vacuum energy can be computed by [54]:

$$\langle 0|T_{\mu\nu}|0\rangle = -\langle\rho\rangle g_{\mu\nu}, \tag{1.116}$$

where $\langle\rho\rangle \approx M^4/(16\pi^2)$ is obtained by summing zero-point energies of all normal modes of some field of mass m, with M representing some cutoff in the integration. Assuming that GR is valid up to the Planck scale, $M = 1/\sqrt{8\pi G}$, which gives $\langle\rho\rangle = 10^{71} GeV^4$. Thus, the value of the cosmological constant will be:

$$\Lambda = 8\pi G\langle\rho\rangle \sim 10^{38} GeV^2. \tag{1.117}$$

However, from cosmological data, we have:

$$\Lambda = 8\pi G\rho_0 = 3H_0^2 \sim 10^{-83} GeV^2, \tag{1.118}$$

which is very small compared with the value derived above. This disagreement of the order of $\sim 10^{121}$ between the theoretical estimate and the cosmologically determined value is known as the cosmological constant problem.

◇ *Dark-sector problem*
The ΛCDM model requires the existence of a dark sector representing $\sim 95\%$ of the universe content, having at least two components: DM and DE. As we discussed before, DM cannot be in baryonic form, with its particle candidate being out of the standard model of particle physics. In addition, the other unknown component, DE, represents most of the matter of the universe ($\sim 68\%$), and is required to explain its recent acceleration.

2 Modified Gravity & Dark Energy

As we presented in the previous chapter, the universe is well described by ΛCDM, a model based on GR, and that has at its core two unknown dark components, DM and DE, and smaller fractions of baryonic matter and radiation. In short, DM is proposed to explain the observed rotation galaxies curves, greater than the expected one by classical mechanics; DE, in turn, is an exotic fluid required to explain the late-time accelerated expansion of the universe − confirmed by several observations, including observations of the age of the universe compared to the oldest stars, CMB, BAO, LSS, and SNIa. This last one was the first strong observational evidence of the presence of DE in the universe, coming from the late 1990s [1, 2]. Fig. 5 shows two fits for 740 SNIa: one considering the presence of DE in the universe, while the other assumes the universe is only composed of ordinary matter.

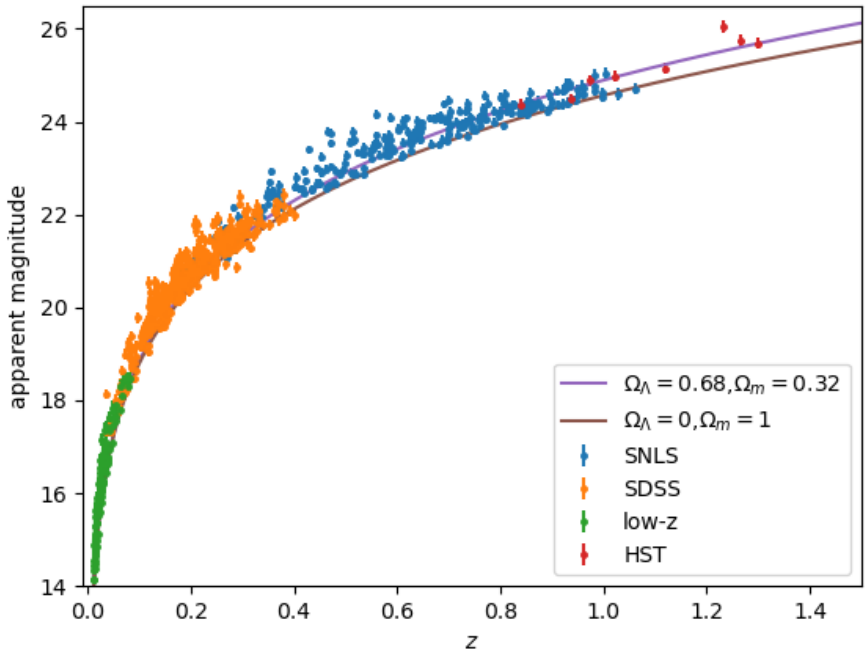

Figure 5 – Apparent magnitude versus redshift for 740 Type IA supernovae. The data are better fitted assuming a flat ΛCDM universe than the curve predicted by a matter-only universe ($\Omega_m = 1.0$). SDSS=Sloan Digital Sky Survey; SNLS=SuperNova Legacy Survey; HST=Hubble Space Telescope. Data were extracted from [55].

Although the ΛCDM gives a great description of the universe, such a model shows some limitations: it demands a cosmic component with negative pressure, attributed to the

cosmological constant, which has a smaller value than the quantum theory prediction; the tension on the value of the Hubble constant, and others. Also, besides the GR has been passed many tests within our solar system, its properties are poorly constrained aside from it, in other environments. These summarized reasons motivate the search for new physics beyond the standard model either with alternative models to DE or by proposing modifications of the GR. In this work, we will focus on the latter, where instead of the DE being the acceleration engine of the late universe, it would be caused by a modification of gravity theory on large scales.

Strictly speaking, what we call as MG proposals, actually are departures from Einstein's theory, made by invoking Lovelock's theorem, a powerful tool that provides a consistent way to create alternative theories of gravity from the metric tensor, as detailed below. Since the GR is a complete theory, *i.e.*, it fulfills the basic requirements of being a theory describing a single massless spin two field, maintaining the Lorentz invariance of equations, and since it also has passed a broad set of tests, any other scenario must reduce to GR at low scales in order to satisfy local tests of gravity. Many well-known MG models found in literature includes $f(R)$ theories [56], Brans-Dicke theories [57], Dvali-Gabadadze-Porrati braneworld [58], and Galileon gravity [59]. Here, we will explore the most general modification of GR, the Horndeski theories [8], a class of scalar-tensor theories, presented further below.

The cost of altering the current gravity theory is the modification of the growth of structure dynamics, which describes how LSS − galaxies and clusters of galaxies − scale with the cosmic time, given the expansion rate of the universe and the cosmic budget. Specifically, the Poisson equation relating over-densities to the gravitational potential, Φ, and the Weyl potential, $\Psi + \Phi$, describing the geodesics of relativistic particles, differ from the standard case (see Eq.s 2.61*a*, and 2.61*b*). Redshift-Space Distortions (RSD) and Weak Lensing (WL) are powerful probes for the growth of structure − complementary to BAO, and CMB measurements −, allowing us to distinguish between MG theories and DE models by imposing constraints on their respective parameters − in particular, we discuss RSD effects in Subsec. 3.2.4. Model-independent tests to detect MG effects from the growth of structures can usually be done through the *growth index formalism* [60, 107], or by specifying some parameterization for the gravitational potentials (Subsec. 2.1.8). In order to put a validity range for the classes of Horndeski theories studied in this work[1], we can notice that observations of LSS is divided into two regimes

- ◇ Large Scales ($\gtrsim$ 100 Mpc): In this regime, density perturbations are much smaller than one, which enable us to apply a perturbative treatment, making accurate theoretical predictions for the growth of structure;

[1] From both theoretical and observational motivations, fluctuations on the scalar field are only considered at the linear level.

- ◇ Smaller Scales ($\lesssim 10$ Mpc): In these scales, density fluctuations become non-linear, and so that the perturbative treatment fails. Instead, predictions on MG theories can be made through N-body simulations.

The chapter is organized as follows: starting from the Lovelock's theorem, we introduce the Horndeski gravity; then, we expand order-by-order in perturbations to scalar quantities a general action written in terms of Arnowitt-Deser-Misner (ADM) variables, and get the correspondent Horndeski perturbed action; later, we take the coefficients of perturbed quantities to form a phenomenological α-basis; finally, we discuss a sub-class of Horndeski theories coming from GW170817 & GRB170817A bounds, and give two commonly used parameterizations for the α_i functions, implementable in HI_CLASS, a Boltzmann solver.

2.1 Horndeski Theories

In 1971, D. Lovelock presented a powerful theorem from which alternative theories of gravity can be constructed as a deviation of the shortlist of its conditions [7]. This theorem establishes that if we try to create any gravity theory from the metric tensor *alone*, then the only field equations that are second-order or less are Einstein equations and/or a cosmological constant. In other words, from the principle of the least action, the only possible second-order Euler-Lagrange expression obtainable in a 4-dimensional space from a scalar density of the form $\mathcal{L} = \mathcal{L}(g_{\mu\nu})$ is

$$E^{\mu\nu} = \alpha\sqrt{-g}\left[R^{\mu\nu} - \frac{1}{2}g^{\mu\nu}R\right] + \lambda\sqrt{-g}g^{\mu\nu}, \tag{2.1}$$

where α and λ are constants; $R^{\mu\nu}$ and R are the Ricci tensor and the scalar curvature, respectively, and the action of $E^{\mu\nu}$ on any Lagrangian, $\mathcal{L}$, is defined as

$$E^{\mu\nu}[\mathcal{L}] = \frac{d}{dx^\rho}\left[\frac{\partial\mathcal{L}}{\partial g_{\mu\nu,\rho}} - \frac{d}{dx^\lambda}\left(\frac{\partial\mathcal{L}}{\partial g_{\mu\nu,\rho\lambda}}\right)\right] - \frac{\partial\mathcal{L}}{\partial g_{\mu\nu}}. \tag{2.2}$$

Thus, MG theories with field equations that differ from those of GR can be created by doing one (or more) of what follows

1. Consider other fields beside the metric tensor;
2. Accept higher than second derivatives of the metric in the field equations;
3. Work in a space with dimensionality different from four;
4. Give up on either rank (2, 0) tensor field equations, symmetry of the field equations under exchange of indices, or divergence-free field equations.

What Lovelock's doctoral student, G. Horndeski did in 1974 was to break condition 1, introducing a single scalar field into the Einstein-Hilbert action, whilst maintaining second-order equations of motion, without breaking other conditions. The Horndeski action reads

$$\begin{aligned} S &= \int d^4x\sqrt{-g}\sum_{i=2}^{5}\mathcal{L}_i, \\ \mathcal{L}_2 &= G_2(\phi, X), \\ \mathcal{L}_3 &= -G_3(\phi, X)\Box\phi, \\ \mathcal{L}_4 &= G_4(\phi, X)R + G_{4X}(\phi, X)[(\Box\phi)^2 - \phi_{;\mu\nu}\phi^{;\mu\nu}], \\ \mathcal{L}_5 &= G_5(\phi, X)G_{\mu\nu}\phi^{;\mu\nu} - \frac{1}{6}G_{5X}(\phi, X)[(\Box\phi)^3 + 2\phi_{;\mu}{}^{\nu}\phi_{;\nu}{}^{\alpha}\phi_{;\alpha}{}^{\mu} - 3\phi_{;\mu\nu}\phi^{;\mu\nu}\Box\phi], \end{aligned} \tag{2.3}$$

where $G_i(i = 2, 3, 4, 5)$ are functions of the scalar field, ϕ, and its canonical kinetic energy $X \equiv -\nabla^\mu\phi\nabla_\mu\phi/2$; $G_{iX} = \partial G_i/\partial X$ are the partial derivatives; R is the Ricci scalar; $G_{\mu\nu} = R_{\mu\nu} - \frac{1}{2}g_{\mu\nu}R$ is the Einstein tensor. G_2 is called as the k-*essence* term, $-G_3(\phi, X)\Box\phi$ is the cubic Galileon term, $G_4(\phi, X)$ is the generalization of the Einstein-Hilbert term, and $G_5(\phi, X)G_{\mu\nu}\phi^{;\mu\nu}$ is the non-minimal derivative coupling to Einstein tensor. The short notation for the remaining kinetic terms are explicitly written as

$$\Box\phi = g^{\mu\nu}\nabla_\mu\nabla_\nu\phi, \tag{2.4a}$$

$$\phi_{;\mu\nu}\phi^{;\mu\nu} = \nabla^\mu\nabla^\nu\phi\nabla_\mu\nabla_\nu\phi, \tag{2.4b}$$

$$\phi_{;\mu}{}^{\nu}\phi_{;\nu}{}^{\alpha}\phi_{;\alpha}{}^{\mu} = \nabla_\mu\nabla_\nu\phi\nabla^\nu\nabla^\alpha\phi\nabla_\alpha\nabla^\mu\phi. \tag{2.4c}$$

Many well-known models can be seen as sub-classes of Horndeski gravity. For the examples cited early, they are obtained through specific choices of the G_i functions

- ◇ ΛCDM: $G_4 = \frac{R-2\Lambda}{16\pi G}$, $G_2 = G_3 = G_5 = 0$;
- ◇ $f(R)$ theories: $G_2 = (Rf_{,R} - f)$, $G_4 = \frac{f_{,R}}{16\pi G}$, $G_3 = G_5 = 0$;
- ◇ Brans-Dicke theory: $G_2 = -\frac{\omega_{BD}X}{16\pi\phi}$, $G_4 = \frac{\phi}{16\pi}$, $G_3 = G_5 = 0$;
- ◇ Galileon gravity: $G_2 = c_2X$, $G_3 = c_3m^{-3}X$, $G_4 = \frac{1}{16\pi G} + c_4m^{-6}X^2$, $G_5 = c_5m^{-9}X^2$.

2.1.1 Linear Perturbations

Given an MG theory, we need to re-derive the evolution equations for the structure formation in order to study its properties and to understand how it differs from GR. We apply the perturbative treatment on the action describing the theory, and use the observed inhomogeneities in the LSS to constrain coefficients of the expanded fields. In fact, this procedure gives a set of second-order coupled equations in linear field perturbations, which

can be solved numerically, enabling us to seek how the gravitational potentials evolve with time. We start considering the unitary gauge and use it to construct a general action for perturbations, written in terms of 3-dimensional scalar quantities (ADM variables), which does not rely on any specific model. Such action provides the so-called EFT framework, a formalism applied to the inflationary theory and DE/MG models [61].

2.1.1.1 Unitary Gauge

The Horndeski scalar field can be thought as a Goldstone boson that breaks time translations of an expanding universe. We can recover this symmetry by defining the unitary gauge as follows[2]. Decomposing the scalar field in a perturbed FLRW universe as $\phi(t,\vec{x}) = \bar{\phi}(t)+\delta\phi(t,\vec{x})$, the unitary gauge corresponds to the choice of a time coordinate such that $\delta\phi(t,\vec{x}) = 0$. Then, t becomes a function of ϕ, defining a preferred time slicing ($\phi = const$) in which constant time hypersurfaces, $\Omega(t)$, coincide with constant scalar field hypersurface, $\Omega(\phi)$.

From the unitary gauge it is possible to write down a generic Lagrangian for cosmological perturbations, since we only have to worry about metric perturbations, with ϕ been absorbed by the metric[3]. Instead of ϕ, the generic action is written in terms of 4-dimensional invariant scalars, and 3-dimensional objects living on $t = const$, called ADM variables [64]. Such terms are built from contractions of tensors with the unity vector, n_μ, which can be seen, in a fluid point of view, as the velocity of the scalar field, orthogonal to the constant time hypersurfaces, and defined as

$$n_\mu = -\frac{\partial_\mu\phi}{\sqrt{-(\partial_\mu\phi)^2}}. \tag{2.5}$$

For instance, the *extrinsic* curvature tensor and its trace − presented below − are given by $K_{\mu\nu} = h_\mu{}^\sigma\nabla_\sigma n_\nu$ and $K = \nabla^\nu n_\nu$, with $h_{\mu\nu} = g_{\mu\nu} + n_\mu n_\nu$ been the induced metric. Then, writing down the line element of FLRW metric in terms of ADM variables [9]

$$ds^2 \;=\; -N^2dt^2 + \gamma_{ij}(dx^i + N^i dt)(dx^j + N^j dt), \tag{2.6}$$

where γ_{ij} is the 3-dimensional spatial metric; N and N^i are called *lapse* and *shift* functions, respectively, the general action reads

$$S = \int d^4x\sqrt{-g}\mathcal{L}(N, K, \mathcal{S}, \mathcal{R}, \mathcal{Z}; t), \tag{2.7}$$

where the four scalar quantities are

$$K \equiv K^\mu_\mu, \qquad \mathcal{R} \equiv {}^{(3)}R \equiv {}^{(3)}R^\mu_\mu, \qquad \mathcal{S} \equiv K_{\mu\nu}K^{\mu\nu}, \qquad \mathcal{Z} \equiv {}^{(3)}R_{\mu\nu}\,{}^{(3)}R_{\mu\nu}. \tag{2.8}$$

[2] The unitary gauge was introduced by S. Weinberg in 1971 [62], in the context of the EW spontaneous symmetry breaking, and applied later in cosmology by H. Kodama and M. Sasaki, in 1984 [63].

[3] To be clear, the unitary gauge yields $n_\mu = -\frac{\partial_\mu\phi}{\sqrt{-(\partial_\mu\phi)^2}} \to -\frac{\delta^0_\mu}{\sqrt{-g^{00}}}$.

with ${}^{(3)}R_{\mu\nu}$ called the *intrinsic* curvature tensor. Now, we expand the action (2.7) order-by-order in these fields, maintaining only the linear perturbations.

2.1.1.2 $\mathcal{O}^0$ Perturbations

The background equations can be obtained by writing the flat FLRW metric in terms of ADM variables as

$$ds^2 = -\bar{N}^2 dt^2 + a^2 \delta_{ij} dx^i dx^j. \tag{2.9}$$

where $K = 3H/\bar{N}$ and $\mathcal{S} = 3H^2/\bar{N}^2$. Substituting this line element into Eq. (2.7), and varying that action with respect to lapse and scale factor, we obtain

$$\delta S^{(0)} = \int d^4x \left[a^3(\bar{\mathcal{L}} + \mathcal{L}_N - 3H\mathcal{F})\delta\bar{N} + 3a^2(\bar{\mathcal{L}} - 3H\mathcal{F} - \dot{\mathcal{F}})\delta a \right], \tag{2.10}$$

where $\sqrt{-g} = a^3\bar{N}$, and

$$\mathcal{F} \equiv 2H\mathcal{L}_{\mathcal{S}} + \mathcal{L}_K, \tag{2.11}$$

with $\mathcal{L}_N = \partial\mathcal{L}/\partial\bar{N}$, etc. Then, making the lapse function $\bar{N} = 1$[4], the Friedmann equations read

$$3H\mathcal{F} - \bar{\mathcal{L}} - \mathcal{L}_N = 0, \tag{2.12a}$$

$$\dot{\mathcal{F}} + 3H\mathcal{F} - \bar{\mathcal{L}} = 0. \tag{2.12b}$$

2.1.1.3 $\mathcal{O}^1$ Perturbations

For the first-order perturbation, we note that $\sqrt{-g} = \sqrt{h}N$, where h is the determinant of the induced metric, and $N = \bar{N} + \delta N$. Thus,

$$S^{(1)} = \int d^4x \left[(\bar{\mathcal{L}} - 3H\mathcal{F} - \dot{\mathcal{F}})\delta\sqrt{h} + a^3(\bar{\mathcal{L}} + \mathcal{L}_N - 3H\mathcal{F})\delta N + a^3\mathcal{L}_{\mathcal{R}}\delta\mathcal{R} \right], \tag{2.13}$$

which vanishes by using Eq.s (2.12*a*) and (2.12*b*) – the last term can be ignored because it is a total derivative.

2.1.1.4 $\mathcal{O}^2$ Perturbations

From the metric (2.6), and the first-order perturbation $\delta\sqrt{-g} = \delta\sqrt{h} + a^3\delta N$, the action (2.7), at second-order, reads

$$\begin{aligned} S^{(2)} = & \int d^4x \left\{ \delta\sqrt{h} \left[(\dot{\mathcal{F}} + \mathcal{L}_N)\delta N + \mathcal{L}_{\mathcal{R}}\delta\mathcal{R} \right] + \right. \\ & + a^3 \left[\left(\mathcal{L}_N + \frac{1}{2}\mathcal{L}_{NN} \right) \delta N^2 + \mathcal{L}_{\mathcal{R}}\delta_2\mathcal{R} + \frac{1}{2}\mathcal{A}\delta K^2 + \mathcal{B}\delta K\delta N + \mathcal{C}\delta K\delta\mathcal{R} + \right. \\ & \left. \left. + \mathcal{L}_{\mathcal{S}}\delta K^\mu_\nu \delta K^\nu_\mu + \mathcal{L}_{\mathcal{Z}}\delta\mathcal{R}^\mu_\nu\delta\mathcal{R}^\nu_\mu + \frac{1}{2}\mathcal{L}_{\mathcal{R}\mathcal{R}}\delta\mathcal{R}^2 + (\mathcal{L}_{\mathcal{R}} + \mathcal{L}_{N\mathcal{R}}\delta N\delta\mathcal{R}) \right] \right\}, \end{aligned} \tag{2.14}$$

[4] From now, we will always make this for the final expressions.

where $\delta_2\mathcal{R}$ denotes the second-order perturbation of $\mathcal{R}$, and we have defined

$$\mathcal{A} \equiv 4H^2\mathcal{L}_{\mathcal{SS}} + 4H\mathcal{L}_{\mathcal{SK}} + \mathcal{L}_{KK}, \tag{2.15a}$$

$$\mathcal{B} \equiv 2H\mathcal{L}_{\mathcal{SN}} + \mathcal{L}_{KN}, \tag{2.15b}$$

$$\mathcal{C} \equiv 2H\mathcal{L}_{\mathcal{SR}} + \mathcal{L}_{K\mathcal{R}}. \tag{2.15c}$$

We can split up the second-order action (2.14) into *scalar* and *tensorial* modes.

(i) Tensorial modes:

First, considering the tensorial part of the metric (2.6), explicitly written as

$$\gamma_{ij} = a^2(t)\left(\delta_{ij} + h_{ij}\right), \tag{2.16}$$

with h_{ij} traceless and divergenceless, *i.e.*, $h^i_i = 0$ and $\partial^i h_{ij} = 0$, the action (2.7), at second-order perturbations reads

$$S_T^{(2)} = \frac{1}{4}\int d^4x a^3 \left(\mathcal{A}\dot{h}_{ij}^2 - \frac{\mathcal{D}}{a^2}(\partial_k h_{ij})^2\right). \tag{2.17}$$

where $\mathcal{D} \equiv \mathcal{L}_{\mathcal{R}} + \dot{\mathcal{C}}/2N + H\mathcal{C}$. The GR is recovered if we set $\mathcal{A} = \mathcal{D} = M_{Pl}/2$, which gives the propagation of the Gravitational Wave (GW). For most general theories of gravity, it will be useful to define the *effective Planck mass*, and the *tensorial sound speed (squared)*, respectively given by

$$M_*^2 \equiv 2\mathcal{A}, \tag{2.18a}$$

$$c_T^2 \equiv \frac{\mathcal{D}}{\mathcal{A}} = 1 + \alpha_T, \tag{2.18b}$$

where α_T denotes the GWs speed deviation from the light speed (squared). With these definitions, we can rewrite the Eq. (2.17) as

$$S_T^{(2)} = \frac{1}{8}\int d^4x a^3 M_*^2 \left(\dot{h}_{ij}^2 - \frac{c_T^2}{a^2}(\partial_k h_{ij})^2\right). \tag{2.19}$$

(ii) Scalar modes:

The scalar modes of the action (2.14) is given by writing the spatial part of the metric (2.6) in terms of ζ [65],

$$\gamma_{ij} = a^2(t)e^{2\zeta}\delta_{ij}. \tag{2.20}$$

As a function of ζ, we can write

$$\delta\sqrt{h} = 3a^3\zeta \qquad \textit{and} \qquad \delta_2\mathcal{R} = -\frac{2}{a^2}[(\partial_i\zeta)^2 - 4\zeta\partial^2\zeta]. \tag{2.21}$$

In order to obtain the second-order action as a function of ζ alone, we proceed to the calculation of two constraints: the Hamiltonian and the momentum equations. The first one is obtained by varying the action (2.14) with respect to δN

$$[\mathcal{L}_{NN}+2\mathcal{L}_N+3H(3H\mathcal{A}+2H\mathcal{L}_\mathcal{S}-2\mathcal{B})]\delta N-(\mathcal{B}-3H\mathcal{A}-2H\mathcal{L}_\mathcal{S})\frac{\partial^2\psi}{a^2}+$$
$$+3(\mathcal{B}-3H\mathcal{A}-2H\mathcal{L}_\mathcal{S})\dot{\zeta}-4(\mathcal{L}_\mathcal{R}+\mathcal{L}_{N\mathcal{R}}-3H\mathcal{C})\frac{\partial^2\zeta}{a^2}+3(\mathcal{L}_N+\dot{\mathcal{F}})\zeta=0. \tag{2.22}$$

On the other hand, varying the action with respect to the shift $N_i\equiv\partial_i\psi$, we get the momentum equation

$$-(\mathcal{B}-3H\mathcal{A}-2H\mathcal{L}_\mathcal{S})\delta N+(\mathcal{A}+2\mathcal{L}_\mathcal{S})\frac{\partial^2\psi}{a^2}=(3\mathcal{A}+2\mathcal{L}_\mathcal{S})\dot{\zeta}-4\mathcal{C}\frac{\partial^2\zeta}{a^2}. \tag{2.23}$$

The second-order action contains the terms

$$\frac{1}{a}\left[\frac{1}{2}(\mathcal{A}+2\mathcal{L}_\mathcal{S})(\partial^2\psi)^2+4\mathcal{C}\partial^2\psi\partial^2\zeta+2(4\mathcal{L}_{\mathcal{R}\mathcal{R}}+3\mathcal{L}_\mathcal{Z})(\partial^2\zeta)^2\right]. \tag{2.24}$$

which impose three conditions constraints,

$$\mathcal{A}+2\mathcal{L}_\mathcal{S}=0, \qquad \mathcal{C}=0, \qquad 4\mathcal{L}_{\mathcal{R}\mathcal{R}}+3\mathcal{L}_\mathcal{Z}=0. \tag{2.25}$$

So, taking in account such conditions, the momentum constraint (2.23) implies that

$$\delta N=\mathcal{F}\dot{\zeta}, \qquad \textit{with} \qquad \mathcal{F}\equiv\frac{4\mathcal{L}_\mathcal{S}}{\mathcal{B}+4H\mathcal{L}_\mathcal{S}}. \tag{2.26}$$

Substituting this result in the Hamiltonian constraint, and after integration by parts, we get the second-order action for scalar modes

$$S_s^{(2)}=\frac{1}{2}\int d^4x a^3\left[\mathcal{L}_{\dot{\zeta}\dot{\zeta}}\dot{\zeta}^2+\mathcal{L}_{\partial_i\zeta\partial_i\zeta}\frac{(\partial_i\zeta)^2}{a^2}\right], \tag{2.27}$$

where

$$\mathcal{L}_{\dot{\zeta}\dot{\zeta}} \equiv 2\left(\frac{1}{2}\mathcal{L}_{NN}+\mathcal{L}_N-3H\mathcal{B}-6H^2\mathcal{L}_S\right)\mathcal{F}^2+12\mathcal{L}_\mathcal{S}, \tag{2.28a}$$
$$\mathcal{L}_{\partial_i\zeta\partial_i\zeta} \equiv 4\left[\mathcal{L}_\mathcal{R}-\frac{1}{a}\frac{d}{dt}(a\mathcal{G})\right], \qquad \textit{with} \qquad \mathcal{G}\equiv\mathcal{F}(\mathcal{L}_\mathcal{R}+\mathcal{L}_{N\mathcal{R}}). \tag{2.28b}$$

Defining the *kinetic braiding*,

$$\alpha_B\equiv\frac{\mathcal{B}}{4\mathcal{A}}, \tag{2.29}$$

we can rewrite the action (2.27) as

$$S_s^{(2)}=\int d^4x a^3 Q_s\left[\dot{\zeta}^2+\frac{c_s^2}{a^2}(\partial_i\zeta)^2\right], \tag{2.30}$$

where

$$Q_s \equiv \frac{2M_*^2 E}{(2-\alpha_B)^2}, \qquad E \equiv \alpha_K + \frac{3}{2}\alpha_B^2, \qquad \alpha_K \equiv \frac{2\mathcal{L}_N + \mathcal{L}_{NN}}{2H^2\mathcal{A}}, \tag{2.31}$$

and the sound speed squared is defined as

$$c_s^2 \equiv -\frac{\mathcal{L}_{\partial_i\zeta\partial_i\zeta}}{\mathcal{L}_{\dot{\zeta}\dot{\zeta}}} = -\frac{(2-\alpha_B)[\dot{H} - \frac{1}{2}H^2\alpha_B(1+\alpha_T) - H^2(\alpha_M - \alpha_T)] - H\dot{\alpha}_B}{H^2 E} \tag{2.32}$$

with

$$\alpha_M \equiv \frac{1}{H}\frac{d}{dt} ln M_*^2. \tag{2.33}$$

Putting the final expressions for these modes together, we get

$$S^{(2)} = \int d^4x a^3 \left[Q_s \left(\dot{\zeta}^2 + \frac{c_s^2}{a^2}(\partial_i\zeta)^2 \right) + Q_T \left(\dot{h}_{ij}^2 - \frac{c_T^2}{a^2}(\partial_k h_{ij})^2 \right) \right], \tag{2.34}$$

where $Q_T \equiv M_*^2/8$. Now, we analyze the stability conditions of the theory.

2.1.2 Stability Conditions

The solutions to the background equations can be affected by mainly two types of instabilities, *gradient* and *ghost* ones, becoming no longer appropriate. The former occurs when the speed of sound squared of the perturbations is negative, leading to an exponential destabilization of the perturbations at small scales; the latter occurs when the sign of the kinetic term is wrong, giving a negative energy modes [66]. In order to avoid such instabilities, from Eq.s (2.18*a*), (2.18*b*), (2.31) and (2.32) we require that

$$Q_s > 0, \qquad c_s^2 > 0, \qquad M_*^2 > 0, \qquad \textit{and} \qquad c_T^2 > 0. \tag{2.35}$$

2.1.3 α-basis

From the action (2.3), the perturbed second-order action (2.14) consists of a sum of terms, quadratic in perturbed fields, each of which is multiplied by time-dependent coefficients, which only rely on the background cosmology. In order to clear physical effects of Horndeski gravity, such coefficients are taken to form a basis, described by 4 phenomenological functions,

$\alpha_M, \alpha_B, \alpha_K, \alpha_T$, defined as [10]

$$
\begin{aligned}
HM_*^2\alpha_M &\equiv \frac{d}{dt}M_*^2, \qquad with \qquad M_*^2 \equiv 2(G_4 - 2XG_{4X} + XG_{5\phi} - \dot{\phi}HXG_{5X}) && \text{(2.36a)}\\
HM_*^2\alpha_B &\equiv 2\dot{\phi}(XG_{3X} - G_{4\phi} - 2XG_{4\phi X}) + \\
&+ 8XH(G_{4X} + 2XG_{4XX} - G_{5\phi} - XG_{5\phi X}) + \\
&+ 2\dot{\phi}XH^2(3G_{5X} + 2XG_{5XX}), && \text{(2.36b)}\\
H^2M_*^2\alpha_K &\equiv 2X(G_{2X} + 2XG_{2XX} - 2G_{3\phi} - 2XG_{3\phi X}) + \\
&+ 12\dot{\phi}XH(G_{3X} + XG_{3XX} - 3G_{4\phi X} - 2XG_{4\phi XX}) + \\
&+ 12XH^2(G_{4X} + 8XG_{4XX} + 4X^2G_{4XXX}) - \\
&- 12XH^2(G_{5\phi} + 5XG_{5\phi X} + 2X^2G_{5\phi XX}) + \\
&+ 4\dot{\phi}XH^3(3G_{5X} + 7XG_{5XX} + 2X^2G_{5XXX}), && \text{(2.36c)}\\
M_*^2\alpha_T &\equiv 2X[2G_{4X} - 2G_{5\phi} - (\ddot{\phi} - \dot{\phi}H)G_{5X}]. && \text{(2.36d)}
\end{aligned}
$$

The coefficients of the perturbed fields arranged in this way have the advantage of separating the background history from the perturbed α_i functions − this is particularly important because it allows us to set up the background expansion to the ΛCDM cosmology, and to seek for departures from the standard scenario just looking at the α_i variables. The physical interpretation of the α_i is

- ◇ α_M is the *running Planck mass*. This function parameterizes the time evolution of the effective Planck mass, M_*^2. It has contributions from G_4 and G_5;
- ◇ α_B is called *braiding* function. This function quantifies the coupling between the metric and the DE field. It also regulates the clustering of DE, and has contributions from G_3, G_4 and G_5;
- ◇ α_K is called *kineticity* function. This function measures the dynamics of scalar field, *i.e.*, it arises from the kinetic energy term. It has contributions from all G_i functions;
- ◇ α_T is the *tensor speed excess*. It describes the deviation of the speed of propagation of GWs from the speed of light, as shown in the Eq. (2.18*b*). It has contributions from G_4 and G_5.

In theories beyond Horndeski, the derivatives G_{4X} and G_{5X} that appear in the fourth and fifth lines of Eq. (2.3) are replaced by more general functions, which generates equation of motion with higher order derivatives − also immune from Ostrogradski's instabilities. Such functions are parameterized by a fifty α_H. In terms of G_i, α_H is more complicated, and so we recommend the reader to see [67] for more details. Since the Horndeski Lagrangian

describes all theories with at most second-order derivatives in their equations of motion on the FLRW background, this approach is connected to EFT for DE, just differing from that by a redefinition of variables [9, 68–70]. We also note that the ΛCDM is recovered when $\alpha_i \to 0$ *together*, and $M_*^2 \to 1$.

2.1.4 Horndeski Theories after GW170817 & GRB170817A

The Horndeski theories were almost entirely ruled-out after the nearly simultaneous detection of GWs from a neutron star merger (GW170817) and its counterpart (GRB170817A). The event put a tight constraint on the GWs speed [71–73]

$$-3 \times 10^{-15} \leq c_T - 1 \leq 7 \times 10^{-16}. \tag{2.37}$$

Such a bound has had consequences for scalar-tensor theories, and also for other types of DE models. From an EFT point of view, it was shown by [74, 75] that the bound (2.37) was sufficient to suppress some operators that predict non-luminal gravitational propagation. At a first look, for Horndeski case, from definitions (2.18*b*) and (2.36*d*) we have

$$c_T^2 = \frac{G_4 - X(\ddot{\phi} G_{5X} + G_{5\phi})}{G_4 - 2XG_{4X} - X(H\dot{\phi} G_{5X} - G_{5\phi})}. \tag{2.38}$$

The bound $c_T = 1$ can be satisfied if we set, for instance, $G_{4X} = 0$ and $G_5 = 0$ − note that it yields $\alpha_T = 0$ from Eq. (2.18*b*). Then, the result is a sub-class of Horndeski theories which the Lagrangian reads

$$\mathcal{L} = G_2(\phi, X) - G_3(\phi, X)\Box\phi + G_4(\phi)R. \tag{2.39}$$

However, as pointed out by [76], we must recall that the recent LIGO bound applies to GWs at a frequency of 10−100Hz, which differs from cosmological energy scales by 20 orders of magnitude (smaller). Also, the speed of GWs may depend on the frequency at which it is measured, $c_T = c_T(k)$, and so it is not scale/time/energy-independent. Thus, in our analysis, we also consider values for α_T slightly different from 0.

2.1.5 Structure Formation

MG theories modify the gravitational potentials Φ and Ψ, affecting how structure grows − the former, the nonrelativistic potential, governs the motion of matter, while the combination Ψ + Φ, sometimes called Weyl potential, determines the geodesics of relativistic particles. To obtain such potentials, let us derive their perturbed evolution equations.

2.1.5.1 Background Equations

First, let us consider the Horndeski background. From Eq.s (2.12*a*) and (2.12*b*), the Friedmann equations from the action (2.3) reads

$$3H^2 = \tilde{\rho}_m + \tilde{\mathcal{E}} \tag{2.40a}$$

$$2\dot{H} + 3H^2 = -\tilde{p}_m - \tilde{\mathcal{P}}, \tag{2.40b}$$

where the tild indicates that all the quantities are divided by the effective Planck mass, M_*^2, and,

$$\begin{aligned} M_*^2\tilde{\mathcal{E}} &\equiv -G_2 + 2X(G_{2X} - G_{3\phi}) + 6\dot{\phi}H(XG_{3X} - G_{4\phi} - 2XG_{4\phi X}) + \\ &+ 12H^2X(G_{4X} + 2XG_{4XX} - G_{5\phi} - XG_{5\phi X}) + 4\dot{\phi}H^3X(G_{5X} + XG_{5XX}), \end{aligned} \tag{2.41a}$$

$$\begin{aligned} M_*^2\tilde{\mathcal{P}} &\equiv G_2 - 2X(G_{3\phi} - 2G_{4\phi\phi}) + 4\dot{\phi}H(G_{4\phi} - 2XG_{4\phi X} + XG_{5\phi\phi}) - \\ &- M_*^2\alpha_B H\frac{\ddot{\phi}}{\dot{\phi}} - 4H^2X^2G_{5\phi X} + 2\dot{\phi}H^3XG_{5X}. \end{aligned} \tag{2.41b}$$

As a consequence of absorbing the time-evolving Planck mass in the definition of the tilded quantities, the energy density is not necessarily covariantly conserved; rather, there is an exchanged between the scalar and matter subsystems whenever the value of M_*^2 changes, as described by the equations

$$\dot{\tilde{\rho}}_m + 3H(\tilde{\rho}_m + \tilde{p}_m) = -\alpha_M H\tilde{\rho}_m, \tag{2.42a}$$

$$\dot{\tilde{\mathcal{E}}} + 3H(\tilde{\mathcal{E}} + \tilde{\mathcal{P}}) = \alpha_M H\tilde{\rho}_m. \tag{2.42b}$$

Also, varying the action (2.3) with respect to $\phi = \phi(t)$ gives the scalar-field equation of motion

$$\dot{n} + 3Hn = \mathcal{P}_\phi, \tag{2.43}$$

where

$$\begin{aligned} n &\equiv \dot{\phi}(G_{2X} - 2G_{3\phi}) + 6HX(G_{3X} - 2G_{4\phi X}) + \\ &+ 6H^2\dot{\phi}(G_{4X} + 2XG_{4XX} - G_{5\phi} - XG_{5\phi X}) + \\ &+ 2H^3X(3G_{5X} + 2XG_{5XX}), \end{aligned} \tag{2.44a}$$

$$\begin{aligned} \mathcal{P}_\phi &\equiv G_{2\phi} - 2XG_{3\phi\phi} + 2\ddot{\phi}(XG_{3\phi X} + 3H\dot{\phi}G_{4\phi X}) + 6\dot{H}G_{4\phi} + \\ &+ 6H^2(2G_{4\phi} + 2XG_{4\phi X} - XG_{5\phi\phi}) + 2H^3\dot{\phi}XG_{5\phi X}. \end{aligned} \tag{2.44b}$$

2.1.5.2 Evolution of Perturbations

Now, we consider small perturbations around the FLRW background, in the Newtonian gauge, described by the metric

$$ds^2 = -(1 + 2\Psi)dt^2 + a^2(1 - 2\Phi)dx^2. \tag{2.45}$$

Horndeski theories modify the evolution of standard cosmological perturbations through the α_i functions, and by introducing a dynamical potential, v_X. Invariant under the reparameterizations, such a potential is defined as

$$v_X \equiv -\frac{\delta\phi}{\dot{\bar{\phi}}}, \tag{2.46}$$

which can be interpreted as a potential for a peculiar velocity field, when appropriately normalised. The perturbation $\delta\phi$ is given by the *background value of the scalar field*, evaluated on perturbed constant time hypersurface

$$\delta\phi(t,\vec{x}) \equiv \bar{\phi}[t + \delta t(t,\vec{x})]. \tag{2.47}$$

The coefficients for the gravitational potentials equations are modified from their standard values as follows: On the left-hand side, there is the contribution of the scalar field potential; on the right-hand side appears the contribution of all matter sources: DM, baryons, photons and neutrinos

◇ Einstein (00)

$$\lambda_1\dot{v}_X + \lambda_2 v_X - 3(2-\alpha_B)H\dot{\Phi} - \frac{2k^2}{a^2}\Phi - (6-\alpha_K-6\alpha_B)H^2\Psi = \tilde{\rho}_m\delta_m, \tag{2.48}$$

◇ Einstein ($0i$)

$$\alpha_B H\dot{v}_X + \lambda_3 v_X - 2\dot{\Phi} - (2-\alpha_B)H\Psi = (\tilde{\rho}_m + \tilde{p}_m)v_m, \tag{2.49}$$

◇ Einstein (ij) Traceless

$$\lambda_4 v_X + \Psi - (1+\alpha_T)\Phi = \tilde{p}_m\pi_m, \tag{2.50}$$

◇ Einstein (ij) Trace

$$\alpha_B H\ddot{v}_X + \lambda_6\dot{v}_X + \lambda_7 v_X - 2\ddot{\Phi} - 2(3+\alpha_M)H\dot{\Phi} - (2-\alpha_B)H\dot{\Psi} - \lambda_5\Psi = -\frac{\delta p_m}{M_*^2}, \tag{2.51}$$

◇ Scalar Field Perturbations

$$\begin{aligned} H^2\alpha_K\ddot{v}_X &+ \lambda_{10}\dot{v}_X + (H^2M^2+\lambda_{11})v_X + 3H\alpha_B\ddot{\Phi} - \lambda_8\dot{\Phi} - 2(\alpha_M-\alpha_T)H\frac{k^2}{a^2}\Phi + \\ &+ (\alpha_K+3\alpha_B)H^2\dot{\Psi} - \left(\alpha_B H\frac{k^2}{a^2} + \lambda_9\right)\Psi = 0, \end{aligned} \tag{2.52}$$

where the coefficients λ_i and H^2M^2 are given by

$$\lambda_1 \equiv (\alpha_K + 3\alpha_B)H^2, \tag{2.53a}$$
$$\lambda_2 \equiv \left[\left(\frac{k^2}{a^2} - 3\dot{H}\right)\alpha_B + 3(2\dot{H} + \tilde{\rho}_m + \tilde{p}_m)\right] H, \tag{2.53b}$$
$$\lambda_3 \equiv 2\dot{H} + \tilde{\rho}_m + \tilde{p}_m, \tag{2.53c}$$
$$\lambda_4 \equiv (\alpha_T - \alpha_M)H, \tag{2.53d}$$
$$\lambda_5 \equiv H^2(2 - \alpha_B)(3 + \alpha_M) - \alpha_B H + 4\dot{H} - \lambda_3, \tag{2.53e}$$
$$\lambda_6 \equiv \lambda_3 + \alpha_B H + H^2\alpha_B(3 + \alpha_M), \tag{2.53f}$$
$$\lambda_7 \equiv 2\ddot{H} + 2\dot{H}H(3 + \alpha_M) + \dot{\tilde{p}}_m + \alpha_M H\tilde{p}_m, \tag{2.53g}$$
$$\lambda_8 \equiv 3\left[\lambda_3 - H^2\alpha_B(3 + \alpha_M) - (\alpha_B H)\right], \tag{2.53h}$$
$$\lambda_9 \equiv H\left[3\lambda_3 - \dot{H}(2\alpha_K + 9\alpha_B) - H(\dot{\alpha}_K + 3\dot{\alpha}_B) - H^2(3 + \alpha_M)(\alpha_K + 3\alpha_B)\right] \tag{2.53i}$$
$$\lambda_{10} \equiv \left[2\dot{H}\alpha_K + \dot{\alpha}_K H + H^2\alpha_K(3 + \alpha_M)\right] H, \tag{2.53j}$$
$$\lambda_{11} \equiv \left[\alpha_B H + 2H^2(\alpha_M - \alpha_T) + H^2\alpha_B(1 + \alpha_M) - \lambda_3\right]\frac{k^2}{a^2}, \tag{2.53k}$$
$$H^2M^2 \equiv 3\dot{H}[\dot{H}(2 - \alpha_B) + \tilde{\rho}_m + \tilde{p}_m - H\dot{\alpha}_B] - 3H\alpha_B[\ddot{H} + \dot{H}H(3 + \alpha_M)]. \tag{2.53l}$$

To solve the above set of equations (2.48-2.52), we need to give the α_i parameters, together with the standard matter-sector perturbation quantities, δ_m, δp_m, v_m, π_m, and the background expansion history, H – as for the ΛCDM model.

Eliminating the scalar field potential of those equations, and expressing all dynamics in terms of the gravitational potentials, we get

$$\ddot{\Phi} + \frac{\beta_1\beta_2 + \beta_3\alpha_B^2\frac{k^2}{a^2}}{\beta_1 + \alpha_B^2\frac{k^2}{a^2}}\dot{\Phi} + \frac{\beta_1\beta_4 + \beta_1\beta_5\frac{k^2}{a^2} + c_s^2\alpha_B^2\frac{k^4}{a^4}}{\beta_1 + \alpha_B^2\frac{k^2}{a^2}}\Phi = -\frac{1}{2}\tilde{\rho}_m\frac{\beta_1\beta_6 + \beta_7\alpha_B^2\frac{k^2}{a^2}}{\beta_1 + \alpha_B^2\frac{k^2}{a^2}}\delta_m, \tag{2.54}$$

where the β_i functions are defined below. Ψ is obtained from Eq. (2.50) through the equation

$$\begin{aligned}(\alpha_M - \alpha_T)\left[\alpha_B\tilde{\rho}_m\delta_m - 2HE\dot{\Phi}\right] &= \alpha_B^2\frac{k^2}{a^2}\left[\Psi - \Phi\left(1 + \alpha_T + \frac{2(\alpha_M - \alpha_T)}{\alpha_B}\right)\right] + \\ &+ \beta_1\left[\Psi - \Phi(1 + \alpha_T)\left(1 - \frac{2EH^2(\alpha_M - \alpha_T)}{\beta_1}\right)\right]\end{aligned} \tag{2.55}$$

The dynamical system is completed with the standard evolution equations for pressureless matter perturbations

$$\dot{\delta}_m - \frac{k^2}{a^2}v_m = 3\dot{\Phi}, \qquad \dot{v}_m = -\Psi. \tag{2.56}$$

$$\beta_1 \equiv \frac{3\alpha_B^2}{2}(\tilde{\rho}_m + \tilde{p}_m) - E[2\beta_8 + \tilde{\rho}_m + \tilde{p}_m] \tag{2.57a}$$

$$\beta_2 \equiv 2H(2 + \alpha_M) + 3H\beta_9 \tag{2.57b}$$

$$\beta_3 \equiv H(3 + \alpha_M) + \frac{\alpha_K}{E}\left(\frac{\dot{\alpha}_K}{\alpha_K} - 2\frac{\dot{\alpha}_B}{\alpha_B}\right) \tag{2.57c}$$

$$\beta_4 \equiv (1 + \alpha_T)[2\dot{H} + H^2(3 + 3\beta_9 + \alpha_M)] + \dot{\alpha}_T H \tag{2.57d}$$

$$\beta_5 \equiv c_s^2 + \frac{\alpha_B(\beta_3 - \beta_2)}{HE} + \frac{H\alpha_B^2}{\beta_1}(1 + \alpha_T)(\beta_3 - \beta_2) + \frac{\alpha_B^2\beta_4}{\beta_1} \tag{2.57e}$$

$$\beta_6 \equiv \beta_7 + \frac{\alpha_B(\beta_3 - \beta_2)}{HE} \tag{2.57f}$$

$$\beta_7 \equiv c_s^2 - \omega_m + \frac{\alpha_B^2(1 + \alpha_T + 3\omega_m) + 2(\alpha_M - \alpha_T)\alpha_B}{2E} \tag{2.57g}$$

$$\beta_8 \equiv \dot{H} - H^2(\alpha_M - \alpha_T) \tag{2.57h}$$

$$3\beta_1 H\beta_9 \equiv 2E[\dot{\beta}_8 + (3 + \alpha_M)H\beta_8] \tag{2.57i}$$

2.1.6 Ansatzes for the α_i

In order to forecast MG models within Horndeski gravity, we must measure the α_i functions. Their values might be directly inferred given enough data, but usually we do that by assigning specific parameterizations for the α_i – a broad ones have been discussed in [77–80]. Here, we will compute constraints adopting the two parameterizations that follows

◇ **Parameterization I**

$$\alpha_i(z) = \alpha_{i,0}\Omega_{DE}(z). \tag{2.58}$$

This one ensures that the MG model only becomes relevant once DE provides a sizeable fraction of the background energy density.

◇ **Parameterization II**

$$\alpha_i(z) = \alpha_{i,0}a(z). \tag{2.59}$$

This one ensures that the GR modification switches off smoothly at early times.

As initially the scale factor grows more quickly than DE fractional density, the scalar field perturbations become relevant slightly earlier in parameterization II than in parameterization I. In Fig. 6 we show the effects of such parameterization on the CMB angular power spectrum for the model (2.60).

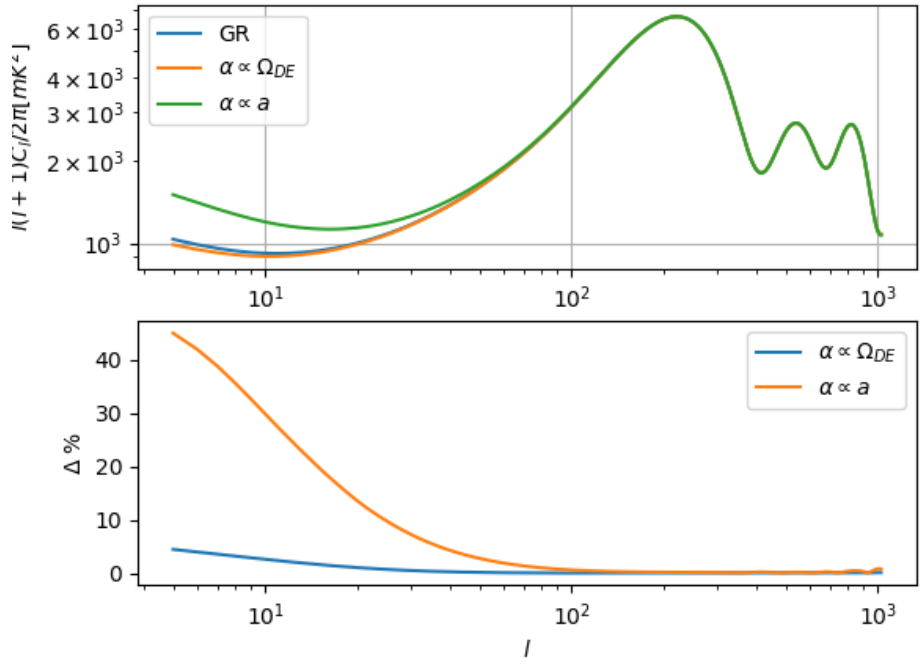

Figure 6 – (a) Upper panel: Effects on the CMB angular power spectrum from the different parameterizations adopted in this work for the α_i functions. Deviations are shown for the MG model given by Eq. (2.60). (b) Lower panel: Relative errors from the ΛCDM model.

2.1.7 HI_CLASS code

The phenomenological parameterization for the α_i functions was implemented in Boltzmann codes, such as CAMB [81] and CLASS [82] – we use HI_CLASS to compute the perturbed equations [83]. Fig. 7 presents schematically how HI_CLASS works: The user sets in the input module a parameterization, the initial values for the α_i parameters, as well as others fiducial cosmological values to determine Ω_{DE}. Then, the background is computed, giving the Hubble rate and the α_i functions. Next, the thermodynamics module computes the thermal evolution using this background expansion history. Finally, the code uses these last results as inputs to determine the evolution of perturbations, giving the observables.

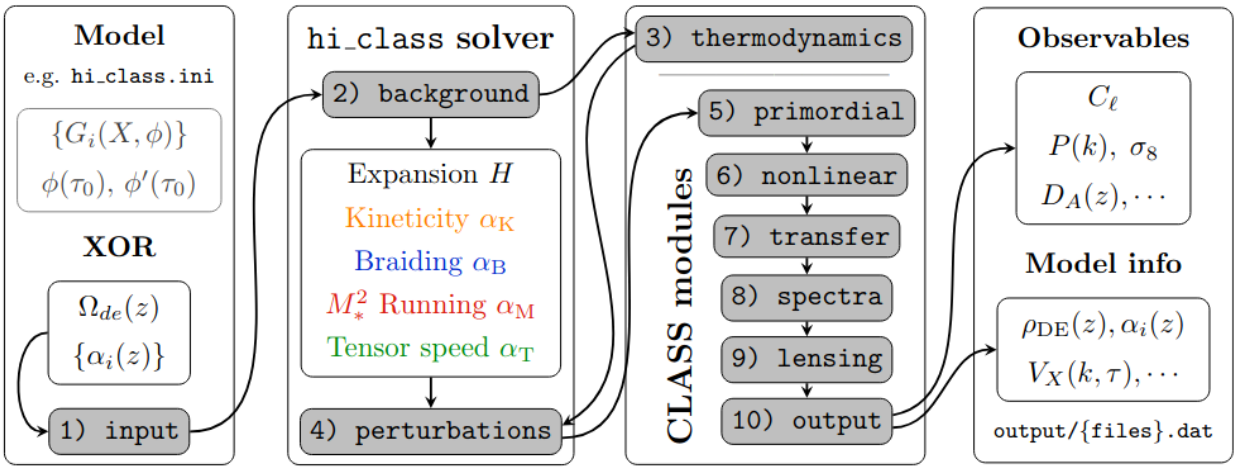

Figure 7 – Description of HI_CLASS structure. The arrows represent the flow of information between modules, while the numbers represent the order of execution of the module. Extracted from [83].

The CMB angular power spectrum (see Eq. 3.30) for some sort of models within the sub-class of Horndeski theories (2.39) is shown in Fig. 8. In these plots we used the parameterization $\alpha_i \propto \Omega_{DE}$.

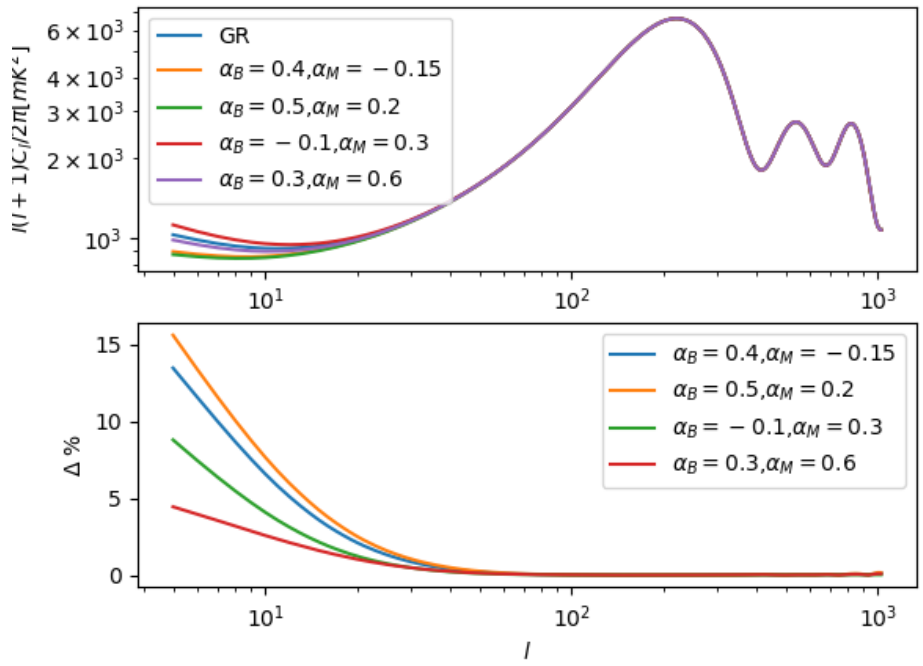

Figure 8 – (a) Upper panel: Effects of vary the α_i functions on the CMB angular power spectrum; (b) Lower panel: Relative errors of the MG models from the ΛCDM one. Here, we set $\alpha_K = 0.1$ and $\alpha_T = 0$, and consider the parameterization $\alpha_i \propto \Omega_{DE}$.

As we can see, the model defined by the set of values

$$\alpha_T = 0, \qquad \alpha_K = 0.1, \qquad \alpha_M = 0.6, \qquad \alpha_B = 0.3, \tag{2.60}$$

is the closest to ΛCDM, giving the smallest relative error. For this reason, we will take such a model in our analysis, placing constraints in some cosmological parameters in Chapt. 5.

2.1.8 μ and Σ couplings

To interpret theoretical predictions coming from solutions for the gravitational potentials, we define two phenomenological parameters: the *effective gravitational coupling*, μ − associated with modifications of gravity on the clustering of matter −, and the *light deflection parameter*, Σ − which accounts for modifications on how light travels. These ones are given by

$$-\frac{k^2}{a^2}\Psi = 4\pi G\mu\bar{\rho}_m\delta_m, \tag{2.61a}$$

$$-\frac{k^2}{a^2}(\Psi+\Phi) = 8\pi G\Sigma\bar{\rho}_m\delta_m. \tag{2.61b}$$

Also, we can combine these equations, and derive a third descriptor of MG observational effects, the *gravitational slip parameter*, defined as

$$\eta = \frac{2\Psi}{\Psi+\Phi}. \tag{2.62}$$

The relation between these three functions reads

$$\Sigma = \frac{\mu}{2}(1+\eta), \tag{2.63}$$

where the GR is recovered when $\Sigma = \mu = \eta = 1$. Thus, the introduction of deviations on the coefficients of perturbed evolution equations by the α_i functions, modifies the standard Poisson equation (2.61*a*), altering the dynamics for the growth of structures as

$$\ddot{\delta}_m + 2H\dot{\delta}_m - 4\pi G a^2\mu\bar{\rho}_m\delta_m = 0. \tag{2.64}$$

The solution for this equation is the *linear growth function*, D, given by

$$\delta_m(a) = D(a)\delta_m(a=1), \tag{2.65}$$

from which we obtain the *linear growth rate*, f, commonly used for observational comparison purposes

$$f \equiv \frac{dlnD(a)}{dlna}. \tag{2.66}$$

In Fig. 9, we plot the slip parameter for the model (2.60). We clearly see the deviation caused by the model from the GR for the redshift range $0.04 < z < 3.0$.

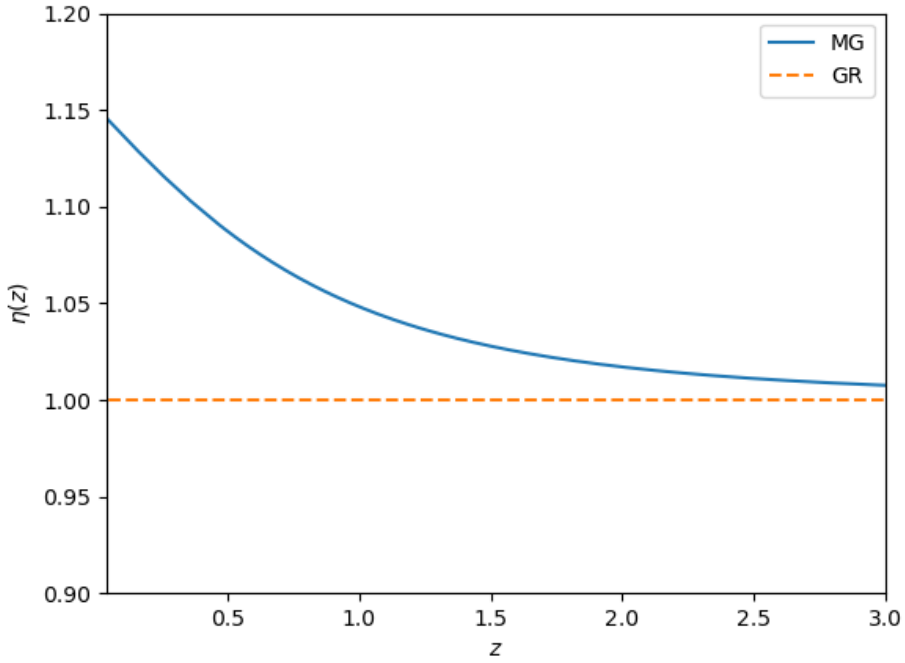

Figure 9 – Slip parameter derived from the MG model given by Eq. (2.60), compared with that one of the GR theory for the redshift range $0.04 < z < 3.0$.

2.1.9 Quasi-Static Limit & Non-linear Effects

Obtain analytical forms of the couplings presented above is generally not possible. However, those are achieve for a specific theory of gravity if we consider the *quasi-static* (QS) limit (or approximation). Such a limit is obtained by setting the terms containing time derivatives in Eq. (2.54) to zero. As result, we get an expression relating Φ to the matter density perturbation, which can be rewritten in the form of Eq. (2.61*a*). From [10], such couplings in QS approximation read

$$\mu^{QS}(z) = \frac{\alpha_T}{2} + \frac{2\alpha^2}{Ec_s^2}, \tag{2.67a}$$

$$\Sigma^{QS}(z) = \frac{\alpha_T}{2} + \frac{\alpha(\alpha - \alpha_B/2)}{Ec_s^2}, \tag{2.67b}$$

$$\eta^{QS}(z) = \frac{Ec_s^2 - \alpha_B\alpha}{Ec_s^2(1+\alpha_T) + 2\alpha^2}, \tag{2.67c}$$

where

$$\alpha \equiv -\frac{\alpha_B}{2}(1+\alpha_T) + \alpha_T - \alpha_M. \tag{2.68}$$

Instead of constrain the α_i functions, it is also possible investigate DE/MG extensions to GR using the μ, Σ, η approach. Deviations from the standard model can then be captured by constraining such functions in a model-independent manner, as was it done in Sec. 4.5 of [61].

We end up the discussion about Horndeski gravity by saying that to connect the linear approach presented here with non-linear effects is not clear in the general case. Only if we consider well-defined sub-classes of Horndeski theories is that it becomes manageable. Such non-linear effects, also known as screening mechanisms, correspond to regions of high density, and are strongly suppressed by Solar System and binary pulsar constraints. Some known screening mechanisms are Chameleon screening [84], K-mouflage [85] and Vainshtein screening [86, 87], most of them excluded observationally.

3 Observables

We have an MG model that is proposed to describe the late-time expansion of the universe, and now we need the observational data to constrain its parameters. Several cosmological observables can be used to test MG theories. They can be SNIa and BAO surveys − which constrains the Hubble rate or the DE equation of state −; RSD, CMB, and WL surveys − which measure gravitational potentials, matter density, and temperature fluctuations power spectra. A special observable is the 21-cm line of HI, from which we can build temperature maps, and extract, among others relevant information to astrophysics and cosmology, the BAO signal. In this chapter, we introduce the observables used in this work: CMB and the 21-cm line of HI − Sec. 3.1 and Subsec. 3.2.2, respectively.

3.1 Cosmic Microwave Background

The CMB temperature was first theoretically predicted by R. Alpher and R. Herman in 1948 [88], following the arguments developed by G. Gamow [89]. This prediction was years later confirmed by A. Penzias and R. Wilson in 1965 [90] while trying to identify sources of noise in microwave satellite communications at Bell Laboratories, in New Jersey. The detected noise was interpreted by R. Dicke *et al.* as being the CMB at a temperature of 3.5 ± 1 K [91].

The CMB spectrum is well described by the blackbody model, with $T_\gamma = 2.7255$ K [27], and today CMB is the main supporting pillar of the Big Bang model for the universe. In fact, anisotropies in the CMB temperature, first reported by COBE satellite in 1992 [92], provide strong support that the initial fluctuations from gravitational instability generated all of the structure in the universe, and the matter-energy constituents drive its expansion [93].

3.1.1 Recombination

In this subsection, we derive formally some universe's stages associated with the CMB we observe today. To do that, we start considering that the elements of interest are in thermal equilibrium − described by the so-called Saha equation −, and later we consider them in a more complicated situation (out-of-equilibrium), which requires a treatment via Boltzmann equation. The physics of recombination was first presented by P. Peebles, in 1968 [94].

In early times, the universe was constituted by a hot and dense plasma of baryons, electrons, photons, etc. The multiple interactions in this plasma were so abundant that the mean free path of a photon was about the size of an atom. As the universe expands, the baryonic matter

goes from an ionized plasma to a neutral gas, forming HI from electrons and protons in an epoch known as *recombination*.

As the rate at which photons scatter from electrons becomes smaller than the Hubble parameter, the mean free path of the photon grows, allowing it to stream freely, at the time known as *photon decoupling*, originating the observed CMB, detected today from the *last scattering surface*.

The epoch of recombination is determined by the Saha equation. In order to derive it, let us assume that the universe is only fulfilled with a single element, the hydrogen (H), and that it is in thermal equilibrium with photons (γ), electrons (e^-), and protons (e^+), described by the reaction that follows

$$e^- + p^+ \leftrightarrow H + \gamma. \tag{3.1}$$

Using Eq. (1.76) for the number density, each element is specified by

$$n_i = g_i \left(\frac{m_i T}{2\pi}\right)^{3/2} exp\left(\frac{\mu_i - m_i}{T}\right). \tag{3.2}$$

Also, let us consider that these elements are in chemical equilibrium, *i.e.*, $\mu_e + \mu_p = \mu_H$ ($\mu_\gamma = 0$). The dependency of the chemical potential is removed by writing the ratio that follows

$$\left(\frac{n_e n_p}{n_H}\right)_{eq} = \frac{g_e g_p}{g_H}\left(\frac{m_e m_p}{m_H}\frac{T}{2\pi}\right)^{3/2} e^{-(m_p+m_e-m_H)/T}. \tag{3.3}$$

In the exponential, the sum of masses gives the biding energy of the hydrogen into ground state

$$B_H \equiv m_p + m_e - m_H = 13.6\ eV. \tag{3.4}$$

The values for the internal degrees of freedom are: $g_p = g_e = 2$ and $g_H = 4$[1]. Then, since the universe is electrically neutral, $n_p = n_e$, we obtain

$$\left(\frac{n_e^2}{n_H}\right)_{eq} = \left(\frac{m_e T}{2\pi}\right)^{3/2} e^{-B_H/T}. \tag{3.5}$$

where we set $m_p \approx m_H$ in the prefactor. In order to accounts for the degree to which the baryonic content of the universe is ionized let us define the *free electron fraction*

$$X_e \equiv \frac{n_e}{n_e + n_H} = \frac{n_e}{n_b}, \tag{3.6}$$

[1] In the hydrogen atom, the spins of electron and proton can be aligned or anti-aligned giving one singlet and one triplet states, which leads to $g_H = 1 + 3 = 4$.

where we are neglecting the relatively small number of helium atoms − it will be clear in a moment why we made this definition. In the last equality n_b is the density number of baryons

$$n_b = \eta n_\gamma = \eta \frac{2\zeta(3)}{\pi^2} T^3, \tag{3.7}$$

which depends on the *baryon-to-photon ratio*, $\eta = 5.5 \times 10^{-10}\,(\Omega_b h^2/0.020)$. Thus, using these last equations we can rewrite the Eq. (3.5)

$$\left(\frac{X_e^2}{1-X_e}\right)_{eq} = \frac{\pi^2}{2\eta\zeta(3)} \left(\frac{m_e}{2\pi T}\right)^{3/2} e^{-B_H/T}. \tag{3.8}$$

which is known as *Saha equation*. When $T \sim B_H$ the right-hand side of the last equation is of order $\sim 10^{15}$. To be satisfied, the denominator on the left-hand side must be very small, which yields $X_e \sim 1$ meaning that all electrons are free, or, in other words, all hydrogen is ionized. The recombination time takes place when $X_e = 10^{-1}$ in the last equation, which gives to us $T_\star \approx 3.600$ K. Since $T \propto a^{-1}$ (Eq. 1.90), the redshift of recombination is $z_\star \approx 1320$.

The Saha equation is an approximation to case where hydrogen, electrons, and photons are in thermodynamic equilibrium. However, as the temperature drops far below the biding energy, the exponential of Eq. (3.8) changes, and we must solve the Boltzmann equation (1.99) to follow the electrons relics. The equilibrium abundance of HI is given by $n_H \approx n_H^{eq}$, and then, the Boltzmann equation for the electron density can be written as

$$\frac{1}{a^3}\frac{d(n_e a^3)}{dt} = -\langle\sigma v\rangle \left[n_e^2 - (n_e^{eq})^2\right]. \tag{3.9}$$

The cross-section is approximated by

$$\langle\sigma v\rangle \cong \sigma_T \left(\frac{B_H}{T}\right)^{1/2}, \tag{3.10}$$

where $\sigma_T \approx 2 \times 10^{-3}$ MeV^{-2} is the Thomson cross-section. Writing $n_e = n_b X_e$ and given that $n_b a^3 = const.$, we get

$$\frac{dX_e}{dx} = -\frac{\lambda}{x^2}\left[X_e^2 - (X_e^{eq})^2\right], \tag{3.11}$$

where $x = B_H/T$, and we have defined λ for a *matter dominated universe* as

$$\lambda \equiv \left[\frac{n_b\langle\sigma v\rangle}{xH}\right]_{x=1} = 3.9 \times 10^3 \left(\frac{\Omega_b h}{0.03}\right). \tag{3.12}$$

The numerical solutions of both Saha (3.8) and Boltzmann (3.11) equations are shown in Fig. 10.

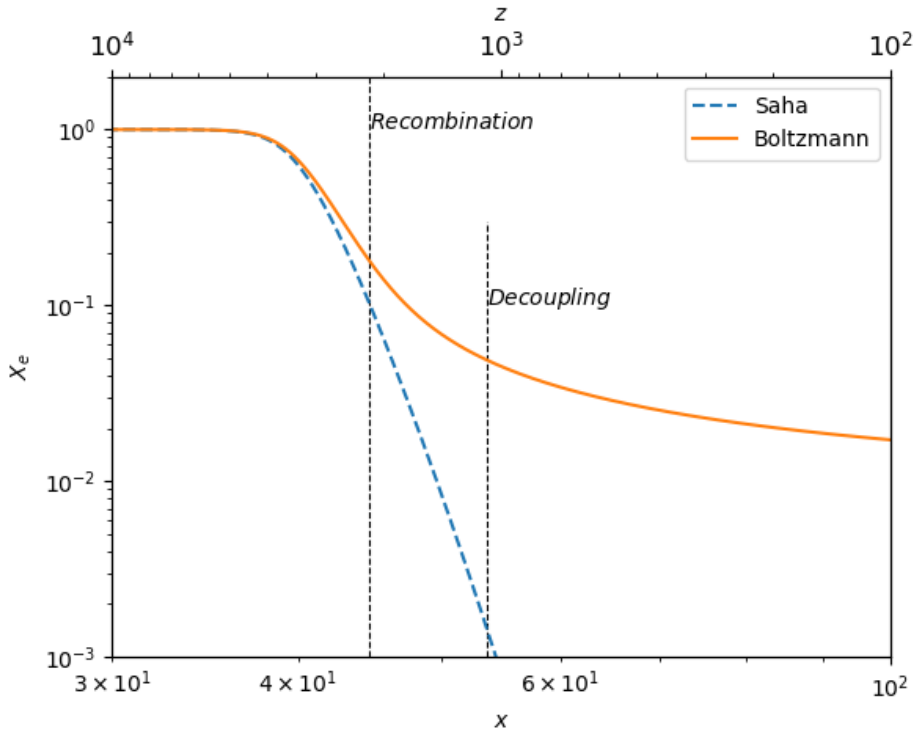

Figure 10 – Numerical solutions of the Saha and Boltzmann equations as a function of the redshift, z, and x.

Following the expansion of the universe, photons decouple from matter when their interaction rate with electrons, described by the Thomson scattering [95],

$$\Gamma_\gamma(z) = n_e(z)\sigma_T c, \tag{3.13}$$

becomes smaller than the expansion rate, *i.e.*, $\Gamma(T_{dec}) \sim H(T_{dec})$. Again, writing $n_e = n_b X_e$, and taking the Hubble parameter for a matter-dominated universe

$$H(T_{dec}) = H_0\sqrt{\Omega_{m,0}}\left(\frac{T_{dec}}{T_\gamma}\right)^{3/2}, \tag{3.14}$$

we get

$$X_e(T_{dec})T_{dec}^{3/2} \sim \frac{\pi^2}{2\zeta(3)}\frac{H_0\sqrt{\Omega_{m,0}}}{\eta\sigma_T T_\gamma^{3/2}}. \tag{3.15}$$

The photon decoupling occurs when $X_e = 10^{-2}$ in the last equation, which gives $T_{dec} \sim 0.27$ eV, or the redshift of decoupling $z_{dec} \sim 1100$ for the best-fit of cosmological parameters. Once decoupled, the CMB photons start their travel to us from the *last-scattering surface*.

3.1.2 Thomson Scattering in the IGM

At relatively low redshift, the CMB photons are affected by some effects, such as Thomson scattering, gravitational lensing [96], Integrated Sachs-Wolfe (ISW) effect (Sec. 3.1.4.3), and Sunyaev-Zeldovich effect [97]. The Thomson scattering in the *intergalactic medium* (IGM) comes from the *reionization epoch*, an epoch where pos-recombination neutral baryons are reionized by photons produced by the first stars. This process is described by the *optical depth*, defined as the integral of the Thomson scattering (Eq. 3.13) at some redshift z_i

$$\tau \equiv \int_0^{z_i} \Gamma_\gamma(z) \frac{dt}{dz} dz = n_{H,0} \sigma_T c \int_0^{z_i} X_e(z) \frac{(1+z)^2}{H(z)} dz. \tag{3.16}$$

The inferred value of τ depends on the model assumed for the free electron fraction, and on the background cosmology. The best-fit value for the optical depth, using a hyperbolic tangent model for $X_e(z)$, is $\tau = 0.054 \pm 0.007$[2]. Essentially, the optical depth reduces the observed fluctuation amplitude (Eq. 3.30) on all scales by a factor $e^{-\tau}$ (see Eq. 3.48).

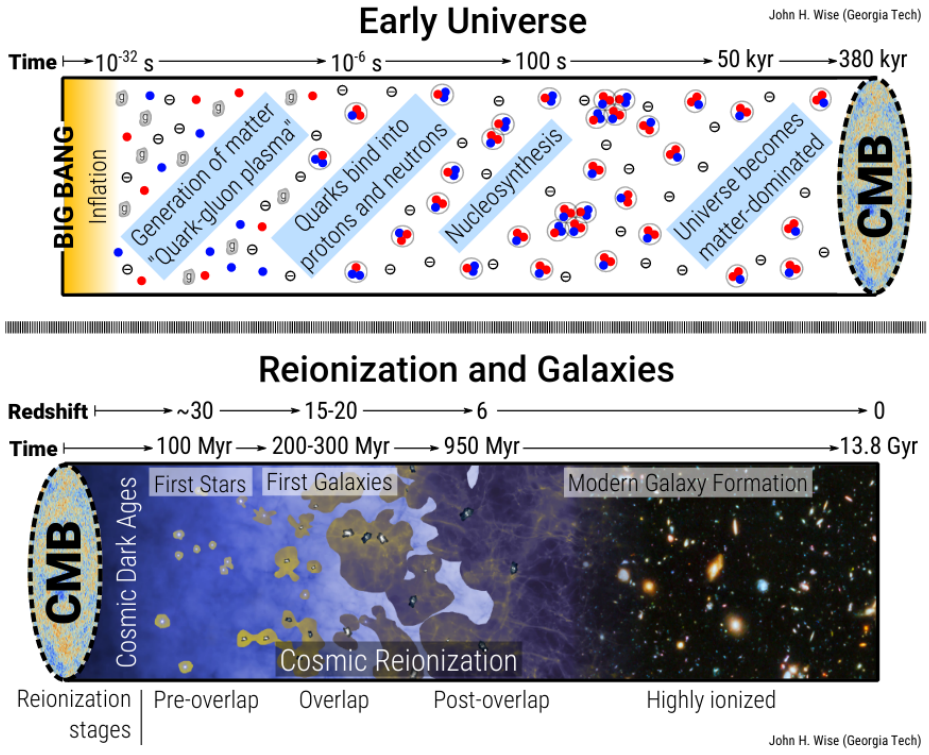

Figure 11 – Illustration of the universe before (top) and after (bottom) recombination along with the stages of reionization. Extracted from [99].

[2] This model assumes a smooth transition from a neutral to the ionized universe; it is not physically motivated, but satisfies the requirement of the optical depth be approximately independent of the transition width, a parameter coming from a fitting function for $X_e(z)$ applied by A. Lewis in this work [98].

3.1.3 Statistical Description of the CMB Fluctuations

The CMB signal from different locations in the sky is recorded by measuring the radiation intensity at a given frequency, I_ν. This is related to the blackbody temperature in the low regime (Raleigh-Jeans portion of the Planck function)

$$I_\nu = \frac{2h\nu^3}{c^2}\frac{1}{e^{h\nu/k_BT}-1}, \tag{3.17}$$

or

$$I_\nu \propto \nu^2 T, \qquad when \qquad h\nu \ll k_BT, \tag{3.18}$$

which implies, for a fixed frequency,

$$\frac{\delta I_\nu}{I_\nu} = \frac{\delta T}{T}. \tag{3.19}$$

This relation allows us to investigate fluctuations in temperature through the measurement of the radiation intensity. Actually, the key CMB observable is the angular variation in temperature correlations, defined from the mean temperature, T_γ, as the dimensionless fluctuations

$$\Theta(\theta,\phi) \equiv \frac{\delta T}{T_\gamma}(\theta,\phi) = \frac{T(\theta,\phi)-T_\gamma}{T_\gamma}, \tag{3.20}$$

with $T(\theta,\phi)$ denoting the temperature at a given point on the sky (θ,ϕ). The mean temperature average over the whole sky is

$$T_\gamma = \frac{1}{4\pi}\int T(\theta,\phi)\sin\theta d\theta d\phi = 2.7255 \pm 0.0006K, \tag{3.21}$$

from which we obtain temperature anisotropies at the $\langle\Theta^2\rangle^{1/2} \sim 10^{-5}$ level.

The CMB temperature fluctuations are well characterized by connecting them to statistic through the angular power spectrum formalism − we introduced it here for CMB density field, but it is also applied to others fields (*e.g.* galaxy and HI ones). Such a formalism consists in decompose the density field in terms of orthonormal spherical harmonics as

$$\Theta(\theta,\phi) = \sum_{l=0}^{\infty}\sum_{m=-l}^{l} a_l^m Y_l^m(\theta,\phi). \tag{3.22}$$

The angular spectrum is built taking the coefficients of this expansion. Given that spherical harmonics are normalized according to

$$\int_0^{2\pi} d\phi \int_0^{\pi} \sin\theta d\theta Y_{lm}^*(\theta,\phi) Y_{l'm'}(\theta,\phi) = \delta_{ll'}\delta_{mm'}, \tag{3.23}$$

we get the useful addition property

$$\sum_{m=-l}^{l} Y_{lm}(\theta,\phi)Y^*_{lm}(\theta',\phi') = \frac{2l+1}{4\pi}\mathcal{P}_l(\cos\alpha), \tag{3.24}$$

where α is the angle between the two directions $\vec{r}(\theta,\phi)$ and $\vec{r}'(\theta',\phi')$, and $\mathcal{P}_l$ is the Legendre polynomial of order l.

A statistical measurement of the temperature fluctuations is given by the *correlation function*. Denoted by $C(\alpha)$, it is found by multiplying together the values of Θ at the two points, and averaging the product over all pairs of points separated by the angle α

$$C(\alpha) = \langle \Theta(\vec{r})\Theta(\vec{r}') \rangle_{\vec{r}\cdot\vec{r}'=\cos\alpha}\,. \tag{3.25}$$

Using the expansion in spherical harmonics (3.22) and the addition property (3.24), the correlation function can be written in the form

$$C(\alpha) = \frac{1}{4\pi}\sum_{l=0}^{\infty}(2l+1)C_l\mathcal{P}_l(\cos\alpha), \tag{3.26}$$

from which we obtain the angular power spectrum as its *multipole components* − using the normalization condition (3.23) to invert the Eq. (3.22) −,

$$\langle a^*_{ml}a_{m'l'}\rangle = \delta_{ml}\delta_{m'l'}C_l, \tag{3.27}$$

with

$$a_{ml} = \int_{\theta=-\pi}^{\pi}\int_{\phi=0}^{2\pi}\Theta(\theta,\phi)Y_l^{*m}(\theta,\phi)d\Omega. \tag{3.28}$$

In Eq. (3.27), immediately we see that if $m \neq m'$, $l \neq l'$ we get a null angular power spectrum. For $l = l'$, we find in literature the denominations that follows: if $m \neq m'$ we refer to the angular power spectrum as *cross correlations* of C_l's; otherwise, if $m = m'$, we get the *auto correlations* of C_l's − given a l, equal/different m correspond to equal/different patterns or orientations with the same angular scale, $\theta \sim 180°/l$.

Using the previous results, as for auto correlations of C_l's the expectation values of the multipole coefficients amplitudes depend on l only, *i.e.* $C_l = \langle|a_l^m|^2\rangle$, we can measure the C_l's of CMB from the expectation value of the square of the temperature perturbation through the sum

$$\left\langle\left(\frac{\delta T}{T}\right)^2\right\rangle = \sum_l \frac{2l+1}{4\pi}C_l. \tag{3.29}$$

We also have a theoretical model for the angular power spectrum. It comes from the inflationary theory, which predicts a functional form for the three-dimensional power spectrum

of primordial curvature perturbations (Eq. 3.32). As for the case of the multipole coefficients, the amplitude of the primordial power spectrum does not differentiate between directions; instead, it depends just on the scale magnitude, k, in Fourier space. The angular power spectrum is related to the primordial one via [100]

$$C_l^{TT} = \frac{2}{\pi}\int dk k^2 \left|\Theta_l(k)\right|^2 P_{\mathcal{R}}(k) = 4\pi \int \frac{dk}{k} \left|\Theta_l(k)\right|^2 \Delta^2_{\mathcal{R}}(k), \tag{3.30}$$

where $\Theta_l(k)$ is the *multipole moment* of the temperature fluctuations in Fourier space, defined as

$$\Theta_l(k) = \frac{1}{2(-i)^l}\int_{-1}^{1} d\mu \mathcal{P}_l(\mu)\Theta(\mu), \tag{3.31}$$

with $\Theta(\mu)$ being the Fourier transform of Eq. (3.20), $\mu = \hat{k}\cdot\hat{p}$, and $\hat{p}$ is the photon direction.

In the definition (3.30), $P_{\mathcal{R}}(k)$ denotes the *primordial power spectrum*, a measure of the distribution of very tiny perturbations, which act as the seeds of structure formation in the context of inflationary theory – $\Delta^2_{\mathcal{R}}(k) = k^3 P_{\mathcal{R}}(k)/2\pi^2$ is the dimensionless power spectrum, useful for some applications. We do not treat the theory of inflation here, but V. Mukhanov gives a very clear description of how quantum mechanical processes generate such perturbations in Chap. 8 of his book [101].

The simplest model predicted by inflation contains two parameters describing the initial conditions for density perturbations: A_s and n_s, respectively the amplitude and slope of the functional form for the power spectrum

$$P_{\mathcal{R}}(k) = A_s^2 \left(\frac{k}{k_0}\right)^{n_s-1}, \qquad with \qquad n_s = 1 - 6\epsilon + 2\eta. \tag{3.32}$$

Here, $A_s^2 \equiv P_{\mathcal{R}}(k_0)$, with k_0 usually chosen as $k_0 = 0.05 Mpc^{-1}$; ϵ and η are the slow-roll parameters depend on the inflation model, $V(\phi)$,

$$\epsilon \equiv \frac{3}{2}\frac{\dot{\phi}^2}{V}, \qquad and \qquad \eta \equiv \epsilon - \frac{\ddot{\phi}}{H\dot{\phi}}. \tag{3.33}$$

The current best-fit values for A_s and n_s are: $n_s = 0.965 \pm 0.004$ and $A_s = (2.101^{+0.031}_{-0.034}) \times 10^{-9}$. Both observed and theoretical C_l's are shown in Fig. 12, from which we see the good agreement between theory and observations. The plot was made as

$$\mathcal{D}_l^{TT} = \frac{l(l+1)}{2\pi} C_l^{TT} T_\gamma^2, \tag{3.34}$$

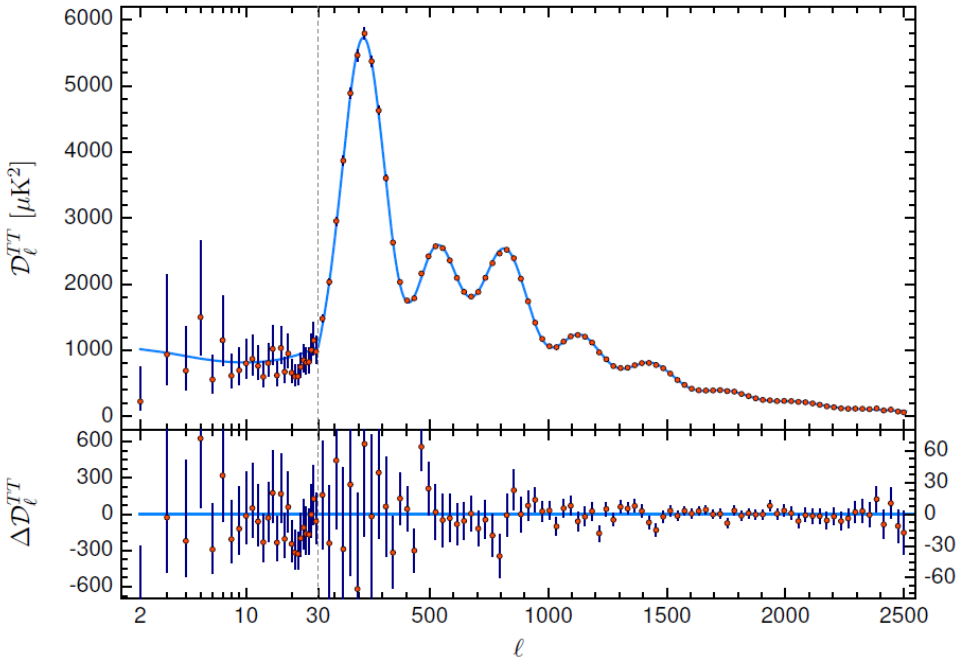

Figure 12 – (a) Upper panel: The base-ΛCDM theoretical spectrum best-fit to the *Planck* TT,TE,EE+lowE+lensing likelihoods is plotted in light blue. (b) Lower panel: Residuals with respect to this model. Extracted from [23].

3.1.4 Physics of CMB Anisotropies

In this subsection, we describe the physics behind the multipole moment components that enter into the model for the CMB angular power spectrum. We do not present a full treatment starting from the first principle of perturbation theory, but we are assuming a small perturbation on the FLRW metric, written in terms of the gravitational potentials, Φ and Ψ, as given by Eq. (2.45).

3.1.4.1 The Monopole, $l = 0$

The monopole term of the correlation function $C(\alpha)$ corresponds to $l = 0$ in the Eq. (3.25), and is associated to the mean temperature, averaged over the whole sky, T_γ. This term vanishes, since $Y_0^0 = 1/2\sqrt{\pi}$, which makes $a_0^0 = \langle\Theta(\theta,\phi)\rangle = 0$, from the definition (3.20). Actually, we do not know if the mean temperature we measure locally is different from the average temperature of the universe.

3.1.4.2 The Dipole, $l = 1$

The dipole term of the correlation function $C(\alpha)$ corresponds to $l = 1$ in the Eq. (3.25), and is affected by our motion across space − our view of the CMB is redshifted (or blueshifted),

depending on the angle θ relative to the nearly isotropic blackbody field.

For the motion of an observer with velocity $\beta = v/c$, the corresponding temperature shifts as a Lorentz-boost, producing a pattern given by [102]

$$T(\theta) = T_\gamma \frac{(1-\beta^2)^{1/2}}{1-\beta\cos\theta} \cong T_\gamma \left[1 + \beta\cos\theta + \mathcal{O}(\beta^2)\right]. \tag{3.35}$$

The CMB dipole is a demonstration that we are not fundamental observers. This dipole is a frame-dependent quantity, and the rest frame is that in which the CMB dipole would be zero.

3.1.4.3 The ISW, $l \leq 10$, and Sachs-Wolfe Plateau, $10 \leq l \leq 100$

For small values of l (large scales), the main source of temperature fluctuations are the intrinsic inhomogeneities in the distribution of matter (mostly DM), which is described by the variation of the energy density

$$u_{DM}(\vec{r}) = \langle u_{DM}\rangle + \delta u_{DM}(\vec{r}), \tag{3.36}$$

where $\delta u_{DM}(\vec{r})$ is the local deviation from the mean $\langle u_{DM}\rangle$. This deviation generates a fluctuating gravitational potential $\delta\Phi$, both related via Poisson equation

$$\nabla^2(\delta\Phi) = 4\pi G \delta u_{DM}. \tag{3.37}$$

A detailed general relativistic calculation, performed by Sachs and Wolfe [103] shows that the perturbation of the potential gravitation can affect the temperature fluctuations in two different ways. First, through the gravitational redshift, which accounts the lose of photons energy when they climb out the potential well. Considering the weak-field regime, it is given by

$$\Theta = \frac{\delta\nu}{\nu} \approx \delta\Phi. \tag{3.38}$$

The second way comes from photons scattered from higher density regions. These photons received today were scattered at slightly earlier times, when the CMB temperature was slightly higher, causing a time dilatation at time scattering $\delta t/t = \delta\Phi$. As in the early time the universe is dominated by matter, *i.e.* $a \propto t^{2/3}$, and given that $T \propto a^{-1}$, we then obtain

$$\Theta \approx -\frac{2}{3}\delta\Phi. \tag{3.39}$$

The added two effects (3.38, 3.39) gives the commonly known Sachs-Wolf (SW) effect

$$\Theta = \frac{1}{3}\delta\Phi. \tag{3.40}$$

In terms of multipole moment, the SW effect is written as [100]

$$\Theta_l(\tau_0, k) = \Theta_I + \Theta_{II} + \Theta_{III}, \tag{3.41}$$

where

$$\Theta_I = (\Theta_0 + \Psi)(\tau_\star, k) j_l(kr_\star) \tag{3.42a}$$

$$\Theta_{II} = 3\Theta_1(\tau_\star, k)\left[j_{l-1}(kr_\star) - \frac{l+1}{kr_\star} j_l(kr_\star)\right] \tag{3.42b}$$

$$\Theta_{III} = \int_{\tau_\star}^{\tau_0} d\tau \left[\Psi'(\tau, k) + \Theta'(\tau, k)\right] j_l(kr), \tag{3.42c}$$

are respectively the monopole, dipole, and ISW terms, for $l \geq 1 -$ here, j_l are the Bessel spherical functions, τ is the conformal time, with subscripts 0 and $\star$ indicating the present and recombination time, respectively; $r = \tau_0 - \tau$. Inserting the Eq. (3.41) into Eq. (3.30), we can predict the contribution to the total angular power spectrum of CMB.

These fluctuations happen at all scales, but dominate at large scales. As the primordial power spectrum $P_{\mathcal{R}}(k) \propto k^{n_s - 1}$, the angular power-spectrum C_l reduces to $l(l+1)C_l/2\pi \propto l^{n_s - 1}$. In principle one can measure n_s this way. For scale invariance ($n_s = 1$), $C_l \propto 1/l(l+1)$, which gives rise to the flat part of Fig. 12, know as *Sachs-Wolf plateau*.

3.1.4.4 The Acoustic Peaks, $100 \leq l \leq 1000$

Continuing to build up a picture of how the universe was like at the last scattering surface, the Fig. 12 shows a peak at an angular scale $\theta \approx 1°$, which corresponds to the *sound horizon* (Eq. 3.46) at the time of decoupling. Let us consider what happened before the atoms in the universe became neutral.

At the epoch of recombination, the universe was fully ionized and consisted of a plasma mixture that, among others, contained photons and baryons. The baryons were coupled to the electrons by Coulomb scattering which in turn were tightly coupled to the photons via Thomson scattering. This coupling allows us to treat the primordial plasma as a perfect baryon-photon relativistic fluid.

The fluid was inside gravitational potential wells, provided mostly by DM. As gravity tries to compress the fluid, photon pressure resists, reversing the compression. With some additional inertia, the baryons expand until gravity takes over again. The fluid density underwent oscillations, giving time variations in temperature, creating what we call as BAO.

We expect to see these oscillations in the baryon distribution, after recombination, and actually it was detected by Eisenstein *et al.* [4], as detailed in Sec. 3.2.1. The oscillations affect the CMB temperature as described by equation

$$\left(\frac{d^2}{d\tau^2} + \frac{R'}{1+R}\frac{d}{d\tau} + k^2 c_s^2\right)(\Theta_0 + \Phi) = \frac{k^2}{3}\left(\frac{\Phi}{1+R} - \Psi\right), \tag{3.43}$$

where $c_s^2 = 1/3(1+R)$ is the *sound speed* squared, with $R = 3\rho_b/4\rho_\gamma$.

The solution of the last equation, after some algebraic steps, reads

$$\begin{aligned}(\Theta_0 + \Psi)(\tau, k) &= (\Theta_0 + \Psi)(0, k)\frac{\cos[kr_s(\tau)]}{(1+R)^{1/4}} \\ &+ \frac{k}{\sqrt{3}}\int_0^\tau d\tau' \left[\frac{\Phi(\tau')}{1+R} - \Psi(\tau')\right]\sqrt{1+R}\sin[kr_s(\tau) - kr_s(\tau')], \quad (3.44)\end{aligned}$$

with extrema fluctuations given by

$$\frac{k\tau}{\sqrt{3(1+R)}} = n\pi, \qquad n = 1, 2, 3, ... \quad (3.45)$$

In Eq. (3.44), r_s is the sound horizon, defined as

$$r_s \equiv \int_0^\tau c_s(\tau')d\tau', \quad (3.46)$$

i.e., the sound horizon is the conformal distance traveled by a sound wave propagating in the photon-baryon fluid. When evaluated at recombination, it gives the *standard ruler*, with size $r_s(\tau_\star) = 150$ Mpc.

The dipole contribution to the temperature fluctuations is $\Theta_1(\tau, k) = -\Theta_0'(\tau, k)/k$. Inserting this one, and the monopole (3.44) into the Eq. (3.41), and in turn substituting the result in Eq. (3.30), we get the the angular power spectrum.

3.1.4.5 The Damping Tail, $l \geq 1000$

In Fig. 12, for $l \geq 1000$, the temperature fluctuations drops off. This comes from the fact that the recombination process is not instantaneous. The coupling between baryons and photons is not perfect: as the mean free path of photons grows, they can diffuse and smooth out temperature anisotropies. This leads to a damping of the anisotropies, cutting off them at multipole above about 2000.

So, we need to consider what happens to the temperature fluctuations when the quadrupole moment, Θ_2, is taken into account. The relation between the dipole and the quadrupole moment is $\Theta_2 = -4k\Theta_1/9\tau'$, from which we can obtain Θ_0 and write the dynamic equation [104]

$$\Theta_0'' + \left(-\frac{8k^2}{27\tau'}\right)\Theta_0' + \frac{k^2}{3}\Theta_0 = 0. \quad (3.47)$$

This is the equation for an harmonic oscillator, where a damping term relevant on small scale appears Here, τ is the *optical depth* to Thomson scattering Eq. (3.16). The Eq. (3.47) has as a solution

$$\Theta_0 \propto e^{ik\tau/\sqrt{3}}e^{-k^2/k_{silk}^2}, \quad (3.48)$$

where we have introduced the *Silk length*

$$\lambda_{silk}^2 = \frac{1}{k_{silk}^2} \equiv -\frac{4\tau}{27\tau'}. \tag{3.49}$$

The Silk length is the comoving distance traveled by a photon in a time τ, taking into account the collisions which it is suffering, *i.e.* its diffusion. Again, inserting the Eq. (3.48) into Eq. (3.41), we get the CMB power spectrum in this regime. Fig. 13 shows the C_l's of CMB and each contribution for the plot of anisotropies, computed using CLASS code [82].

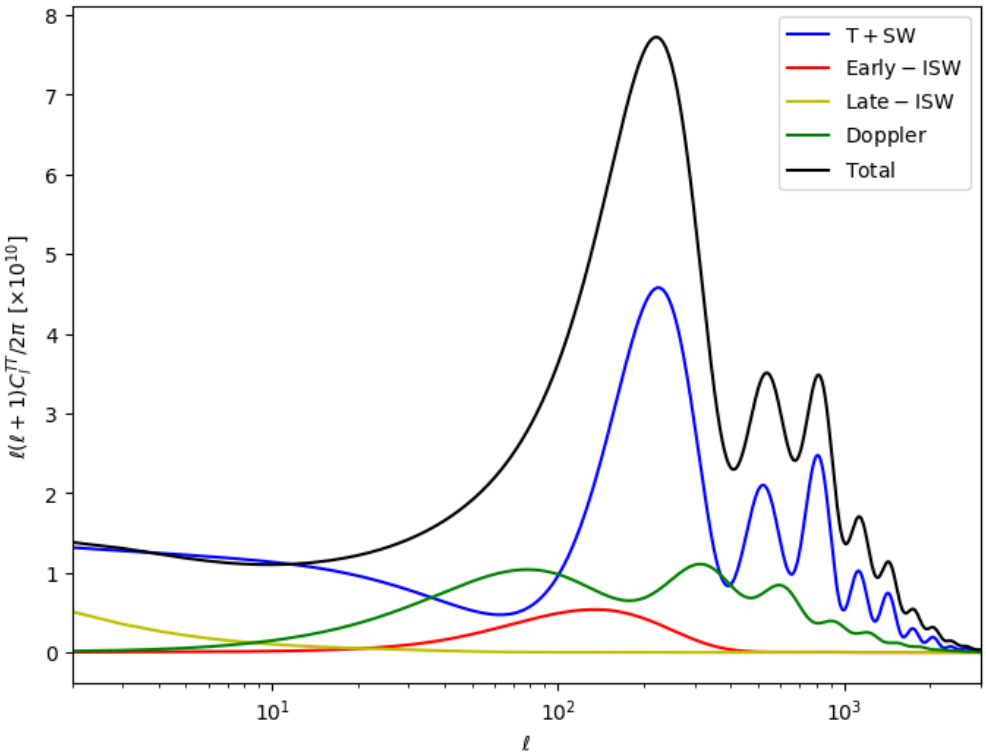

Figure 13 – Contribution of all CMB anisotropies to the C_l^{TT} spectrum.

3.2 Baryonic Acoustic Oscillations

As we discussed in the last section, before recombination and decoupling the universe consisted of a hot baryon-photon plasma. There were competing forces of radiation pressure and gravity, which set up the oscillations in the photon fluid (Eq. 3.43). Then, at recombination, the cosmos becomes neutral, the pressure on the baryons is removed. After recombination and decoupling, the photon pressure can no longer prevent gravitational instability in the baryons, defining the *drag epoch* [105].

The acoustic oscillations in the photon-baryon fluid imprinted their signatures on CMB − the acoustic peaks in the CMB angular power spectrum −, and also on the matter distribution

– the BAO in galaxy power spectrum. The observed BAO in the galaxy power spectrum have a characteristic scale, which is determined by the comoving sound horizon at the end of drag epoch, $r_d \equiv r_s(z_d)$ (Eq. 3.46). From Eq.s (1.62) and (3.46), neglecting the DE contribution to $z > z_d$, and considering a flat model, we can write

$$r_d = \int_{z_d}^{\infty} \frac{c_s}{H(z)} dz = \frac{1}{\sqrt{\Omega_m H_0^2}} \frac{2c}{\sqrt{3 z_{eq} R_{eq}}} ln \left(\frac{\sqrt{1+R_d} + \sqrt{R_d + R_{eq}}}{1+\sqrt{R_{eq}}} \right), \tag{3.50}$$

where $R = 3\rho_b/4\rho_\gamma \propto \Omega_b h^2/(1+z)$, with the subscripts eq, d respectively denoting the ratio R at $z_{eq} = \Omega_m/\Omega_r$, and z_d given by the fit formula that follows [106]

$$\begin{aligned} z_d &= 1291 \frac{(\Omega_m h^2)^{0.251}}{1+0.659\,(\Omega_m h^2)^{0.828}} \left[1 + b_1 \left(\Omega_b h^2\right)^{b_2}\right] \\ b_1 &= 0.313 \left(\Omega_m h^2\right)^{-0.419} \left[1 + 0.607 \left(\Omega_m h^2\right)^{0.674}\right] \\ b_2 &= 0.238 \left(\Omega_m h^2\right)^{0.223}. \end{aligned} \tag{3.51}$$

The last Planck results give $r_d = 147.05 \pm 0.30$ Mpc for the ΛCDM model [23].

3.2.1 Extracting the BAO Scale

The primary observable in the LSS is the matter density $\rho(\vec{x}, t)$, or some proxy such as the galaxy number density or *21-cm brightness temperature* (Eq. 3.58). The perturbation about the mean value of matter density, $\bar{\rho}(t)$, defines the density contrast

$$\delta(\vec{x}, t) \equiv \frac{\rho(\vec{x}, t) - \bar{\rho}(t)}{\bar{\rho}(t)}. \tag{3.52}$$

Instead the prediction about the precise matter density at a given location, the most important quantity predicted by theory is the *2-point correlation function* between matter densities. Presented by P. Peebles [134], it describes the probability that a galaxy will be found within a given distance from another random galaxy. Mathematically, it is defined as the spatial average of the density contrast product

$$\xi(r) \equiv \langle \delta(\vec{x}, t) \delta(\vec{x} + \vec{r}) \rangle, \tag{3.53}$$

which depends only on the modulus separation[3], r. Also, $\xi(r)$ is independent of the direction $\hat{r}$ (assuming statistical isotropy) and of $\vec{x}$ (assuming statistical homogeneity).

The BAO scale, $k_A = 2\pi/r_d$, can be extracted from galaxy surveys in three ways [108]: (i) using correlations in the direction perpendicular to the line of sight, (ii) using correlations

[3] In this sense, the scale given by Eq. (3.53) reflects the higher probability of finding two galaxies separated by the distance r_d.

in the direction parallel to the line of sight, (*iii*) and the angle-averaged measurement. The first two measures are made by comparing the observed galaxy distribution to a catalog of randomly simulated distributed galaxies. Pairs of galaxies are counted separated along the line of sight, $\vec{r}_{||}$, and transverse to the line of sight, $\vec{r}_{\perp}$, and used to estimate $\xi(r)$. It is necessary to convert redshift data to distance, which requires a fiducial model, usually the flat ΛCDM universe. A commonly used estimator of $\xi(r)$ is that of Landy-Szalay [109]

$$\xi(r) = \frac{DD - 2RD + RR}{RR}, \tag{3.54}$$

where DD is the normalized sum of weights of galaxy-galaxy pairs, coming from the data; RR is the normalized sum of weights of random-random pairs in the simulated catalog; DR is the normalized sum of weights of galaxy-random pairs, calculated by overlaying the real galaxy catalog and the simulated random galaxy catalog. The BAO scale was extracted first by Eisenstein *et al.* in 2005 from the spherically-averaged redshift-space correlation function from Sloan Digital Sky Survey (SDSS) Luminous Red Galaxies (LRG) sample [108], presented in Fig. 14.

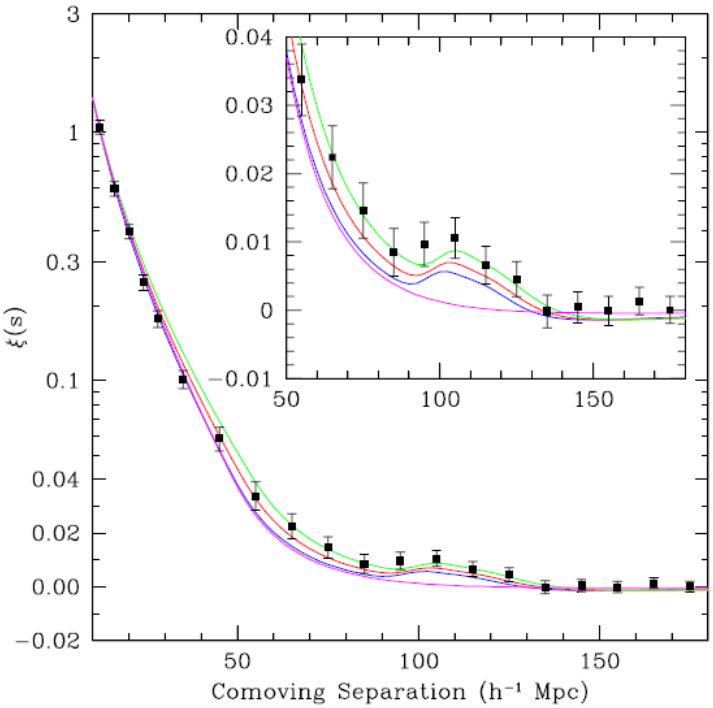

Figure 14 – The baryon acoustic peak in the correlation function from clustering of the SDSS LRG galaxy sample. The models are $\Omega_m h^2 = 0.12$ (top, green), 0.13 (red), and 0.14 (bottom with peak, blue), all with $\Omega_b h^2 = 0.024$, comoving number density $n = 0.98$ and with a mild non-linear prescription folded in. The magenta line shows a pure CDM model ($\Omega_m h^2 = 0.105$). Extracted from [108].

Another method to extract BAO scale, which provides an important cross-check, is to use the power spectrum analysis, a common choice on large scales, since it allows to recover the statistical independence in the face of survey boundary effects [108]. The power spectrum and correlation function contain the same information in principle, and are related via Fourier transform. From the two-point correlation function (Eq. 3.53), we define the *matter power spectrum* as the average of the density contrast product in Fourier space

$$\left\langle \delta(\vec{k})\delta^*(\vec{k}') \right\rangle \equiv (2\pi)^3 \delta^{(3)}(\vec{k}-\vec{k}')P_m(k), \tag{3.55}$$

where $\delta^{(3)}$ is the 3D Dirac delta function, and $\delta(\vec{k})$ is the Fourier transform of the matter density perturbation, given by

$$\delta(\vec{k}) = \mathcal{F}\left[\delta(\vec{x})\right] = \int d^3\vec{x}\delta(\vec{x})e^{i\vec{k}\cdot\vec{x}}. \tag{3.56}$$

3.2.2 21-cm Line & HI Maps

As we mentioned before, the BAO scale was first extracted using spherically-averaged redshift-space correlation function from SDSS LRG sample, by Eisenstein *et al.* in 2005. Since then, in the last two decades other optical or near-infrared galaxy surveys were used to constraining DE using the BAO ruler, such as Two degree Field (2dF) [112,113], Sloan Digital Sky Survey Data Release 7 (SDSS DR7) [114], WiggleZ [115], Six degree Field (6dF) [116], Baryon Oscillation Spectroscopic Survey (BOSS) [117], and others.

An alternative way to perform redshift surveys is in the radio frequency, using the 21-cm radiation from HI to select galaxies. The most common atomic species present in the universe ($\sim 75\%$ of the gas mass present in the IGM [118]), atomic Hydrogen, HI is a useful tracer of local properties of that gas mass. The 21-cm line is produced by the hyperfine splitting caused by the interaction between electron and proton magnetic moments separated by $\Delta E = 5.9 \times 10^{-6}$ eV, corresponding to a wavelength of 21.1 cm. Theoretically predicted by H. van de Hulst in 1942 [119], and first detected by H. Ewen and E. Purcell in 1951 [120], the 21-cm line has been used as a probe of astrophysics and cosmology.

There exists a particular technique to do radio redshift survey called HI IM [121–124]. The idea is not to detect individual galaxies throughout HI IM, but rather to measure the combined flux in wide patches of the sky containing many galaxies. The data obtained from HI IM can be analyzed in two ways: using 2-dimensional HI maps to calculate a set of angular power spectra, which in turn is used to constrain the cosmological parameters; extracting the BAO signal from the measured HI power spectrum to constrain the DE equation of state. In the last possibility, the BAO acoustic scale is extracted with the help of some fitting formula of the BAO wiggles, assuming that the HI power spectrum is only biased relative to the underlying DM distribution.

The physics of HI IM is based on the *brightness temperature* of the 21-cm line. The mean observed brightness temperature due to the average HI density in the universe is described by [125]

$$\bar{T}_{obs}(z) \equiv \langle T_{obs}(z) \rangle = \frac{\langle T_{emit}(z) \rangle}{1+z} = \left(\frac{\hbar c^3}{k_B} \frac{3A_{21}}{16 f_{emit}^2 M_H} \right) \left(\frac{\rho_{HI}(z)}{1+z} \right) \frac{dl}{dv}. \tag{3.57}$$

The first term of the last equality is just a combination of fundamental constants and measured experimental parameters (M_H is the mass of the hydrogen atom, A_{21} is the spontaneous emission coefficient of the 21-cm transition, and f_{emit} is the rest-frame emission frequency for HI); the second term is a function of redshift, with $\rho_{HI}(z)$ the average density of HI at redshift z; and the final term relates the line-of-sight distance to the recession velocity, given by H_0^{-1} in the local universe. After computing the last term, substituting the values for fundamental constants, and writing $\rho_{HI}(z)$ in terms of the HI density parameter, $\Omega_{HI}(z) = 8\pi G \rho_{HI}(z)/3H_0^2$, Eq. (3.58) becomes

$$\bar{T}_{obs}(z) = 44 \mu K \left(\frac{\Omega_{HI}(z) h}{2.45 \times 10^{-4}} \right) \frac{(1+z)^2}{E(z)}, \tag{3.58}$$

where $E(z) \equiv H(z)/H_0$.

The maps of brightness temperature, and ultimately, the 21-cm power spectrum depend on the model for the density of HI, $\Omega_{HI}(z)$. As the range of redshifts relevant to IM is in the post-reionization universe, it is common to assume that almost all the HI content is inside DM halos [127, 128], which is described by a model for the mass of HI, $M_{HI}(z)$, chosen based on both observational and theoretical arguments.

3.2.3 HI Angular Power Spectrum

In order to place constrains on the MG parameters from the 21-cm signal, we can compute the angular power spectrum for HI IM as follows [125] – ignoring peculiar velocities and the SW effects –

$$C_l^{ij} = \frac{2}{\pi} \int W^i(l,k,z) W^j(l,k,z) k^2 P_{cdm}(k) dk, \tag{3.59}$$

where $W^i(l,k,z)$ is the window function, defined as

$$W^i(l,k,z) = \int b_{HI}(k,z) \bar{W}^i(z) \bar{T}_{obs}(z) j_l(k\chi) D(z). \tag{3.60}$$

In the last equation, $b_{HI}(k,z)$ is the HI linear bias function, $\bar{W}^i(z)$ is the window function of the observation, $j_l(k\chi)$ is the order l spherical Bessel function, and $D(z)$ is the growth function, affected by the MG model studied in this work (2.60).

The concept of linear bias function arises from the description of how DM halos are correlated in space. A realistic treatment of DM halos must take into account that their positions *do not* remain unchanged as the structures grow. Considering this factor we obtain a more accurate description of the HI maps concerning the underlying DM overdensity. A detailed discussion about it can be found in Sec. 7.4 of [126].

The window function, $\bar{W}^i(z)$, assumed as uniform in the considered redshift range is defined as

$$\bar{W}^i(z) = \begin{cases} (z_{max} - z_{min})^{-1} & if \quad z_{min} \leq z \leq z_{max} \\ 0 & otherwise \end{cases}, \tag{3.61}$$

and the matter power spectrum $P_{cdm}(k)$ in Eq. (3.59) can be computed from

$$P_{cdm} = A_s k^{n_s} T^2(k), \tag{3.62}$$

where the transfer function $T(k)$ is given by fitting formulae due to Eisenstein & Hu [106]

$$T(k) = \frac{\Omega_b}{\Omega_0} T_b(k) + \frac{\Omega_{cdm}}{\Omega_0} T_c(k), \tag{3.63}$$

where $\Omega_0 = \Omega_b + \Omega_{cdm}$, and

$$
\begin{aligned}
T_c(k) &= f\tilde{T}_0(k,1,\beta_c) + (1-f)\tilde{T}_0(k,\alpha_c,\beta_c), && \text{(3.64a)}\\
T_b(k) &= \left[\frac{\tilde{T}_0(k;1,1)}{1+(kr_s/5.2)^2} + \frac{\alpha_b}{1+(\beta_b/kr_s)^3}e^{-(k/k_{silk})^{1.4}}\right] j_0(k\tilde{r}_s), && \text{(3.64b)}\\
f &= \frac{1}{1+(kr_s/5.4)^4}, && \text{(3.64c)}\\
\tilde{T}_0(k,\alpha_c,\beta_c) &= \frac{ln(e+1.8\beta_c q)}{ln(e+1.8\beta_c q)+Cq^2}, && \text{(3.64d)}\\
C &= \frac{14.2}{\alpha_c} + \frac{386}{1+69.9q^{1.08}}, && \text{(3.64e)}\\
q &= \frac{k}{13.41k_{eq}}, && \text{(3.64f)}\\
\alpha_c &= a_1^{-\Omega_b/\Omega_0} a_2^{-(\Omega_b/\Omega_0)^3}, && \text{(3.64g)}\\
a_1 &= (46.9\Omega_0 h^2)^{0.670}[1+(32.1\Omega_0 h^2)^{-0.532}], && \text{(3.64h)}\\
a_2 &= (12.0\Omega_0 h^2)^{0.424}[1+(45.0\Omega_0 h^2)^{-0.582}], && \text{(3.64i)}\\
\alpha_b &= 2.07k_{eq}r_s(1+R_d)^{-3/4}G\left(\frac{1+z_{eq}}{1+z_d}\right), && \text{(3.64j)}\\
G(y) &= y\left[-6\sqrt{1+y}+(2+3y)ln\left(\frac{\sqrt{1+y}+1}{\sqrt{1+y}-1}\right)\right], && \text{(3.64k)}\\
\beta_c^{-1} &= 1+b_1[(\Omega_{cdm}/\Omega_0)^{b_2}-1], && \text{(3.64l)}\\
b_1 &= 0.944[1+(458\Omega_0 h^2)^{-0.708}]^{-1} && \text{(3.64m)}\\
b_2 &= (0.39\Omega_0 h^2)^{-0.0266}, && \text{(3.64n)}\\
\beta_b &= 0.5+\frac{\Omega_b}{\Omega_0}+\left(3-2\frac{\Omega_b}{\Omega_0}\right)\sqrt{(17.2\Omega_0 h^2)^2+1}, && \text{(3.64o)}\\
\tilde{r}_s(k) &= \frac{r_s}{[1+(\beta_{node}/kr_s)^3]^{1/3}}, && \text{(3.64p)}\\
\beta_{node} &= 9.41(\Omega_0 h^2)^{0.435}. && \text{(3.64q)}
\end{aligned}
$$

3.2.4 RSD Effect

Measurements of RSD are an important tool to put constraints in MG theories since they are related to the growth of structures. To understand RSD effects, let us recall some facts. In deriving the Hubble law (Eq. 3.59), it was implicitly assumed that the movement of an observed object was only due to the expansion of the universe. However, taking the time derivative of the observed position, $x^i_{obs} = a(t)x^i$ we get

$$v^i_{obs} = Hx^i_{obs} + v^i_{pec}. \tag{3.65}$$

Apart from the first term (the Hubble flow), now appears a second physical quantity which describes the *peculiar velocity* of the object in question. The RSD effect arises as deviations

in that velocity caused by the matter overdensities gravitational pull, inducing anisotropies in redshift space. Depending on the scale, such anisotropies leave specific imprints on the field clustering pattern.

On large linear scales, we have the Kaiser effect [134] which is a squashing effect along the line-of-sight produced into high-density field regions, as shown by Fig. 15. On smaller non-linear scales, we have the Fingers-of-God effect [130] where the density field is stretched and structures seem elongated along the line-of-sight.

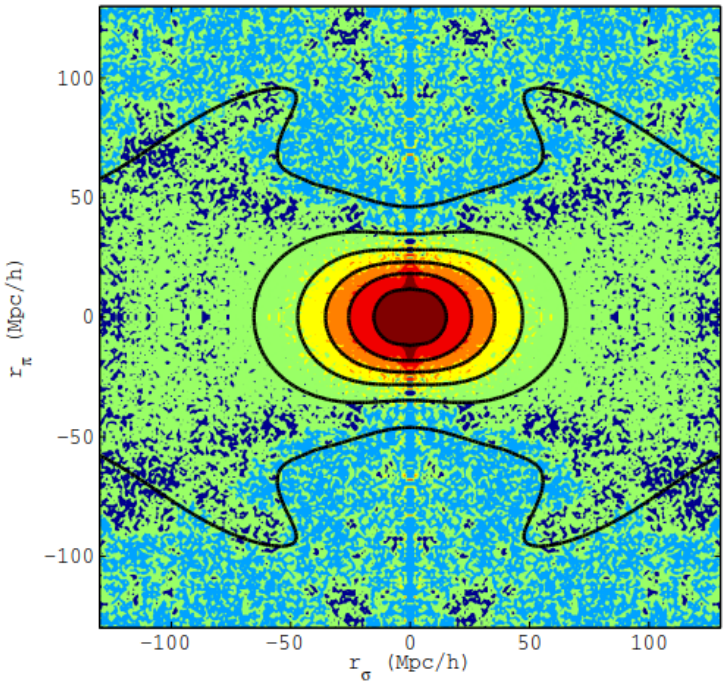

Figure 15 – Two-dimensional correlation function of BOSS galaxies (color) compared with the best-fit model (black lines). Extracted from [131].

The RSD effect is characterized by the *parameter distortion*, $\beta(z)$, defined as

$$\beta(z) \equiv \frac{f(z)}{b(z)}, \tag{3.66}$$

where $f(z)$ is the growth rate (Eq. 2.66), and $b(z)$ is the linear bias with respect to the underlying field – in our case, HI. Then, in the observed redshift-space clustering, MG theories causing slower or faster growth give smaller or larger anisotropic distortions. Following the spherical harmonic approach to redshift distortion developed by Fisher *et al.* [132], RSD effects for HI IM appear into angular power spectrum included in the window function

$$\begin{aligned} W^i_{RSD}(l,k,z) &= \frac{\beta(z)}{k}\int d\chi \bar{T}_{obs}(\chi)\left[\frac{2l^2+2l-1}{(2l+3)(2l-1)}j_l(k\chi)+\frac{l(l-1)}{(2l-1)(2l+1)}j_{l-2}(k\chi)-\right. \\ &- \left.\frac{(l+1)(l+2)}{(2l+1)(2l+3)}j_{l+2}(k\chi)\right], \end{aligned} \tag{3.67}$$

where the parameter distortion quantify the amplitude of RSD effects and is small for wide $\bar{T}_{obs}$. Thus, the total window function that must enter in Eq. (3.59) reads

$$W^i_{Tot}(l,k,z) = W^i(l,k,z) + W^i_{RSD}(l,k,z). \tag{3.68}$$

Usually, predictions for the modified growth function are compared with the bias-independent data of the form $f\sigma_8$ [133], where σ_8 is the variance (Eq. 3.59) of the density field filtered at the scale[4] $R = 8h^{-1}$ Mpc. The RSD signal is well determined from HI IM experiments, given its precise method for determining the redshift.

3.2.5 UCLC_l Code

To compute the angular power spectrum (Eq. 3.59), we make use of the UCLC_l. It extracts the power spectrum, P_{cdm}, from CLASS code, and deals with the redshift distribution in more flexible ways than does CLASS and CAMB [134]. Such a code is related to the UCLC_l PARAM-EST, used to make parameter inference (see Subsec. 4.2.1).

3.2.6 BINGO Survey

There are many post-reionization epoch experiments underway to map the HI emission, such as Square Kilometre Array (SKA) [135], Canadian Hydrogen Intensity Mapping Experiment (CHIME) [136], Tianlai Telescope [137], Five hundred metre Aperture Spherical Telescope (FAST) [138], Hydrogen Intensity and Real-Time Analysis experiment (HIRAX) [139], and BINGO [11–17].

The BINGO project is a single-dish radio telescope that aims at mapping the HI emission from 980 to 1260 MHz frequencies (which correspond to the redshift range of $z = 0.127 - 0.449$) over a sky area of 6000 square degrees [11]. The telescope is being built in the hills of "Serra da Catarina" in the municipality of Aguiar, Paraíba, Brazil, and is funded by several Brazilian and Chinese agencies.

Among the scientific goals are: (*i*) Cosmological ones, that aim to use HI IM as a tool to measure BAO and RSDs to study extensions of the ΛCDM model and alternative cosmologies, such as dynamical DE, interacting DE and MG; and (*ii*) Astrophysical ones, that aim to investigate transient objects, such as Fast Radio Bursts (FRBs) and pulsars.

Although operating in the same redshift range of some radio telescope projects cited above, BINGO can contribute, producing good quality data, being a strong competitor. For instance, BINGO observations can give early hints to the SKA project for what to look for in the

[4] In Eq. (3.59), we have implicitly assumed a unity volume, R, to compute the C_l's. However, for any R, they are given by $\frac{1}{2\pi^2}\int_0^\infty dk k^2 P(k,z)\,|W(kR)|^2$.

cosmic dawn, and since BINGO will be located in the Southern hemisphere, it can contribute to confirming the science explored by the FAST project, which is in the Northern hemisphere.

Figure 16 – BINGO telescope site - artist's view. Extracted from [11].

3.2.7 Lognormal Fields

The HI, mapped soon by BINGO observations, can be simulated as multivariate lognormal random fields. This way to model LSS observables has been applied in the past to the matter density and WL convergence, and has as motivation the fact that such fields, just mentioning these two, have lower limits which do not follow Gaussian distributions, and they show significant skewness and heavy tails at large values, leading to non-physical densities. In order to overcome this problem we can consider a multivariate shifted Lognormal distribution [140, 141]

$$X_i = e^{Z_i} - \lambda_i, \tag{3.69}$$

where Z_i follow a multivariate Gaussian distribution, and the shift $X_{min} = -\lambda_i$ specifies the minimum value of the Lognormal distribution, translating it around the space populated by the variables. X_i depend on 3 parameters: 2 fixed Gaussian ones, μ_i and σ_i, and 1 free, λ_i − determined theoretically as in [18], or fitted through N-body simulations as in [142]. The connection between Gaussian and lognormal variables − mean and variance − is given as follows. The lognormal mean value, $\langle X_i \rangle$, can be obtained from Eq. (3.69) by expanding the

exponential as

$$\langle e^{Z_i} \rangle = e^{\mu_i} \langle e^{Z_i - \mu_i} \rangle = e^{\mu_i} \sum_{n=0}^{\infty} \frac{\langle (Z_i - \mu_i)^n \rangle}{n!}, \tag{3.70}$$

and recalling the relation for Gaussian central moments

$$\langle (Z_i - \mu_i)^n \rangle = \begin{cases} 0, & if \;\; n \;\; is \;\; odd \\ \frac{n!}{(n/2)!} \left(\frac{\sigma_i^2}{2} \right)^{n/2}, & if \;\; n \;\; is \;\; even \end{cases} \tag{3.71}$$

we get

$$\langle X_i \rangle = e^{\mu_i + \frac{\sigma_i^2}{2}} - \lambda_i. \tag{3.72}$$

This result enables us to define a useful quantity

$$\alpha_i \equiv \langle X_i \rangle + \lambda_i = e^{\mu_i + \frac{\sigma_i^2}{2}} > 0, \tag{3.73}$$

from which we can write the covariance matrix, the variance, and the skewness for a Lognormal distribution as a function of Gaussian parameters, respectively as[5]

$$\mathcal{C}_{ln}^{ij} \equiv \langle X_i X_j \rangle - \langle X_i \rangle \langle X_j \rangle = \alpha_i \alpha_j (e^{\mathcal{C}_g^{ij}} - 1), \tag{3.74a}$$

$$v_i \equiv \langle X_i^2 \rangle - \langle X_i \rangle^2 = \alpha_i^2 (e^{\sigma_i^2} - 1), \tag{3.74b}$$

$$\gamma_i \equiv \frac{\langle (X_i - \langle X_i \rangle)^3 \rangle}{v_i^{3/2}}. \tag{3.74c}$$

The Gaussian case can be recovered from the lognormal one by setting the skewness to zero. To construct maps made of fields that follow Lognormal distributions in real space, it is necessary to relate the associated angular power spectrum with its Gaussian counterpart, which is given by[6]

$$C_g^{ij}(l) = 2\pi \int_0^{\pi} ln \left[\sum_{l'=0}^{\infty} \frac{(2l'+1)}{4\pi} \frac{C_{ln}^{ij}(l')}{\alpha_i \alpha_j} P_{l'}(\cos\theta) + 1 \right] P_l(\cos\theta) \sin\theta d\theta. \tag{3.75}$$

3.2.8 FLASK Code

The covariance matrix (Eq. 4.11) associated with the measurements of lognormal random distribution of HI can be computed by using the FLASK code [18]. FLASK is a publicly available code that has the purpose of generating 2-dimensional random realizations of astrophysical fields, following either a multivariate Gaussian distribution or a multivariate Lognormal distribution. If we consider the latter case, then we must provide as input a file

[5] The subscript ln refers to Lognormal distribution, while the g one indicates the Gaussian distribution.

[6] We may notice that the multipoles described by $C_{ln}^{ij}(l)$ are not themselves lognormal in harmonic space.

containing a table of fields' means, shifts, and redshift ranges, and a set of angular auto and cross power spectra, $C_{ln}^{ij}(l)$, for all fields at all redshift slices.

Then, the code uses Eq. (3.75) to get the Gaussian angular power spectrum, and performs the Cholesky decomposition,

$$C_{g,l}^{ij} = \sum_k T_{ik,l} T_{kj,l}, \tag{3.76}$$

where $T_{ik,l}$ form a lower triangular matrix, and $T_{kj,l}$ are the components of its conjugate transpose. Such decomposition is valid only if $C_{g,l}^{ij}$ is positive-definite. If the positivity condition is not attended, FLASK can distort the covariance matrices, $\mathcal{C}_g$, as little as possible so they become positive-definite. The correlated Gaussian multipoles are generated from a set of standard (zero mean and unit variance) independent Gaussian variables, $Z_{k,lm}^0$, as

$$Z_{i,lm} = \sum_k T_{ik,l} Z_{k,lm}^0, \tag{3.77}$$

with the expected values following the usual relation $\langle Z_{lm}^i Z_{l'm'}^j \rangle = \delta_{ll'} \delta_{mm'} C_{g,l}^{ij}$. Once we get the multipoles, $Z_{i,lm}$, maps of lognormal fields are generated using the ALM2MAP HEALPIX function from the local transformation

$$X_i(\hat{n}) = e^{\mu_i} e^{Z_i(\hat{n})} - \lambda_i, \tag{3.78}$$

where

$$e^{\mu_i} = (\langle X_i \rangle + \lambda_i) e^{-\sigma_i^2/2}, \tag{3.79a}$$

$$\sigma_i^2 = \sum_{l_{min}}^{l_{max}} \frac{2l+1}{4\pi} C_{g,l}^{ij}. \tag{3.79b}$$

4 Analysis

In this chapter, we present the necessary tools to make statistical inferences on the cosmological parameters. From the observables, described in the previous chapter, we do that by applying Bayesian methods, which have been used in cosmology and astrophysics due to their higher efficiency to deal with problems of induction from observations, comparing these last ones with theoretical models. We do not present all the vast aspects of Bayesian statistics, but only those resources of interest to manipulate and analyze parameters, recovered from MCMC processes. We follow mainly [143].

4.1 Bayesian Statistics

Bayesian statistics is based on the definition of *probability as a measure of the degree of belief about a proposition* [144]. This point of view about probability is concerned with the question of what can be learned from the observed data, in an opposite way to the classical definition of probability, which predicts the outcomes of data, given the properties of the underlying distributions. One virtue of the Bayes framework is that the parameters describing a theory can have their estimated values updated when new observations become available.

Other advantages of Bayes probability are that it applies to any event, regardless whether we are considering repeated experiments or one-off situations; it deals with uncertainty independently of its origin, *i.e.* there is no distinction between statistical uncertainty − coming from the finite precision of the measurement apparatus −, and systematic uncertainty − derived from deterministic effects such as the calibration uncertainty of a detector[1]. In the Bayesian scenario, we can consider, at least, three levels of inference, as shown in Tab. 1. In this work, we make use of only the first one.

[1] A more detailed discussion can be found in [143].

Table 1 – Three different levels of inference. Adapted from [145]

Level 1 - Parameter inference	Level 2 - Model comparison	Level 3 - Model averaging
We have selected a model, $\mathcal{M}$, and a prior, $P(\Theta\|\mathcal{M})$. What are the parameters? Use Bayes Theorem	Actually, there are several possible models: $\mathcal{M}_0$, $\mathcal{M}_1$, ... What is the relative plausibility of $\mathcal{M}_0$, $\mathcal{M}_1$, ... given the observed data?	None of the models is clearly the best. What is the inference on the parameters accounting for model uncertainty? Model averaging
$P(\Theta\|d,\mathcal{M}) = \frac{P(d\|\Theta,\mathcal{M})P(\Theta\|\mathcal{M})}{P(d\|\mathcal{M})}$	$odds = \frac{P(\mathcal{M}_0\|d)}{P(\mathcal{M}_1\|d)}$	$P(\Theta\|d) = \sum_i P(\mathcal{M}_i\|d)P(\Theta\|d,\mathcal{M}_i)$
e.g. parameter determination by running PLINY [158] or COSMOMC [159]	*e.g.* comparison of ΛCDM and wCDM as in [146]	*e.g.* finding curvature of the universe as in [147] or evolving DE as in [148]

4.1.1 Bayes Theorem

Bayesian statistical inference is condensed in Bayes theorem, which is derived from the axioms of probability as degree of belief. Let us consider a proposition, A, and its negation, $\bar{A}$, conditional on an information, I, that is assumed to be true. Then, the axioms of probability read

◇ *Sum rule*

$$p(A|I) + p(\bar{A}|I) = 1$$

◇ *Product rule*

$$p(A,B|I) = p(A|B,I)p(B|I)$$

The product rule says that the joint probability of A and B is equal to the probability of A given that B occurs times the probability of B occurring on its own. Since, $p(A,B|I) = p(B,A|I)$, we get

$$p(B|A,I) = \frac{p(A|B,I)p(B|I)}{p(A|I)}. \tag{4.1}$$

We can interpret this equation by making the replacements: $A \to d$ (observed data), $B \to \Theta$ (set of parameters we want to assess, with $\Theta = \{\theta_i\}$), and $I \to \mathcal{M}$ (information from the model), obtaining

$$p(\Theta|d,\mathcal{M}) = \frac{p(d|\Theta,\mathcal{M})p(\Theta|\mathcal{M})}{p(d|\mathcal{M})}. \tag{4.2}$$

On the left-hand side, $p(\Theta|d,\mathcal{M})$ is the *posterior probability* that the inferred parameters are true given we observe the data. It is proportional to the *sampling distribution* of the data,

$p(d|\Theta, \mathcal{M})$, assuming the parameters are true, times the *prior probability* for the parameters, $p(\Theta|\mathcal{M})$, which represents our state of knowledge before seeing the data. The posterior probability is normalized to unity by the *Bayesian evidence*, $Z \equiv p(d|\mathcal{M})$, a central quantity for model comparison purposes, given by

$$Z = \int p(d|\Theta, \mathcal{M}) p(\Theta|\mathcal{M}) d\Theta. \tag{4.3}$$

4.1.2 Parameter Inference

In order to constrain the MG parameters in a Bayesian framework, we must start providing a functional form for the prior and sampling distribution. Given such functions and the data, we can employ numeric techniques to compute the posterior probability, and use it to obtain the parameters. Often, for each posterior computed − after passing some test −, the algorithm updates those functions with new input values, assumed as true, and repeat the process of compute-test-update until some convergence criterion is reached (see Sec. 4.2).

4.1.3 Prior

The form of the prior function is a fundamental ingredient for Bayesian statistics, once it contains our state of knowledge about the parameters. A standard choice, is to take a *flat prior*, a function assumed to be constant within some minimum and maximum value of the parameter. It allows us to assign equal probability to equal states of knowledge in which the prior is taken. Mathematically, it is defined as

$$p(\theta_i|\mathcal{M}) = \begin{cases} (\theta_{i,max} - \theta_{i,min})^{-1} & for \;\; \theta_{i,min} \leq \theta_i \leq \theta_{i,max} \\ 0 & otherwise \end{cases}. \tag{4.4}$$

Apart from the normalization term, it results in a posterior functionally identical to the sampling distribution. Even if we start with different states of knowledge, if there are sizeable data available, and the sampling distribution is more informative than the priors, the repeated application of the Bayes theorem will lead to a common posterior probability. Thus, the assignment of the prior becomes eventually irrelevant. However, for small sample sizes, or for problems where the dimensionality of the parameter space is larger than the number of observations, the final inference highly depends on the form of prior function. For further details on the prior choice, we recommend Chap. 5 of [149].

4.1.4 The Likelihood Function

For fixed observed data, the sampling distribution, $p(d|\Theta, \mathcal{M})$, depends only on the model we have − which already contains the parameters. Considered as a function of the hypothesis,

it is referred in literature as *likelihood function*, for which we employ the shortcut notation $\mathcal{L}(\Theta) \equiv p(d|\Theta, \mathcal{M})$. The central step in constraining a set of parameters is to construct the likelihood function for the measurement, which usually reflects the way the data are obtained − common examples are binomial, Poisson, and Gaussian distributions.

Given the likelihood, to determine the best value of a parameter, we must find the maximum posterior probability. This can be done by maximizing the likelihood function, and by minimizing the Bayes evidence. From analytical cases, which summarize the maximization problems as

$$\left.\frac{\partial \mathcal{L}(\Theta)}{\partial \theta_i}\right|_{\theta_{max}} = 0 \qquad \textit{and} \qquad \left.\frac{\partial^2 \mathcal{L}(\Theta)}{\partial \theta_i^2}\right|_{\theta_{max}} < 0, \tag{4.5}$$

and considering a flat prior, we perform a Taylor expansion of the log likelihood, close to the maximum value of parameters

$$ln\mathcal{L}(\Theta) = ln\mathcal{L}(\theta_{max}) + \frac{1}{2}\left(\theta^i - \theta_{max}\right)\frac{\partial^2 ln\mathcal{L}(\Theta)}{\partial\theta^i\partial\theta^j}\left(\theta^j - \theta_{max}\right) + \cdots . \tag{4.6}$$

Up to second-order expansion, we see that the likelihood is, locally, a multivariate Gaussian in parameter space

$$\mathcal{L}(\Theta) = \mathcal{L}(\theta_{max}) exp\left[-\frac{1}{2}\left(\theta^i - \theta_{max}\right) H_{ij}\left(\theta^j - \theta_{max}\right)\right], \tag{4.7}$$

where $H_{ij} \equiv -\frac{\partial^2 ln\mathcal{L}(\Theta)}{\partial\theta^i\partial\theta^j}$ is the *Hessian matrix*, which controls whether the estimates of θ_i and θ_j are correlated or not, with i, j summed over the quantity of parameters in parameter space. If $i = j$, then θ_i and θ_j are said to be *correlated*; on the other hand, if $i \neq j$, then θ_i and θ_j are said to be *uncorrelated*.

From Eq. (4.7), we define the *chi-square function*, an important quantity to evaluate how well our model fit the data,

$$\chi^2(\Theta) \equiv \sum_{i,j}\left(\theta^i - \theta_{max}\right) H_{ij}\left(\theta^j - \theta_{max}\right). \tag{4.8}$$

The χ^2 represents the level of agreement between the measurements and the fitted function, and so it can be used for assessing the goodness-of-fit. The parameter values that give the lowest chi-square, χ^2_{min}, are the best-fit parameters of the model. Normalized to unit, then the Gaussian likelihood function reads

$$\mathcal{L}(\Theta) = \frac{1}{\sqrt{|2\pi\mathcal{C}|}} exp\left[-\frac{1}{2}\chi^2(\Theta)\right], \tag{4.9}$$

where the chi-square,

$$\chi^2(\Theta) = \sum_{i,j}\left(\theta^i - \mu\right)\mathcal{C}^{-1}_{ij}\left(\theta^j - \mu\right), \tag{4.10}$$

is expressed in terms of the measured *covariance matrix*,

$$\mathcal{C}_{ij} \equiv \frac{1}{n-1} \sum_{i,j=1}^{n} (\theta_i - \mu)(\theta_j - \mu)^T, \tag{4.11}$$

with n the set of measurements for the parameters, and $\mu = \langle \theta_i \rangle$ their mean values.

4.1.5 Marginalization

Nuisance parameters related to the measurement process might be present in the likelihood, which are removed from the posterior probability by a process called *marginalization*: the integration of the posterior probability over all parameters which we are not interested in. Assuming we have a set of physically interesting parameters, θ_i, and a set of nuisance parameters, θ_j, the joint posterior for $\Theta = (\theta_i, \theta_j)$, marginalized over θ_j reads

$$p(\theta_i|d, \mathcal{M}) \propto \int \mathcal{L}(\Theta) p(\Theta|\mathcal{M}) d\theta_j. \tag{4.12}$$

The final step in the inference on θ_i from the posterior can then be obtained by the estimator $\hat{\theta}_i$, corresponding to the most probable value of the parameter, given by

$$\hat{\theta}_i = \int p(\theta_i|d, \mathcal{M}) \theta_i d\theta_i, \tag{4.13}$$

or, more usefully, by plotting one or two dimensional subsets of θ_i, with the other components marginalized over.

4.1.6 Confidence Level

The posterior probability may be used to determine regions that will have a given probability of containing the true value of the inferred parameter. In 1-dimension, an interval $[\theta_{lo}, \theta_{up}]$ can be determined through the fraction $1 - \alpha$ of the posterior probability, given by [150]

$$1 - \alpha = \int_{\theta_{lo}}^{\theta_{up}} p(\theta|d, \mathcal{M}) d\theta. \tag{4.14}$$

Considering the Gaussian distribution, with known standard deviation, σ, the probability that the inferred value, θ_i, will fall within the interval $[\mu - \delta, \mu + \delta]$ is

$$1 - \alpha = \frac{1}{\sqrt{2\pi}\sigma} \int_{\mu-\delta}^{\mu+\delta} exp\left[-\frac{1}{2} \left(\frac{\theta_i - \mu}{\sigma} \right)^2 \right] d\theta_i = erf\left(\frac{\delta}{\sqrt{2}\sigma} \right), \tag{4.15}$$

where erf is the Gaussian error function. This equation can be re-expressed in terms of the chi-square function, by using the cumulative distribution function $F(\chi^2, n)$ as

$$\alpha = 1 - F\left(\chi^2, n\right), \tag{4.16}$$

for $\chi^2 = (\delta/\sigma)^2$ and $n = 1$ degree of freedom. For multivariate measurements of n inferred parameters $\hat{\theta} = (\hat{\theta}_1, ..., \hat{\theta}_n)$, the construction of the confidence region requires the full covariance matrix (Eq. 4.11).

In 2-dimension, we have the standard error ellipse for the pair $\left(\hat{\theta}_i, \hat{\theta}_j\right)$, corresponding to a contour $\chi^2 = \chi^2_{min} + 1$ or $ln\mathcal{L} = ln\mathcal{L}_{max} - 1/2$. The ellipse is centered about the inferred values $\hat{\theta}_i$, and the tangents to the ellipse give the standard deviations of the estimators, *i.e.* σ_i and σ_j. Contours of constant $ln\mathcal{L}$ or χ^2 cover the true values, with confidence region determined by

$$ln\mathcal{L}\left(\theta\right) \geq ln\mathcal{L}_{max} - \Delta ln\mathcal{L} \qquad or \qquad \chi^2\left(\theta\right) \leq \chi^2_{min} - \Delta\chi^2. \tag{4.17}$$

Values of $\Delta\chi^2$ or $\Delta ln\mathcal{L}$ are given in Table 2 for some values of the coverage probability, $1-\alpha$, and number of fitted parameters, n, computed as: $\Delta\chi^2 = 2\Delta ln\mathcal{L} = F^{-1}_{\chi^2_{min}}(1-\alpha)$, where $F^{-1}_{\chi^2_{min}}$ is the inverse of the cumulative distribution for n degrees of freedom.

Table 2 – Values of $\Delta\chi^2$ or $2\Delta ln\mathcal{L}$ corresponding to a coverage probability $1-\alpha$ in the large data sample limit, for joint estimation of n parameters. Extracted from [150].

$(1-\alpha)(\%)$	$n=1$	$n=2$	$n=3$
68.27	1.00	2.30	3.53
90.	2.71	4.61	6.25
95.	3.84	5.99	7.82
95.45	4.00	6.18	8.03
99.	6.63	9.21	11.34
99.73	9.00	11.83	14.16

4.2 Parameter Inference via MCMC Techniques

Markov Chain Monte Carlo (MCMC) method is a technique to solve a problem by determining a parameter of a hypothetical population, using random variables to construct a sampler, from which statistical estimates are extracted. MCMC is used in many areas of knowledge, from complex physical phenomena to economic problems. In the context of Bayesian inference, for the case where analytical solutions for the posterior probability do not exist − or are insufficiently accurate −, we need to use MCMC techniques to explore the parameter space in order to find out the best value of the parameters.

A *Markov chain* is defined as a sequence of n random variables in parameter space $\{\theta_0, \theta_1, ..., \theta_{n-1}\}$, where the probability of the $(n+1)-th$ parameter in the chain only depends on the value of the $n-th$ element. The chain starts somewhere in parameter space, jumping to another set of parameters to test. If the second point shows a higher likelihood, then

the algorithm starts from there and makes another jump; if the second point has a smaller likelihood, the algorithm decides whether to keep the new step or return to its previous step and try again − a formal development of MCMC theory can be found in [151].

The Markov chains converge to a stationary state when the parameter does not change its value with n. The density of points left in the track is proportional to the posterior probability, which can be used to infer a (marginalized) parameter θ_i via Eq. (4.13). The choice of algorithm depends on the characteristics of the problem. The popular ones include the Metropolis-Hastings algorithm [152, 153], Gibbs sampling [154], Hamiltonian Monte Carlo [155], etc. As problems become more complex, however, with larger parameter spaces of higher dimensionality, these algorithms become inefficient. To address such an issue, over the last decades the nested sampling has gained popularity.

4.2.1 UCLC_l PARAM-EST & PLINY

Nested sampling was developed to calculate the Bayesian evidence, but also can be used to make parameter inference since it generates weighted samples of the posterior distribution [156]. Starting with a set of N "live-points" from the prior, the algorithm computes the likelihoods, seeking for their minimum values, $\mathcal{L}(\theta_{min})$. Further points are sampled from these last ones until another likelihood with $\mathcal{L} > \mathcal{L}(\theta_{min})$ is found. When it occurs, then θ_{min} is moved to a chain with an associated weight, ω. The procedure of sampling and replacing is repeated until some convergence criterion is attended. In this way, nested sampling rapidly restricts the sampler to regions of high likelihoods, and, at the same time, it gives to us the minimum Bayesian evidence, computed from the chain, as we will see below.

In this work, it was used UCLC_l PARAM-EST code to sample the parameter space, implementing PLINY algorithm to find the maximum likelihood region[2] [158]. PLINY implements an ellipsoidal sampler, determining a Minimum-Volume Covering Ellipsoid (MVCE) of the live-points through the *dual reduced Newton* algorithm. The evidence is given by

$$Z = \sum_i \omega_i \mathcal{L}_i, \qquad with \qquad \omega_i = e^{-i/N} sinh(1/N). \tag{4.18}$$

The convergence criterion is defined through

$$\frac{e^{-i/N}}{N} \sum_i < t \sum_i \omega_i \mathcal{L}_i, \tag{4.19}$$

and it occurs for the step $i = I$, when the live-point test reaches the tolerance ratio, t.

[2] UCLC_l PARAM-EST also accepts MULTINEST [157], but its algorithm can lead to an ellipsoid with volume much larger than the true MVCE, and hence with poor acceptance. Therefore, we prefer PLINY, which is a more accurate algorithm, and uses an efficient Message Passing Interface (MPI) communication scheme.

5 Cosmological Parameter Constraints

In order to constrain the cosmological parameters we mimic the BINGO data by computing the covariance matrix through 500 FLASK simulations, and defining the bias and Ω_{HI} to be same as those from Horizon Run 4 (HIR4) mock [16]. HIR4 is a N-body simulation that generates HI IM in a more realistic way than FLASK by using a technique of populating the HI mass in DM halos, describing non-linearities present in the formation of the LSS. Due to its computational cost, HIR4 is less convenient to build the covariance matrix, and thus we prefer FLASK to do that. The BINGO maps were built from theoretical 21-cm angular power spectra, computed by UCLC_l with fiducial values set up to the WMAP5 cosmology [160] ($\Omega_{cdm} = 0.21$, $\Omega_\Lambda = 0.74$, $h = 0.72$), and considering the bias and Ω_{HI} coming from HIR4 mock; thermal noise, shot noise and other sources of noise were not included in such HI maps.

Our likelihood is obtained from that of Eq. (4.9), just by doing the replacements that follows: $\theta^i \to C_l^{obs}$ and $\mu \to C_l^{th}$, where C_l^{obs} stands for the observational data, and C_l^{th} are the 21-cm theoretical angular power spectra, computed taking into account the MG model (2.60). In Fig. 17 we show the 21-cm theoretical angular power spectra for the $\alpha_i \propto \Omega_{DE}$ parameterization, corresponding to 3 out 30 frequencies of BINGO, and considering the MG model defined by the fiducial values of Eq. (2.60): the lowest frequency, 965 MHz, the central, 1115 MHz, and the highest, 1255 MHz.

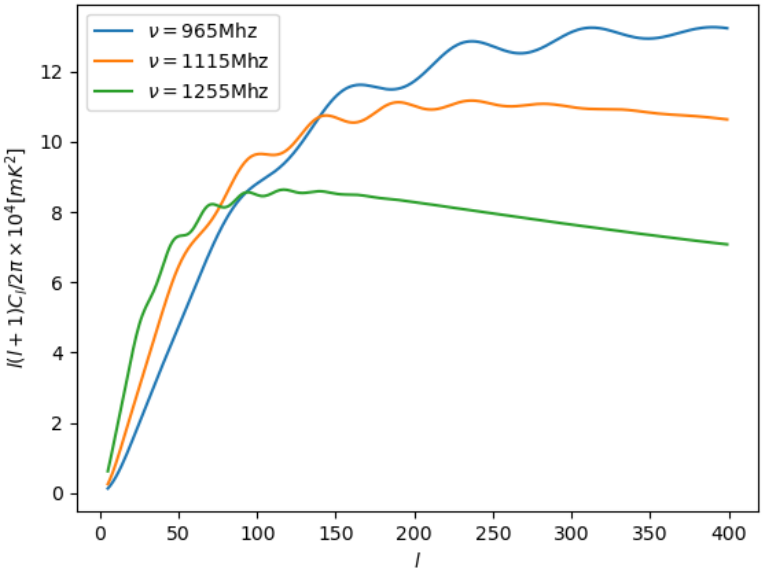

Figure 17 – Angular power spectra of three typical BINGO frequencies using $\alpha_i \propto \Omega_{DE}$ parameterization.

In table 3 we list the prior ranges for the different α_i parameterizations.

Table 3 – Prior range for the samplings.

Parameterization	Parameter	Prior Range
	Ω_{cdm}	0,0.4
	h	0.55,0.85
$\alpha_i \propto \Omega_{DE}$	α_M	-6,6
	α_B	-6,6
$\alpha_i \propto a$	α_M	-4,4
	α_B	-4,4

Taking into account the MG model (2.60), we initially consider α_T as a fixed parameter, and we only allow α_M and α_B to vary. As pointed out by [161], α_K is made up the combination of the G_i and their derivatives that is "orthogonal" to the parameter space probed by linear cosmology, and therefore it is hardly constrained by the data used here. In fact, as we can see in Fig. 18, varying the kineticity almost does not change the angular power spectra. Because of that, we omitted α_K since it does not affect constraints on other parameters.

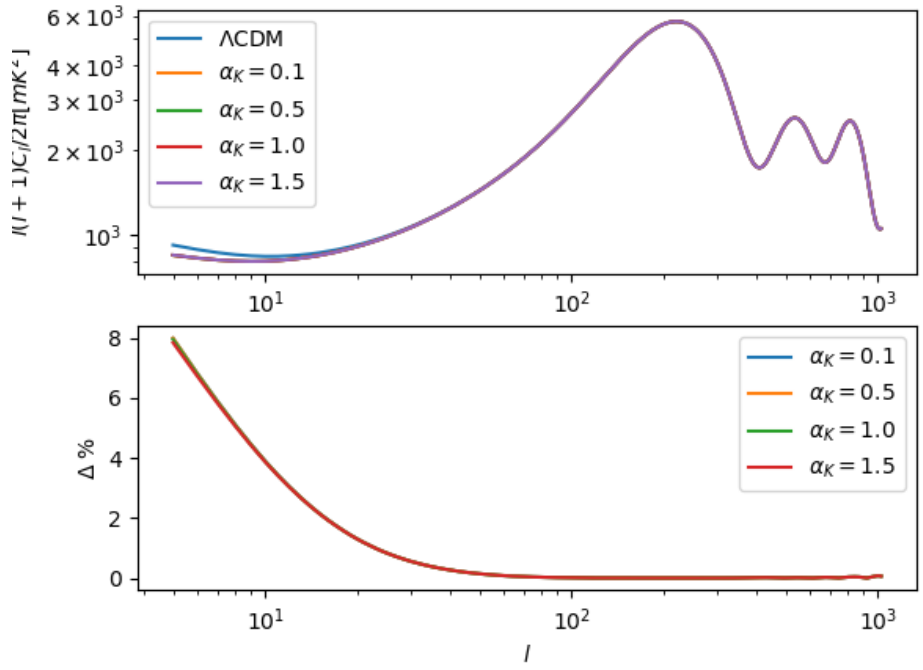

Figure 18 – Effect of the kineticity on CMB temperature angular power spectra.

In the following sections, we show parameter constraints for the α_i parameterizations (2.64) and (2.65), considering first the 21-cm signal only, later the constraints from theoretical CMB likelihood, and finally the combination of 21-cm signal with CMB. Contours mark 1σ

and 2σ confidence level (CL), with all constraints assuming $\alpha_T = 0$. The departures from GR with $c_T \neq c$ will be considered in Sec. 5.4.

5.1 BINGO

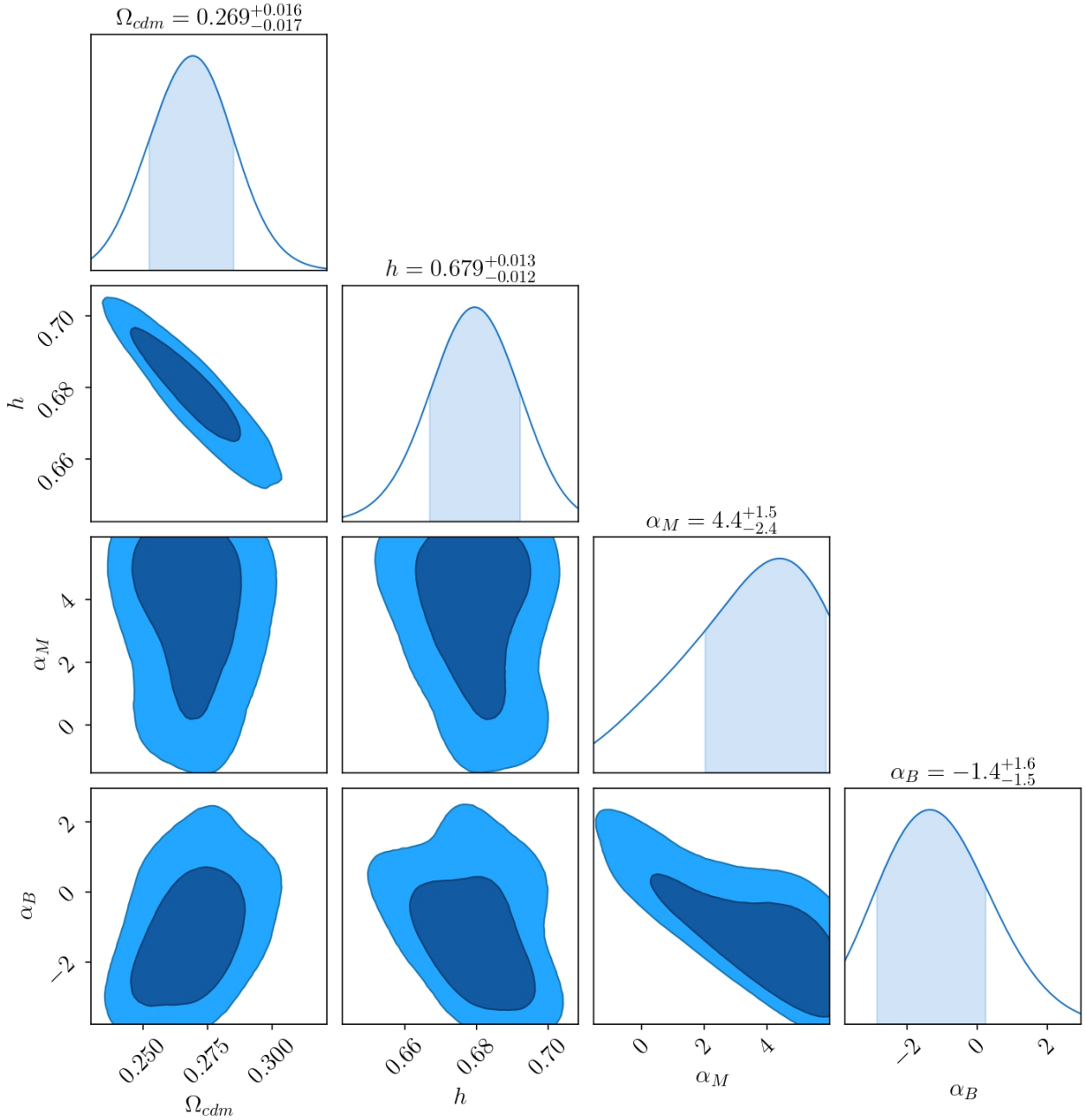

Figure 19 – Cosmological parameter constraints from BINGO using the $\alpha_i \propto \Omega_{DE}$ parameterization.

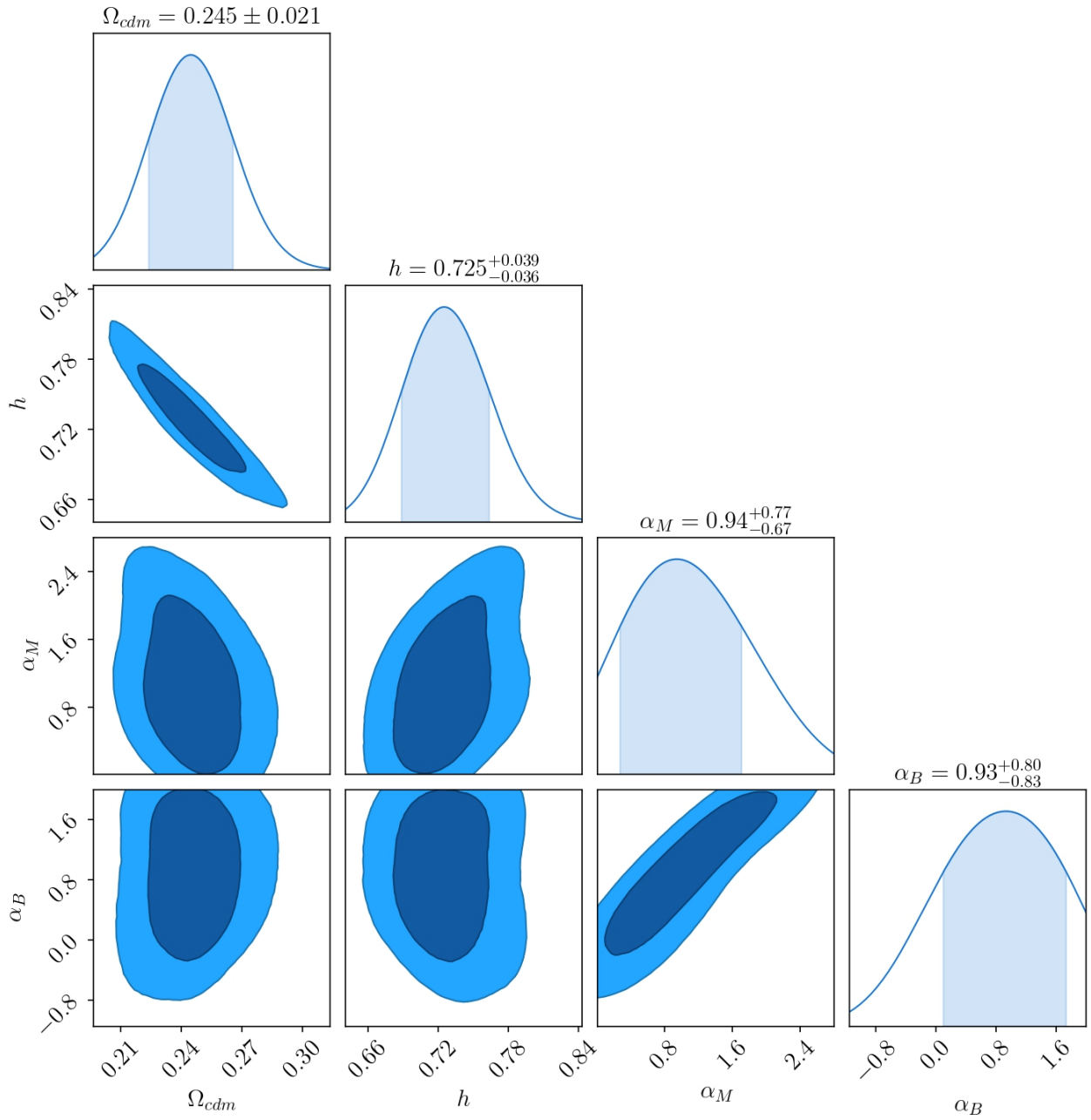

Figure 20 – Cosmological parameter constraints from BINGO using the $\alpha_i \propto a$ parameterization.

5.2 CMB

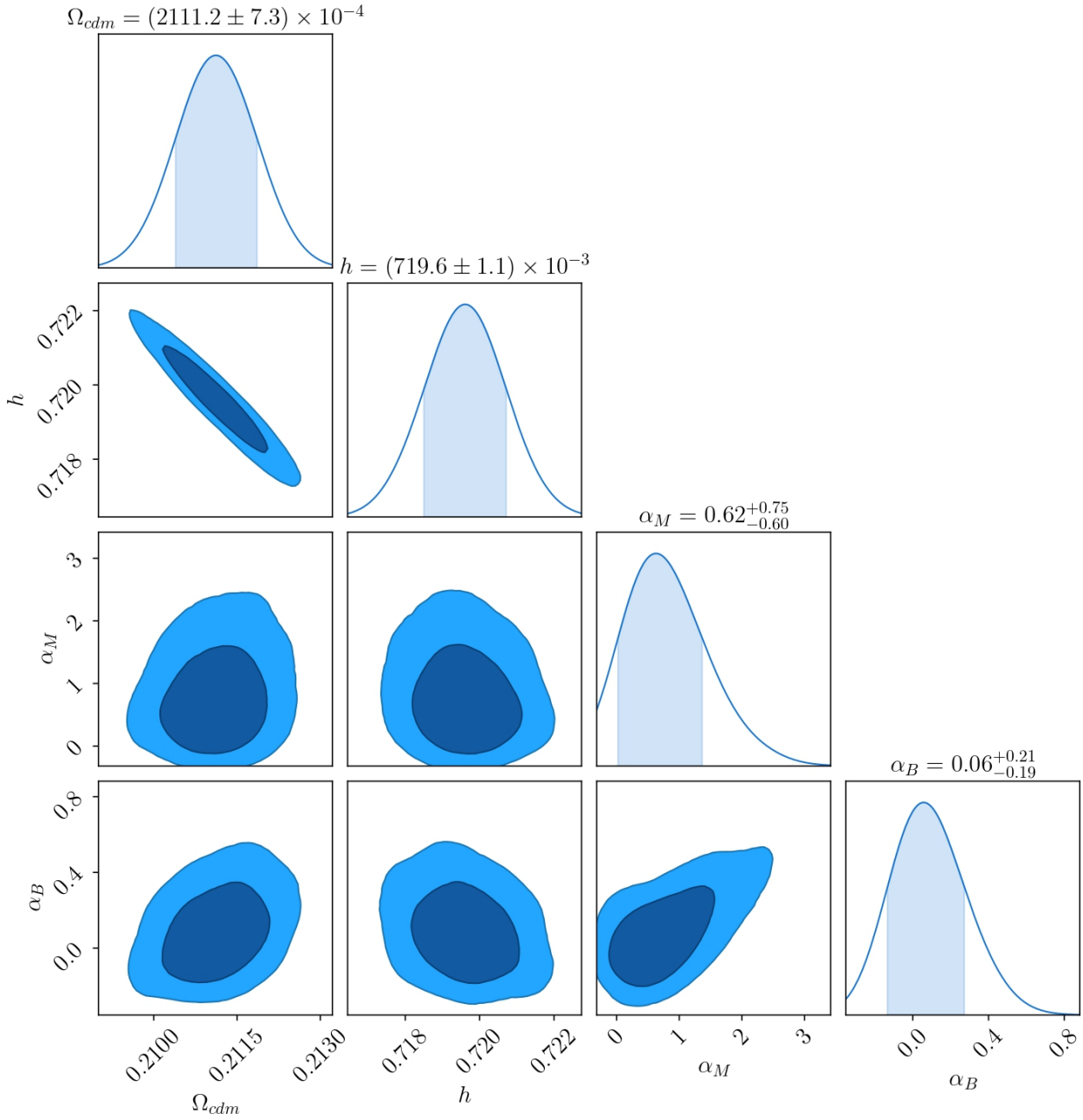

Figure 21 – Cosmological parameter constraints from the CMB data using the $\alpha_i \propto \Omega_{DE}$ parameterization.

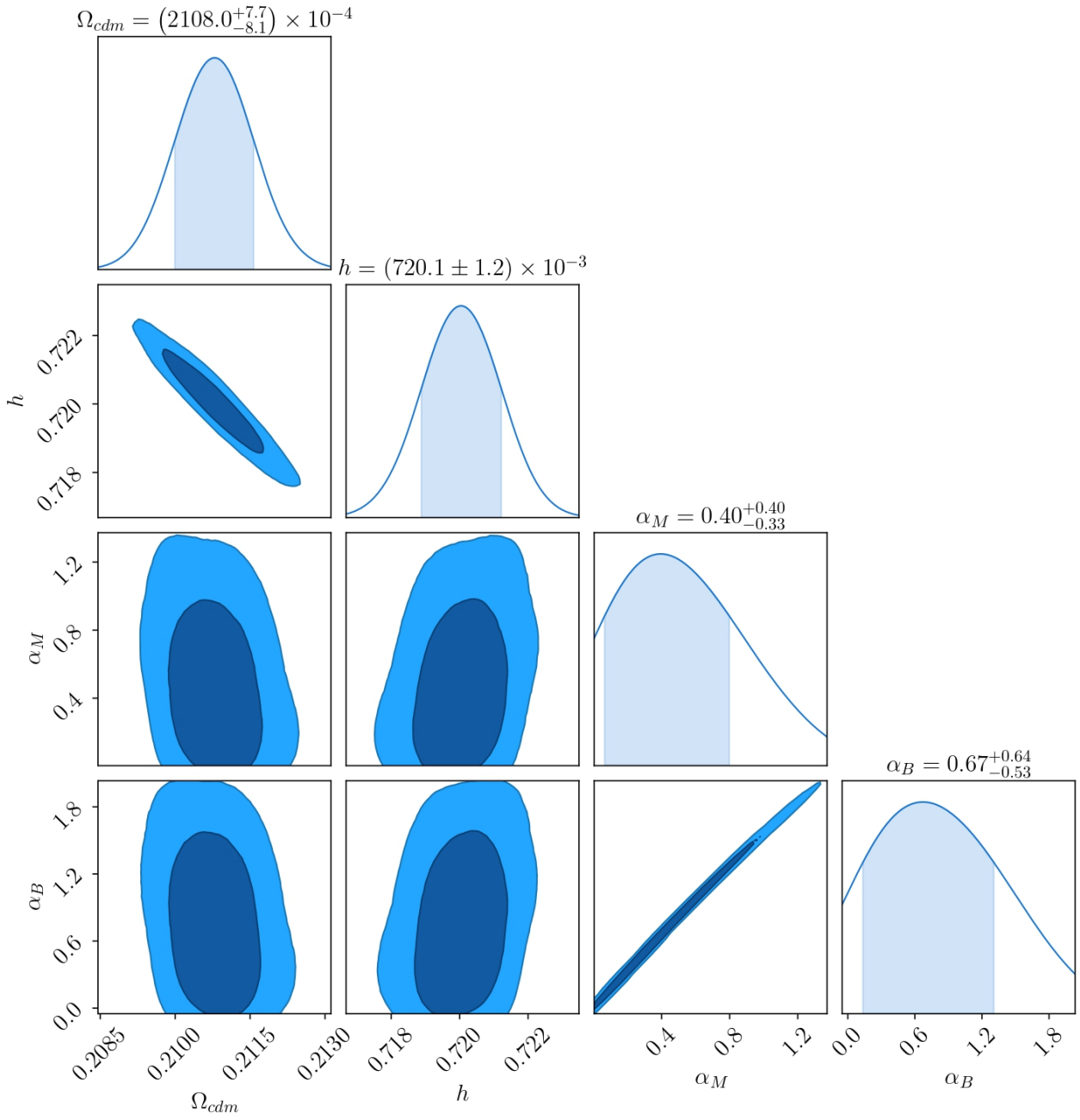

Figure 22 – Cosmological parameter constraints from the CMB data using the $\alpha_i \propto a$ parameterization.

5.3 BINGO+CMB

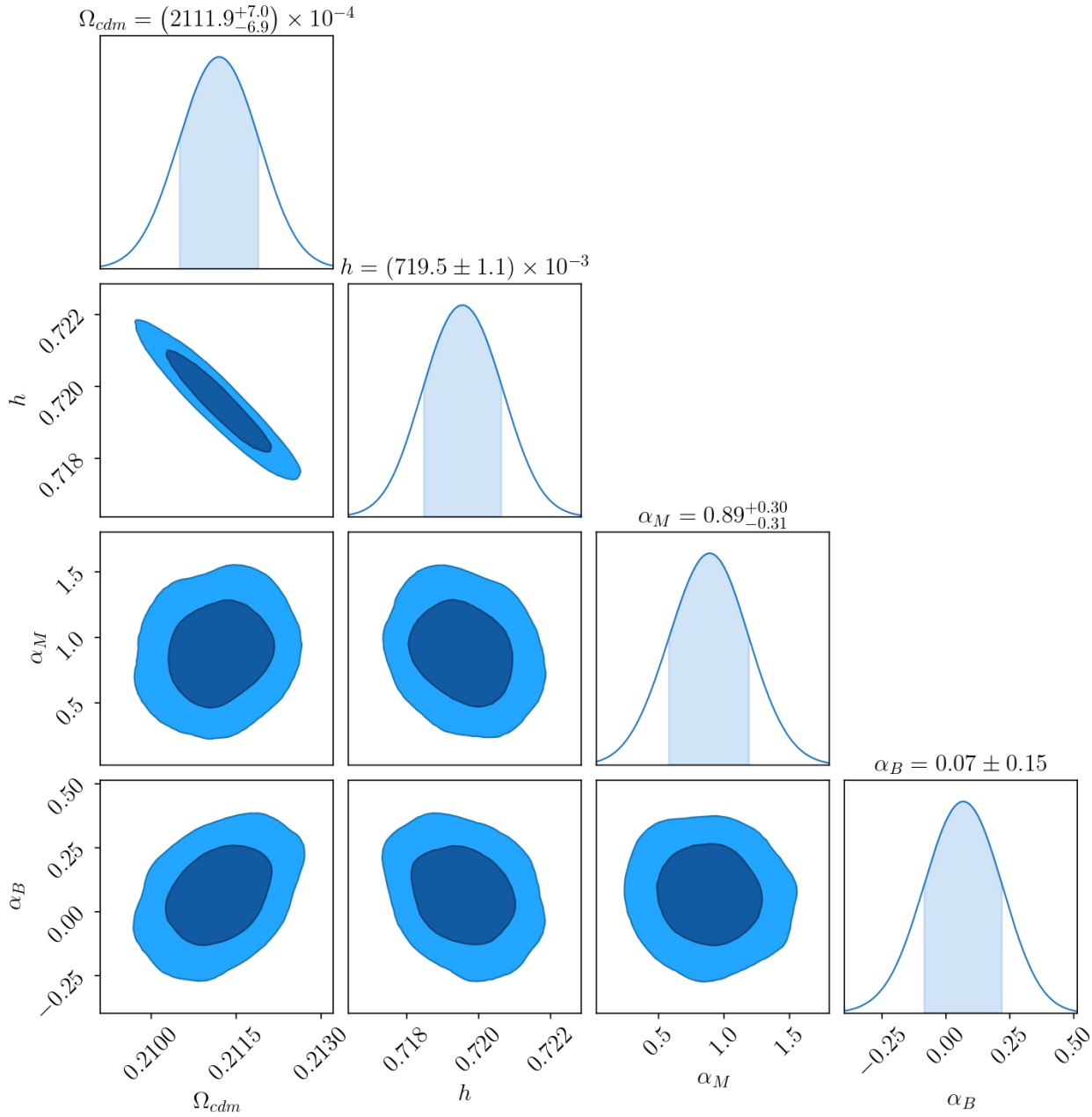

Figure 23 – Cosmological parameter constraints from the combination of BINGO with CMB using the $\alpha_i \propto \Omega_{DE}$ parameterization.

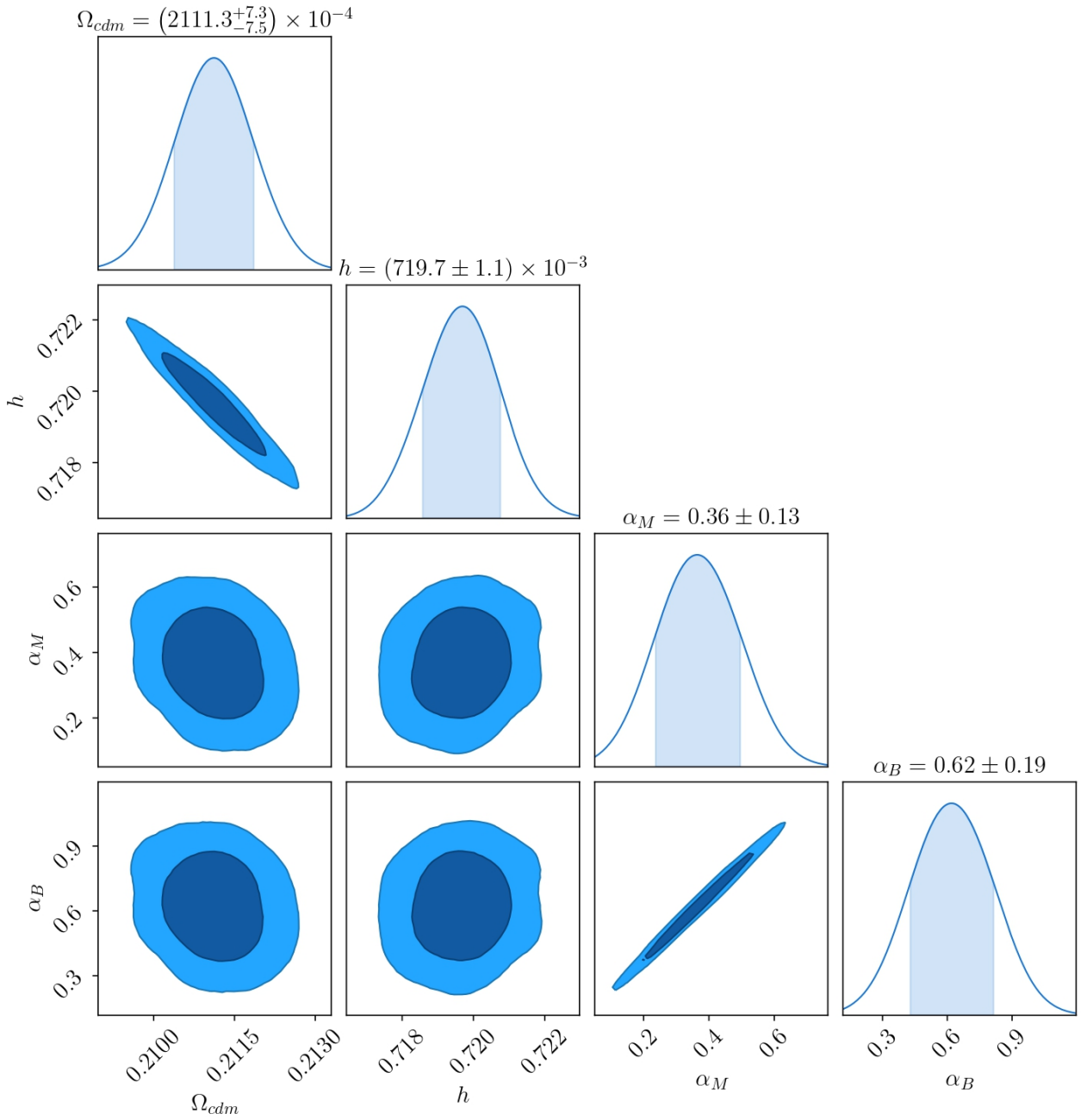

Figure 24 – Cosmological parameter constraints from the combination of BINGO with CMB using the $\alpha_i \propto a$ parameterization.

From the plots of Fig.s 19 and 20, we may notice that, for the 21-cm signal alone, the Ω_{cdm} parameter is not compatible with the fiducial value from WMAP5, considering both parameterizations; h is compatible within 1σ for $\alpha_i \propto a$. The reason for these discrepant values from WMAP5 can be explained by the bias assumed in generating the BINGO maps, which is affected by the way of the HI gas occupation is populated. In fact, the bias is highly sensitive to the method of populating HI in halos, as shown by [16], presenting a small difference from the Halo Occupation Distribution (HOD) mock to the Halo Abundance

Matching (HAM) mock. The generation of more realistic HI maps is in progress under BINGO collaboration; we have used the latest data available. Such disagreement could be solved by computing the b_{HI} directly from FLASK. Beside this, comparing the parameter space involving the MG parameters, we can see that, in general, the 21-cm signal does not favour large departures from GR. The values of α_M and α_B, for the $\alpha_i \propto a$ parameterization, are smaller than those arising from the $\alpha_i \propto \Omega_{DE}$ case: the lower (small α_M) boundary of the contours in the latter is due to the onset of gradient instabilities (Eq. 2.33); also, we see that the contours cross the singular point $\alpha_B = 2$ coming from the sound speed of scalar perturbations (Eq. 2.32). Finally, for both parameterizations, the contour in the $\alpha_M - \alpha_B$ plane suggests a "degeneracy direction" on their measurements.

The plots of Fig.s 21 and 22 show the constraints from theoretical CMB likelihood. As HIR4 simulations were constructed considering the WMAP5 cosmology, then in order to be consistent with those mocks we use a likelihood function built by using a modelling of the CMB thermal noise [162], also set up to the WMAP5 experiment. As we can see, the CMB data place a stronger constrain on the parameters: we recovered the WMAP5 fiducial values of Ω_{cdm} and h for both parameterizations; the MG parameters decrease to a 10^{-1} order; negative α_M values are now ruled out. Combining the data, we get even more accurate estimates. Fig.s 23 and 24 show the parameter constraints for BINGO+CMB. Although the contours are smoother, the MG parameter measurements differ for the two parameterizations: on the one hand, for the $\alpha_i \propto \Omega_{DE}$ case, α_M and α_B values are slightly increased, while on the other hand, for the $\alpha_i \propto a$ case, departures from GR are even smaller. As mentioned before, the results for $\alpha_i \propto a$ parameterization (Fig. 24) confirm a "degeneracy direction" in the $\alpha_M - \alpha_B$ plane. In Fig. 25 we summarize the α_M, α_B constraints from the dataset used here. Table 5 provides the 1σ CL for the cosmological parameters corresponding to the plots of Fig.s 19-24.

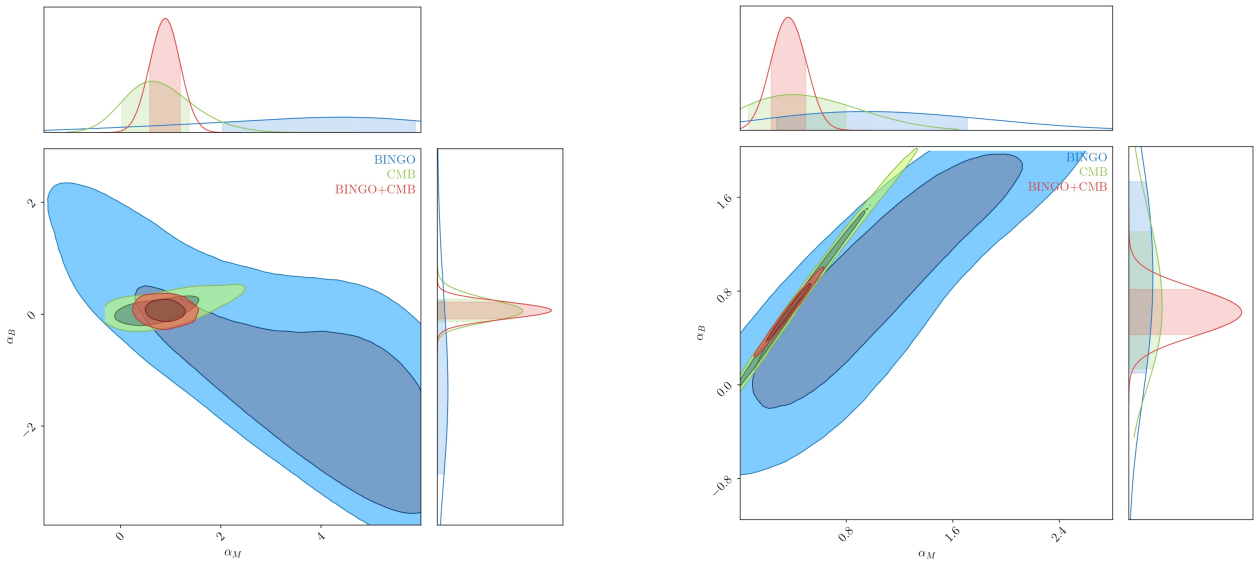

$\alpha_i \propto \Omega_{DE}$ $\alpha_i \propto a$

Figure 25 – Cosmological parameter constraints for the MG parameters α_M and α_B, using the $\alpha_i \propto \Omega_{DE}$ (left triangle plot) and $\alpha_i \propto a$ (right triangle plot) parameterizations and different combinations of datasets and priors.

Table 4 – Recovered parameters from the Monte Carlo analysis with 1σ CL for the $\alpha_i \propto \Omega_{DE}$ parameterization, corresponding to the plots of Fig.s 19, 21 and 23.

Parameter	$\alpha_i \propto \Omega_{DE}$		
	BINGO	CMB	BINGO+CMB
Ω_{cdm}	$0.269^{+0.016}_{-0.017}$	$(2111.2 \pm 7.3) \times 10^{-4}$	$\left(2111.9^{+7.0}_{-6.9}\right) \times 10^{-4}$
h	$0.679^{+0.013}_{-0.012}$	$(719.6 \pm 1.1) \times 10^{-3}$	$(719.5 \pm 1.1) \times 10^{-3}$
α_M	$4.4^{+1.5}_{-2.4}$	$0.62^{+0.75}_{-0.60}$	$0.89^{+0.30}_{-0.31}$
α_B	$-1.4^{+1.6}_{-1.5}$	$0.06^{+0.21}_{-0.19}$	0.07 ± 0.15

Table 5 – Recovered parameters from the Monte Carlo analysis with 1σ CL for the $\alpha_i \propto a$ parameterization corresponding to the plots of Fig.s 20, 22 and 24.

Parameter	$\alpha_i \propto a$		
	BINGO	CMB	BINGO+CMB
Ω_{cdm}	0.245 ± 0.021	$\left(2108.0^{+7.7}_{-8.1}\right) \times 10^{-4}$	$\left(2111.3^{+7.3}_{-7.5}\right) \times 10^{-4}$
h	$0.725^{+0.039}_{-0.036}$	$(720.1 \pm 1.2) \times 10^{-3}$	$(719.7 \pm 1.1) \times 10^{-3}$
α_M	$0.94^{+0.77}_{-0.67}$	$0.40^{+0.40}_{-0.33}$	0.36 ± 0.13
α_B	$0.93^{+0.80}_{-0.83}$	$0.67^{+0.64}_{-0.53}$	0.62 ± 0.19

5.4 Restoring $c_T \neq c$

We end up the discussions about parameter constraints by comparing in this section the manifested effect on the parameter space of allowing α_T to vary. As discussed in Sec. 2.1.4, there exist a large separation in the energy scales of cosmology and those probed by LIGO in determining the sound speed of GWs. This fact, among others mentioned in that section, motivates the exploration of cosmological bounds when $c_T \neq c$. Fig.s 26 and 27 show the constraints considering a varying α_T.

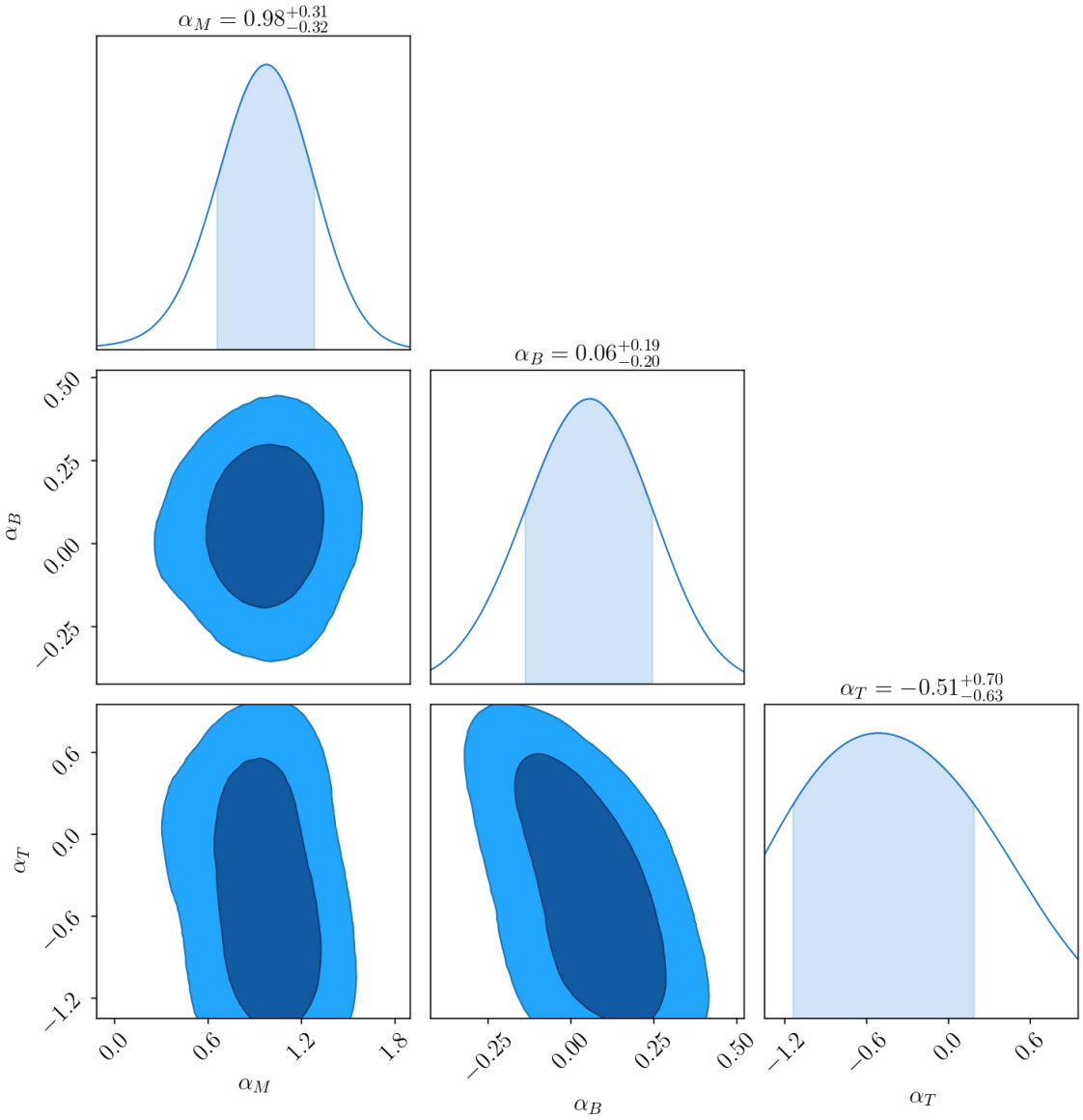

Figure 26 – Cosmological parameter constraints from BINGO+CMB data considering a varying α_T and using the $\alpha_i \propto \Omega_{DE}$ parameterization.

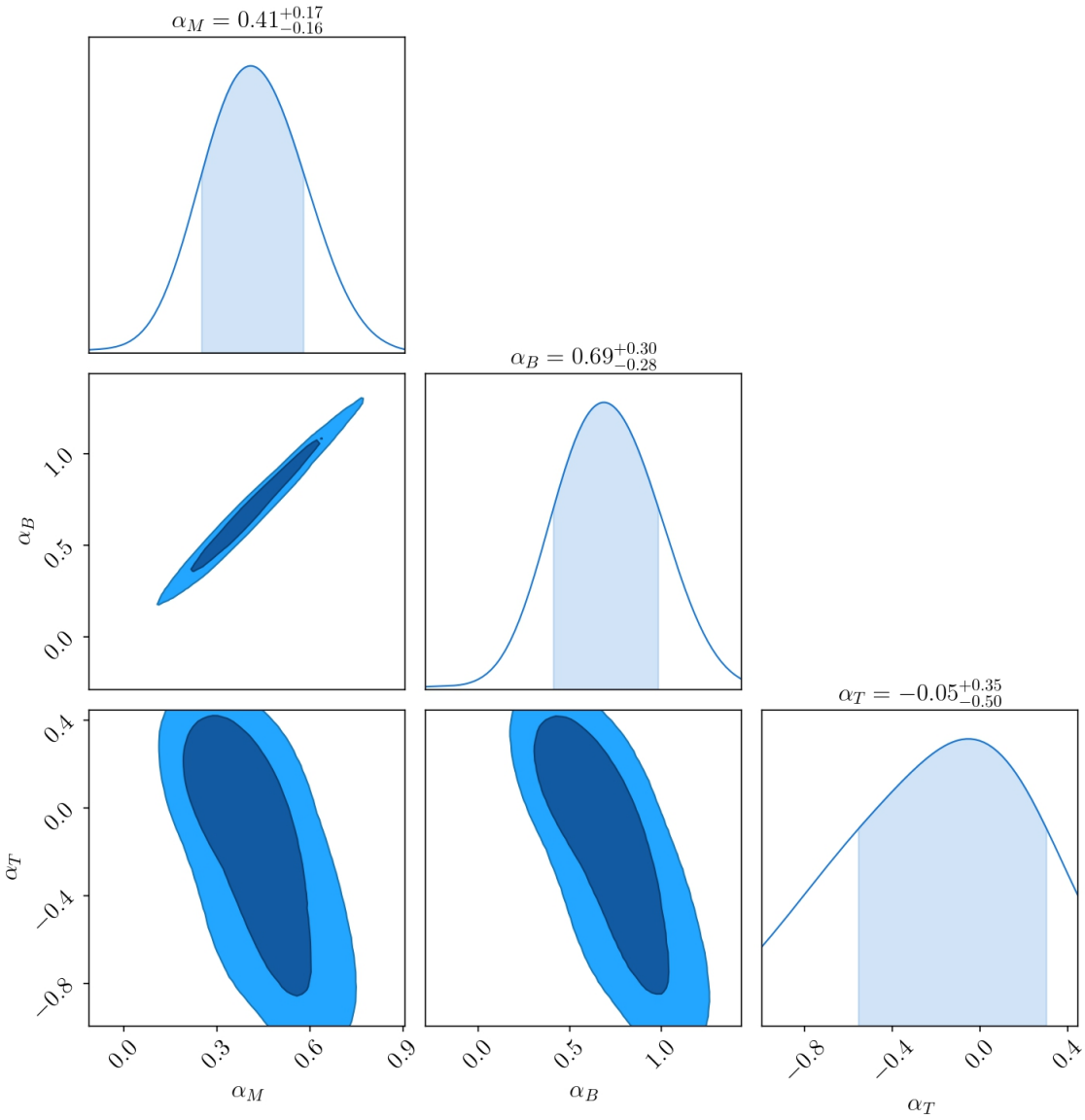

Figure 27 – Cosmological parameter constraints from BINGO+CMB data considering a varying α_T and using the $\alpha_i \propto a$ parameterization.

First of all, we notice a preference for sub-luminal (negative values) propagation of GWs. Such a preference from the data agrees with the theoretical observation that the UV completion from the correspondent EFT rules out superluminal speeds for the propagation of tensor or scalar perturbations [163]. Also, as shown in Fig. 28, the contours in the $\alpha_M - \alpha_B$ plane are mildly changed from the $\alpha_T = 0$ case. Such difference is due to the fact of a non-vanishing α_T affects the onset of gradient instabilities (Eq. 2.32), allowing cosmologies with small negative α_M. Table 6 contains the constraints for the parameters.

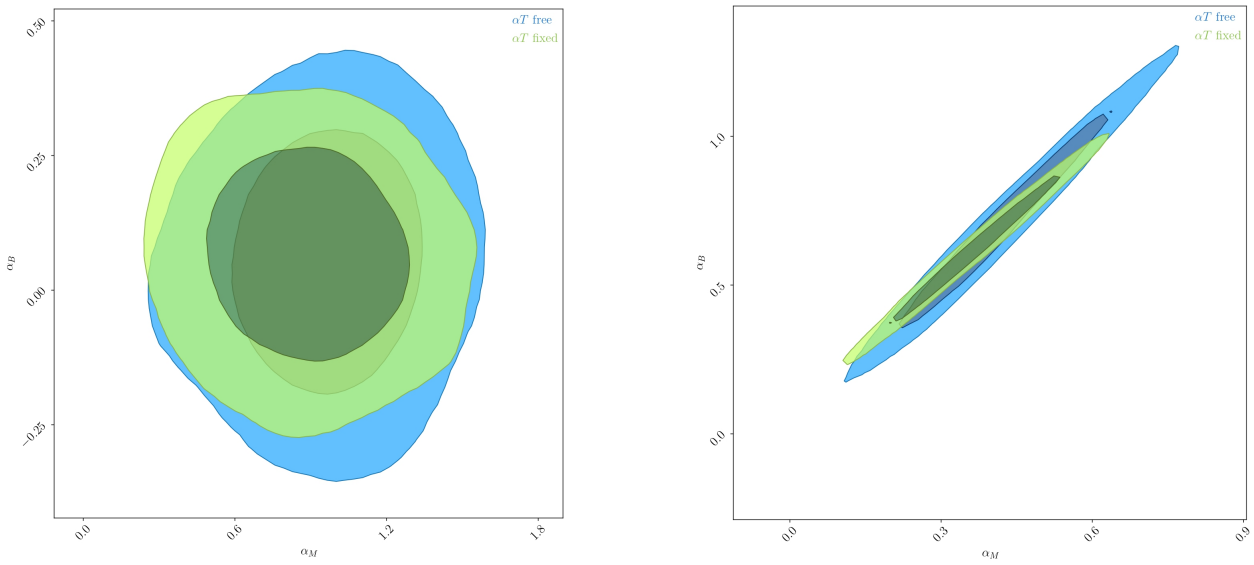

$\alpha_i \propto \Omega_{DE}$ $\alpha_i \propto a$

Figure 28 – Comparison of constraints for α_M and α_B contrasting the case of a fixed luminal speed of GWs vs. the analogous constraints when that speed is allowed to vary for the different parameterizations. Here we used the BINGO+CMB dataset.

Table 6 – Cosmological parameter constraints for the MG parameters α_M and α_B, considering a luminally propagating GWs and the case when α_T is allowed to vary. The values correspond to the plot of Fig. 28.

Parameter	$\alpha_i \propto \Omega_{DE}$		$\alpha_i \propto a$	
	α_T-fixed	α_T-free	α_T-fixed	α_T-free
α_M	$0.89^{+0.30}_{-0.31}$	$0.98^{+0.31}_{-0.32}$	0.36 ± 0.13	$0.41^{+0.17}_{-0.16}$
α_B	0.07 ± 0.15	$0.06^{+0.19}_{-0.20}$	0.62 ± 0.19	$0.69^{+0.30}_{-0.28}$
α_T	$-0.51^{+0.70}_{-0.63}$		$-0.05^{+0.35}_{-0.50}$	

6 Conclusions & Perspectives

In this dissertation, we studied the Horndeski theories, the most general modification to GR that aims to explain the recent accelerated expansion of the universe. We forecast constraints on cosmological parameters using the 21-cm signal from BINGO survey and CMB data. Planned to start to operate in the near future, BINGO is a radiotelescope that will map the distribution of HI in the sky, using a technique called intensity mapping. We used N-body simulations HIR4 and FLASK code to mimic the BINGO data: from HIR4 we extracted the bias and the density parameter of HI, and accounting for the measurement uncertainties by building the covariance matrix from lognormal random distribution, computed by FLASK. The parameters associated to Horndeski gravity were obtained from Markov Monte Carlo processes by employing a nested sampling algorithm.

To extract cosmological parameter constraints, we choose two phenomenological parameterizations for the four α_i functions of the scalar field, arising from second-order linear perturbations of Horndeski action: one proportional to the dark energy density, and the other one proportional to the scale factor − the GR/ΛCDM limit is recovered when all α_i parameters tend to zero. Given the recent measurements of the speed of GWs from GW170817, which stated $c_T = c$ at the energy scale 10^{-13} eV, we initially focused on placed constraints on Horndeski gravity with luminally propagating GWs. When using the 21-cm signal, in general, for the two α_i parameterizations, we have not found a significant deviation from GR, which shows that BINGO experiment has the potential to constrain non-standard cosmology scenarios, such as Horndeski theories. The measurements with CMB data provide more precise/accurate parameters: large values of the MG parameters are ruled out, being reduced to 10^{-1} order. The measurements from the combined BINGO+CMB dataset show even stronger constraints on the parameter, with the α_M and α_B values are smaller for $\alpha_i \propto a$ parameterization than for the $\alpha_i \propto \Omega_{DE}$ case. Pondering about measurements with a varying α_T, the data favour a sub-luminal propagating GWs, according to theoretical predictions, and allows mildly α_M negative values due to gradient instabilities, manifested on lower boundaries for the contours in the $\alpha_M - \alpha_B$ plane.

The BINGO maps are in continuous development; in this work we have used the most recent data provided by the team's collaborators, with the covariance matrix computed by FLASK, assuming constant values for HI bias. Looking ahead, when more realistic mock maps become available it will be possible to obtain better estimates of b_{HI}, and to measure the covariance matrix, improving the constraints presented here. Possible extensions of this work can be made by using complementary data combined with theoretical constraints. On the

observational front, departures from GR can be tested by determining the expansion history through BAO measurements; also, since RSD measures the combination $f\sigma_8$, probing the growth of structures, its use is of special interest in constrain Horndeski theories, and their subclasses. On theoretical front, observational bounds can be increased by reducing the inherent functional freedom of Horndeski gravity. For instance, requiring the constraint $\alpha_M = -\alpha_B$ suppress the possibility of gradient and ghost instabilities coming from the sound speed of scalar perturbations. Also, the synergy between BINGO and other future experiments such as SKA, CMB-S4 and DESI can be explored by using their adopted α-basis parameterization to forecast Horndeski gravity, which takes into account the assumption for screening on small scales [164]. To do that it becomes necessary to implement the EFTCAMB code [165] in the UCLC_l library. In conclusion, we must take care in draw interpretations about Horndeski theories without considering complementary dataset and additional theoretical insights in our analysis. Although the results presented here, whether or not the GR is the final answer remains an open question.

APPENDIX A – Detail calculation

A.1 Einstein Field Equations from Action Approach

The Einstein-Hilbert action is

$$S_{EH} = \int d^4x\sqrt{-g}R. \tag{A.1}$$

Looking at $g^{\mu\nu}$ as an independent dynamical variable, the variation of (A.1) with respect to this quantity is

$$\begin{aligned} \delta S_{EH} &= \delta \int d^4x\sqrt{-g}R \\ &= \int d^4x\delta\left(\sqrt{-g}R\right) \\ &= \int d^4x\sqrt{-g}R_{\mu\nu}\delta g^{\mu\nu} + \int d^4xR\delta\sqrt{-g} + \int d^4x\sqrt{-g}g^{\mu\nu}\delta R_{\mu\nu}. \end{aligned} \tag{A.2}$$

We have three terms of the variation

$$\delta S_{EH} = \delta S_{EH(1)} + \delta S_{EH(2)} + \delta S_{EH(3)}. \tag{A.3}$$

The second term is

$$\delta S_{EH(2)} = \int d^4xR\delta\sqrt{-g}. \tag{A.4}$$

The variation of the determinant is

$$\delta\sqrt{-g} = \frac{-1}{2\sqrt{-g}}\delta g. \tag{A.5}$$

Assuming that $g_{\mu\nu}$ is symmetric, we have $g_{\mu\rho}g^{\rho\nu} = \delta^{\nu}_{\mu}$. So, the inverse of the $g_{\mu\nu}$ is

$$g^{\mu\nu} = \frac{1}{det g_{\mu\nu}}\left(A^{\mu\nu}\right)^T = \frac{1}{g}A^{\nu\mu}, \tag{A.6}$$

where $g \equiv det(g_{\mu\nu})$ and $A^{\nu\mu}$ is the matrix of cofactors from the metric $g_{\mu\nu}$. Solving for the determinant, we get

$$g = g_{\mu\nu}A^{\nu\mu}. \tag{A.7}$$

Performing partial differentiation on both sides of the Eq. (A.7) with respect to $g_{\mu\nu}$ we get

$$\frac{\partial g}{\partial g_{\mu\nu}} = A^{\nu\mu}. \tag{A.8}$$

Considering variation of the Eq. (*A.7*) with respect to $g_{\mu\nu}$, we conclude that

$$\delta g = \frac{\partial g}{\partial g_{\mu\nu}}\delta g_{\mu\nu} = A^{\nu\mu}\delta g_{\mu\nu} = g g^{\mu\nu}\delta g_{\mu\nu}. \tag{A.9}$$

Then, using the result in Eq. (*A.9*)

$$\delta g^{\rho\sigma} = -g^{\mu\rho}g^{\nu\sigma}\delta g_{\mu\nu}, \tag{A.10}$$

the Eq. (*A.5*) is written as

$$\delta\sqrt{-g} = -\frac{1}{2}\sqrt{-g}g_{\mu\nu}\delta g^{\mu\nu}, \tag{A.11}$$

and then the variation given by Eq. (*A.4*) becomes

$$\delta S_{EH(2)} = -\frac{1}{2}\int d^4x\sqrt{-g}R g_{\mu\nu}\delta g^{\mu\nu}. \tag{A.12}$$

The third variation is

$$\delta S_{EH(3)} = \int d^4x\sqrt{-g}g^{\mu\nu}\delta R_{\mu\nu}. \tag{A.13}$$

The variation of the Ricci tensor is

$$\begin{aligned}
\delta R_{\mu\nu} &= \partial_\alpha\delta\Gamma^\alpha_{\mu\nu} - \partial_\nu\delta\Gamma^\alpha_{\mu\alpha} + \Gamma^\beta_{\nu\mu}\delta\Gamma^\alpha_{\alpha\beta} + \Gamma^\alpha_{\alpha\beta}\delta\Gamma^\beta_{\nu\mu} - \Gamma^\beta_{\mu\alpha}\delta\Gamma^\alpha_{\nu\beta} - \Gamma^\alpha_{\nu\beta}\delta\Gamma^\beta_{\mu\alpha} \\
&= \left(\partial_\alpha\delta\Gamma^\alpha_{\mu\nu} + \Gamma^\alpha_{\alpha\beta}\delta\Gamma^\beta_{\nu\mu} - \Gamma^\beta_{\mu\alpha}\delta\Gamma^\alpha_{\nu\beta} - \Gamma^\beta_{\nu\alpha}\delta\Gamma^\alpha_{\mu\beta}\right) \\
&- \left(\partial_\nu\delta\Gamma^\alpha_{\mu\alpha} + \Gamma^\alpha_{\nu\beta}\delta\Gamma^\beta_{\mu\alpha} + \Gamma^\beta_{\nu\mu}\delta\Gamma^\alpha_{\alpha\beta} - \Gamma^\beta_{\nu\alpha}\delta\Gamma^\alpha_{\mu\beta}\right).
\end{aligned} \tag{A.14}$$

The covariant derivative formula gives

$$\nabla_\alpha\delta\Gamma^\alpha_{\mu\nu} = \partial_\alpha\delta\Gamma^\alpha_{\mu\nu} + \Gamma^\alpha_{\alpha\beta}\delta\Gamma^\beta_{\nu\mu} - \Gamma^\beta_{\mu\alpha}\delta\Gamma^\alpha_{\nu\beta} - \Gamma^\beta_{\nu\alpha}\delta\Gamma^\alpha_{\mu\beta}, \tag{A.15}$$

and

$$\nabla_\nu\delta\Gamma^\alpha_{\mu\alpha} = \partial_\nu\delta\Gamma^\alpha_{\mu\alpha} + \Gamma^\alpha_{\nu\beta}\delta\Gamma^\beta_{\mu\alpha} + \Gamma^\beta_{\nu\mu}\delta\Gamma^\alpha_{\alpha\beta} - \Gamma^\beta_{\nu\alpha}\delta\Gamma^\alpha_{\mu\beta}. \tag{A.16}$$

Then, we conclude that

$$\delta R_{\mu\nu} = \nabla_\alpha\delta\Gamma^\alpha_{\mu\nu} - \nabla_\nu\delta\Gamma^\alpha_{\mu\alpha}. \tag{A.17}$$

So,

$$\begin{aligned}
g^{\mu\nu}\delta R_{\mu\nu} &= g^{\mu\nu}\left(\nabla_\alpha\delta\Gamma^\alpha_{\mu\nu} - \nabla_\nu\delta\Gamma^\alpha_{\mu\alpha}\right) \\
&= \nabla_\alpha\left(g^{\mu\nu}\delta\Gamma^\alpha_{\mu\nu}\right) - \delta\Gamma^\alpha_{\mu\nu}\nabla_\alpha g^{\mu\nu} - \nabla_\nu\left(g^{\mu\nu}\delta\Gamma^\alpha_{\mu\alpha}\right) + \delta\Gamma^\alpha_{\mu\alpha}\nabla_\nu g^{\mu\nu} \\
&= \nabla_\alpha\left(g^{\mu\nu}\delta\Gamma^\alpha_{\mu\nu}\right) - \nabla_\nu\left(g^{\mu\nu}\delta\Gamma^\alpha_{\mu\alpha}\right) \\
&= \nabla_\alpha\left(g^{\mu\nu}\delta\Gamma^\alpha_{\mu\nu} - g^{\mu\alpha}\delta\Gamma^\nu_{\mu\nu}\right) \\
&= \nabla_\alpha J^\alpha,
\end{aligned} \tag{A.18}$$

where $J^\alpha \equiv g^{\mu\nu}\delta\Gamma^\alpha_{\mu\nu} - g^{\mu\alpha}\delta\Gamma^\nu_{\mu\nu}$ represents the *4-gravitational current*.

Interpreting J^α as a vector field over the volume $\mathcal{V}$ and boundary Ω, then the Stokes' theorem gives

$$\int_{\mathcal{V}} d^4x\sqrt{|g|}\nabla_\alpha J^\alpha = \int_\Omega d^3x\sqrt{|h|}n_\alpha J^\alpha, \tag{A.19}$$

where n_α is a normal unity vector on hypersurface Ω. This vector can be normalized as $n_\mu n^\mu = -1$. The tensor $h_{\mu\nu}$ is the induced metric associated with hypersurface, defined by

$$h_{\mu\nu} = g_{\mu\nu} + n_\mu n_\nu. \tag{A.20}$$

The contribution of the vector field J^α on boundary Ω, located at the infinity, can be set to zero. Therefore, the variation given by Eq. (A.13) vanish at this limit, and contributes nothing to the Einstein-Hilbert action

$$\delta S_{EH(3)} = \int_\Omega d^3x\sqrt{|h|}n_\alpha J^\alpha = 0. \tag{A.21}$$

Using the results from Eq. (A.12) and Eq. (A.21), the Eq. (A.3) becomes

$$\delta S_{EH} = \int d^4x\sqrt{-g}\left(R_{\mu\nu} - \frac{1}{2}Rg_{\mu\nu}\right)\delta g^{\mu\nu}. \tag{A.22}$$

Finally, from the principle of least action, the Einstein field equations in vacuum read

$$R_{\mu\nu} - \frac{1}{2}Rg_{\mu\nu} = 0. \tag{A.23}$$

A.2 $I_\pm(x)$ and $J_\pm(x)$ Integrals

The following formulas will be useful:

$$\int_0^\infty dy\frac{y^n}{e^y - 1} = \zeta(n+1)\Gamma(n+1) \qquad \textit{and} \qquad \int_0^\infty dy\frac{y^n}{e^y} = \frac{1}{2}\Gamma\left[\frac{1}{2}(n+1)\right], \tag{A.24}$$

where $\zeta(z)$ is the Riemann-zeta function, and $\Gamma(z)$ is the gamma function.

(i) Relativistic limit $(x \ll 1)$

$$I_\pm(x \ll 1) \approx I_\pm(0) = \int_0^\infty dy\frac{y^2}{e^y \pm 1}. \tag{A.25}$$

For bosons we use the first formula of Eq. (A.24)

$$I_-(0) = \zeta(3)\Gamma(3) = 2\zeta(3). \tag{A.26}$$

For fermions we make use of the following trick:

$$\frac{1}{e^y + 1} = \frac{1}{e^y - 1} - 2\frac{1}{e^{2y} - 1}. \tag{A.27}$$

Then, we can write

$$\begin{aligned} I_+(0) &= \int_0^\infty dy \frac{y^2}{e^y+1} = I_-(0) - 2\int_0^\infty dy \frac{y^2}{e^{2y}-1} = I_-(0) - 2\left(\frac{1}{2}\right)^3 I_-(0) = \frac{3}{4} I_-(0) \\ &= \frac{3}{2}\zeta(3). \end{aligned} \tag{A.28}$$

Therefore,

$$I_\pm(0) = \zeta(3) \times \begin{cases} 2 & \text{bosons} \\ \frac{3}{2} & \text{fermions} \end{cases}. \tag{A.29}$$

Similarly, we have

$$J_-(0) = \zeta(4)\Gamma(4) = \frac{\pi^4}{15}, \tag{A.30}$$

and

$$J_+(0) = \left[1 - 2\left(\frac{1}{2}\right)^4\right] J_-(0) = \frac{7}{8} J_-(0), \tag{A.31}$$

and so

$$J_\pm(0) = \frac{\pi^4}{15} \times \begin{cases} 1 & \text{bosons} \\ \frac{7}{8} & \text{fermions} \end{cases}. \tag{A.32}$$

(ii) Non-relativistic limit ($x \gg 1$)

$$\begin{aligned} I_\pm(x \gg 1) &= \int_0^\infty dy \frac{y^2}{e^{\sqrt{x^2+y^2}} \pm 1} \approx \int_0^\infty dy \frac{y^2}{e^{\sqrt{x^2+y^2}}} \approx \int_0^\infty dy \frac{y^2}{e^{x+y^2/2x}} \\ &= e^{-x}\int_0^\infty dy y^2 e^{-y^2/2x} = e^{-x}\sqrt{\frac{\pi}{2}} x^{3/2}. \end{aligned} \tag{A.33}$$

On the other hand,

$$\begin{aligned} J_\pm(x \gg 1) &= \int_0^\infty dy \frac{y^2\sqrt{x^2+y^2}}{e^{\sqrt{x^2+y^2}} \pm 1} \approx \int_0^\infty dy \frac{y^2\sqrt{x^2+y^2}}{e^{\sqrt{x^2+y^2}}} \approx \int_0^\infty dy \frac{y^2\,(x+y^2/2x)}{e^{x+y^2/2x}} \\ &\approx e^{-x} x \int_0^\infty dy y^2 e^{-y^2/2x} = x I_\pm(x \gg 1). \end{aligned} \tag{A.34}$$

Bibliography

[1] Riess, A. *et al. Observational Evidence from Supernovae for an Accelerating Universe and a Cosmological Constant.* The Astronomical Journal **116**, 1009-1038 (1998) DOI=http://dx.doi.org/10.1086/300499;

[2] Perlmutter, S. *et al. Measurements of* Ω *and* Λ *from 42 High-Redshift Supernovae.* The Astrophysical Journal **517**, 565-586 (1999) DOI=http://dx.doi.org/10.1086/307221;

[3] Planck Collaboration, *Planck 2013 results. I. Overview of products and scientific results.* Astronomy & Astrophysics **571**, A1 (2014) DOI=https://doi.org/10.1051/0004-6361/201321529;

[4] Eisenstein, D. *et al. Detection of the Baryon Acoustic Peak in the Large-Scale Correlation Function of SDSS Luminous Red Galaxies.* The Astrophysical Journal **633**, 560–574 (2005) DOI=http://dx.doi.org/10.1086/466512;

[5] Begeman, K. *HI rotation curves of spiral galaxies.* PhD Thesis, 134 p. University of Groningen (1987) Address=https://research.rug.nl/en/publications/hi-rotation-curves-of-spiral-galaxies, accessed in Aug/2021;

[6] Riess, A. *et al. Large Magellanic Cloud Cepheid Standards Provide a 1% Foundation for the Determination of the Hubble Constant and Stronger Evidence for Physics beyond* ΛCDM. The Astrophysical Journal **876**, 85 (2019) DOI=http://dx.doi.org/10.3847/1538-4357/ab1422;

[7] Lovelock, D. *The Einstein Tensor and Its Generalizations.* Journal of Mathematical Physics **12**, 498-501 (1971) DOI=https://doi.org/10.1063/1.1665613;

[8] Horndeski, G. *Second-order scalar-tensor field equations in a four-dimensional space.* International Journal of Theoretical Physics **10**, 363-384 (1974) DOI=https://doi.org/10.1007/BF01807638;

[9] Gleyzes, J. *et al. Essential building blocks of dark energy.* Journal of Cosmology and Astroparticle Physics **2013**, 025-025 (2013) DOI=http://dx.doi.org/10.1088/1475-7516/2013/08/025;

[10] Bellini, E. & Sawicki, I. *Maximal freedom at minimum cost: linear large-scale structure in general modifications of gravity.* Journal of Cosmology and Astroparticle Physics **2014**, 050-050 (2014) DOI=http://dx.doi.org/10.1088/1475-7516/2014/07/050;

[11] Abdalla, E. *et al. The BINGO project. I. Baryon acoustic oscillations from integrated neutral gas observations*. Astronomy & Astrophysics DOI=http://dx.doi.org/10.1051/0004-6361/202140883 (2021);

[12] Wuensche, C. *et al. The BINGO Project II: Instrument Description*. arXiv=https://arxiv.org/abs/2107.01634 (2021);

[13] Abdalla, F. *et al. The BINGO Project III: Optical design and optimisation of the focal plane*. arXiv=https://arxiv.org/abs/2107.01635 (2021);

[14] Liccardo, V. *et al. The BINGO project. IV. Simulations for mission performance assessment and preliminary component separation steps*. Astronomy & Astrophysics DOI=http://dx.doi.org/10.1051/0004-6361/202140886 (2021);

[15] Fornazier, K. *et al. The BINGO Project V: Further steps in Component Separation and Bispectrum Analysis*. arXiv=https://arxiv.org/abs/2107.01637 (2021);

[16] Zhang, J. *et al. The BINGO project. VI. Hi halo occupation distribution and mock building*. Astronomy & Astrophysics DOI=http://dx.doi.org/10.1051/0004-6361/202140887 (2021);

[17] Costa, A. *et al. The BINGO Project VII: Cosmological Forecasts from 21-cm Intensity Mapping*. arXiv=https://arxiv.org/abs/2107.01639 (2021);

[18] Xavier, H., Abdalla, F. & Joachimi, B. *Improving lognormal models for cosmological fields*. MNRAS **459**, 3693-3710 (2016) DOI=http://dx.doi.org/10.1093/mnras/stw874;

[19] Slipher, V. *The radial velocity of the Andromeda Nebula*. Lowell Observatory Bulletin **1**, 56-57 (1913) Address=https://ui.adsabs.harvard.edu/abs/1913LowOB...2...56S;

[20] Lemaître, G. *Un Univers homogène de masse constante et de rayon croissant rendant compte de la vitesse radiale des nébuleuses extra-galactiques*. Annales de la Société Scientifique de Bruxelles, **47** 49-59 (1927) Address=https://ui.adsabs.harvard.edu/abs/1927ASSB...47...49L;

[21] Hubble, E. *A relation between distance and radial velocity among extra-galactic nebulae*. Proceedings of the National Academy of Sciences **15**, 168-173 (1929) DOI=http://dx.doi.org/10.1073/pnas.15.3.168;

[22] Leavitt, H. & Pickering, E. *Periods of 25 Variable Stars in the Small Magellanic Cloud*. Harvard College Observatory Circular **173**, 1-3 (1912);

[23] Aghanim, N. *et al. Planck 2018 results*. Astronomy & Astrophysics **641**, A6 (2020) DOI=http://dx.doi.org/10.1051/0004-6361/201833910;

[24] Reid, M., Pesce, D. & Riess, A. *An Improved Distance to NGC 4258 and Its Implications for the Hubble Constant*. The Astrophysical Journal **886**, L27 (2019) DOI=http://dx.doi.org/10.3847/2041-8213/ab552d;

[25] Di Valentino, E. *et al. Snowmass2021 - Letter of interest cosmology intertwined II: The hubble constant tension*. Astroparticle Physics **131**, 102605 (2021) DOI=http://dx.doi.org/10.1016/j.astropartphys.2021.102605;

[26] Hobson, M., Efstathiou, G. & Lasenby, A. *General Relativity: An Introduction for Physicists*. Cambridge Univ. Press (2006);

[27] Fixsen, D. *The Temperature of the Cosmic Microwave Background*. The Astrophysical Journal **707**, 916-920 (2009) DOI=http://dx.doi.org/10.1088/0004-637X/707/2/916;

[28] Blumenthal, G., Pagels, H. & Primack, J. *Galaxy formation by dissipationless particles heavier than neutrinos*. Nature **299**, 37-38 (1982) DOI=https://doi.org/10.1038/299037a0;

[29] Bond, J., Szalay, A. & Turner, M. *Formation of Galaxies in a Gravitino-Dominated Universe*. Physical Review Letters **48**, 1636-1640 (1982) DOI=https://doi.org/10.1103/PhysRevLett.48.1636;

[30] Pagels, H. & Primack, J. *Supersymmetry, cosmology, and new physics at teraelectronvolt energies*. Physical Review Letters **48**, 223-226 (1982) DOI=https://doi.org/10.1103/PhysRevLett.48.223;

[31] Peebles, P. *Primeval adiabatic perturbations - Effect of massive neutrinos*. Astrophysical Journal **258**, 415-424 (1982) DOI=https://doi.org/10.1086/160094;

[32] Bond, J. & Szalay, A. *The collisionless damping of density fluctuations in an expanding universe*. Astrophysical Journal **274**, 443-468 (1983) DOI=https://doi.org/10.1086/161460;

[33] Doroshkevich, A. & Khlopov, M. *Formation of structure in a universe with unstable neutrinos*. MNRAS **211**, 277-282 (1984) DOI=https://doi.org/10.1093/mnras/211.2.277;

[34] Jeans, J. *The Motions of Stars in a Kapteyn-Universe*. MNRAS **82**, 122-132 (1922) DOI=https://doi.org/10.1093/mnras/82.3.122;

[35] Zwicky, F. *Die Rotverschiebung von extragalaktischen Nebeln*. Helvetica Physica Acta **6**, 110-127 (1933) Address=https://ui.adsabs.harvard.edu/abs/1933AcHPh...6..110Z;

[36] Einasto, J. *Dark matter*. [astro-ph.CO] (2010) arXiv=https://arxiv.org/abs/0901.0632;

[37] Kuijken, K. & Gilmore, G. *The mass distribution in the galactic disc − III. The local volume mass density*. MNRAS **239**, 651-664 (1989) DOI=https://doi.org/10.1093/mnras/239.2.651;

[38] Gilmore, G. *et al. Kinematics, chemistry, and structure of the Galaxy*. Annual Rev. Astron. Astrophys. **27**, 555-627 (1989) DOI=https://doi.org/10.1146/annurev.aa.27.090189.003011;

[39] Rubin, V. *et al. Rotational properties of 21 SC galaxies with a large range of luminosities and radii, from NGC 4605 (R = 4kpc) to UGC 2885 (R = 122kpc)*. Astrophysical Journal **238**, 471-487 (1980) DOI=https://doi.org/10.1086/158003;

[40] Forman, W. & Jones, C. *X-ray-imaging observations of clusters of galaxies*. In: Annual review of astronomy and astrophysics **20**, 547-585 (1982) DOI=https://doi.org/10.1146/annurev.aa.20.090182.002555;

[41] Sarazin, C. *X-ray emission from clusters of galaxies*. Cambridge Astrophysics Series, Cambridge: Cambridge University Press (1988) Address=https://ui.adsabs.harvard.edu/abs/1988xrec.book.....S;

[42] Bradač, M. *et al. Strong and weak lensing united - I. The combined strong and weak lensing cluster mass reconstruction method*. Astronomy & Astrophysics **437**, 39-48 (2005) DOI=https://doi.org/10.1051/0004-6361:20042233;

[43] Dietrich, J. *et al. Weak lensing study of dark matter filaments and application to the binary cluster A 222 and A 223*. Astronomy & Astrophysics **440**, 453-471 (2005) DOI=http://dx.doi.org/10.1051/0004-6361:20041523;

[44] Clowe, D. *et al. Weak lensing mass reconstructions of the ESO Distant Cluster Survey*. Astronomy & Astrophysics **451**, 395-408 (2006) DOI=http://dx.doi.org/10.1051/0004-6361:20041787;

[45] Massey, R. *et al. Dark matter maps reveal cosmic scaffolding*. Nature **445**, 286-290 (2007) DOI=https://doi.org/10.1038/nature05497;

[46] Zyla, P. *et al. Review of Particle Physics*. Progress of Theoretical and Experimental Physics **2020**, 083C01 (2020) DOI=https://doi.org/10.1093/ptep/ptaa104;

[47] Taoso, M. *et al. Dark matter candidates: a ten-point test*. Journal of Cosmology and Astroparticle Physics **2008**, 022 (2008) DOI=http://dx.doi.org/10.1088/1475-7516/2008/03/022;

[48] Trevisani, N. *Collider Searches for Dark Matter (ATLAS + CMS)*. Universe **4** (2018) DOI=https://doi.org/10.3390/universe4110131;

[49] Tolley, E. *Dark Matter searches with the ATLAS Detector*. PoS **ICHEP2018**, 171 p. (2019) DOI=https://doi.org/10.22323/1.340.0171;

[50] Kalderon, C. *Dark Matter searches with the ATLAS Detector*. PoS **DIS2018**, 085p. (2018) DOI=https://doi.org/10.22323/1.316.0085;

[51] Vannerom, D. *Dark Matter searches with CMS*. PoS **DIS2019**, 111p. (2019) DOI=https://doi.org/10.22323/1.352.0111;

[52] Gomez-Ceballos, G. *Dark Matter Searches with the CMS Experiment*. PoS **EDSU2018**, 014p. (2018) DOI=https://doi.org/10.22323/1.335.0014;

[53] Schumann, M. *Direct detection of WIMP dark matter: concepts and status*. Journal of Physics G: Nuclear and Particle Physics **46**, 103003 (2019) DOI=https://doi.org/10.1088/1361-6471/ab2ea5;

[54] Bretón, N., Cervantes-Cota, J. & Salgado, M. *The Early Universe and Observational Cosmology*. Springer, Berlin, Heidelberg, 1st Ed., 469p. (2004) DOI=https://doi.org/10.1007/b97189;

[55] Betoule, M. textitet al. *Improved cosmological constraints from a joint analysis of the SDSS-II and SNLS supernova samples*. Astronomy & Astrophysics **568**, A22 (2014) DOI=http://dx.doi.org/10.1051/0004-6361/201423413;

[56] Sotiriou, T. & Faraoni, V. *$f(R)$ theories of gravity*. Reviews of Modern Physics **82**, 451-497 (2010) DOI=https://link.aps.org/doi/10.1103/RevModPhys.82.451;

[57] Brans, C. & Dicke, R. *Mach's Principle and a Relativistic Theory of Gravitation*. Physical Review **124**, 925-935 (1961) DOI=https://link.aps.org/doi/10.1103/PhysRev.124.925;

[58] Dvali, G., Gabadadze, G. & Porrati, M. *4D gravity on a brane in 5D Minkowski space*. Physics Letters B **485**, 208-214 (2000) DOI=http://dx.doi.org/10.1016/S0370-2693(00)00669-9;

[59] Nicolis, A., Rattazzi, R. & Trincherini, E. *Galileon as a local modification of gravity*. Physical Review D **79** (2009) DOI=https://link.aps.org/doi/10.1103/PhysRevD.79.064036;

[60] Marcondes, R., Landim, R., Costa, A., Wang, B. & Abdalla, E. *Analytic study of the effect of dark energy-dark matter interaction on the growth of structures*. Journal of Cosmology and Astroparticle Physics **2016**, 009-009 (2016) DOI=https://doi.org/10.1088/1475-7516/2016/12/009;

[61] Frusciante, N. & Perenon, L. *Effective field theory of dark energy: A review*. Physics Reports **857**, 1-63 (2020) DOI=https://doi.org/10.1016/j.physrep.2020.02.004;

[62] Weinberg, S. *Physical Processes in a Convergent Theory of the Weak and Electromagnetic Interactions*. Phys. Rev. Lett. **27**, 1688-1691 (1971) DOI=https://link.aps.org/doi/10.1103/PhysRevLett.27.1688;

[63] Kodama, H. & Sasaki, M. *Cosmological Perturbation Theory*. Progress of Theoretical Physics Supplement **78**, 1-166 (1984) DOI=https://doi.org/10.1143/PTPS.78.1;

[64] Arnowitt, R., Deser, S. & Misner, C. *Republication of: The dynamics of general relativity*. Gen Relativ Gravit **40**, 1997-2027 (2008) DOI=https://doi.org/10.1007/s10714-008-0661-1;

[65] Maldacena, J. *Non-gaussian features of primordial fluctuations in single field inflationary models*. Journal of High Energy Physics, **2003**, 013-013 (2003) DOI=https://doi.org/10.1088/1126-6708/2003/05/013;

[66] Ostrogradski, M., Memoires de l'Academie Imperiale des Science de Saint-Petersbourg. **4**, 385 (1850);

[67] Gleyzes, J., Langlois, D. & Vernizzi, F. *A unifying description of dark energy*. International Journal of Modern Physics D **23**, 1443010 (2014) DOI=http://dx.doi.org/10.1142/S021827181443010X;

[68] Gubitosi, G., Piazza, F. & Vernizzi, F. *The effective field theory of dark energy*. Journal of Cosmology and Astroparticle Physics **2013**, 032-032 (2013) DOI=http://dx.doi.org/10.1088/1475-7516/2013/02/032;

[69] Bloomfield, J., Flanagan, É., Park, M. & Watson, S. *Dark energy or modified gravity? An effective field theory approach*. Journal of Cosmology and Astroparticle Physics **2013**, 010-010 (2013) DOI=http://dx.doi.org/10.1088/1475-7516/2013/08/010;

[70] Bloomfield, J. *A simplified approach to general scalar-tensor theories. Journal of Cosmology and Astroparticle Physics* **2013**, 044-044 (2013) DOI=http://dx.doi.org/10.1088/1475-7516/2013/12/044;

[71] Abbott, B. *et al. GW170817: Observation of Gravitational Waves from a Binary Neutron Star Inspiral*. Physical Review Letters **119** (2017) DOI=http://dx.doi.org/10.1103/PhysRevLett.119.161101;

[72] Abbott, B. *et al. Gravitational Waves and Gamma-Rays from a Binary Neutron Star Merger: GW170817 and GRB 170817A*. The Astrophysical Journal **848** L13 (2017) DOI=http://dx.doi.org/10.3847/2041-8213/aa920c;

[73] Abbott, B. *et al. Multi-messenger Observations of a Binary Neutron Star Merger*. The Astrophysical Journal **848** L12 (2017) DOI=http://dx.doi.org/10.3847/2041-8213/aa91c9;

[74] Baker, T., Bellini, E., Ferreira, P., Lagos, M., Noller, J. & Sawicki, I. *Strong Constraints on Cosmological Gravity from GW170817 and GRB 170817A*. Physical Review Letters **119** (2017) DOI=http://dx.doi.org/10.1103/PhysRevLett.119.251301;

[75] Creminelli, P. & Vernizzi, F. *Dark Energy after GW170817 and GRB170817A*. Physical Review Letters **119** (2017) DOI=http://dx.doi.org/10.1103/PhysRevLett.119.251302;

[76] de Rham, C. & Melville, S. *Gravitational Rainbows: LIGO and Dark Energy at its Cutoff*. Physical Review Letters **121** (2018) DOI=http://dx.doi.org/10.1103/PhysRevLett.121.221101;

[77] Noller, J. & Nicola, A. *Cosmological parameter constraints for Horndeski scalar-tensor gravity*. Physical Review D **99** (2019) DOI=http://dx.doi.org/10.1103/PhysRevD.99.103502;

[78] Gleyzes, J. *Parametrizing modified gravity for cosmological surveys*. Physical Review D **96** (2017) DOI=http://dx.doi.org/10.1103/PhysRevD.96.063516;

[79] Denissenya, M. & Linder, E. *Gravity's islands: parametrizing Horndeski stability*. Journal of Cosmology and Astroparticle Physics **2018**, 010-010 (2018) DOI=http://dx.doi.org/10.1088/1475-7516/2018/11/010;

[80] Lombriser, L. *et al. Inherently stable effective field theory for dark energy and modified gravity.* Journal of Cosmology and Astroparticle Physics **2019**, 041-041 (2019) DOI=http://dx.doi.org/10.1088/1475-7516/2019/01/041;

[81] Lewis, A., Challinor, A. & Lasenby, A. *Efficient Computation of Cosmic Microwave Background Anisotropies in Closed Friedmann-Robertson-Walker Models.* The Astrophysical Journal **538**, 473-476 (2000) DOI=http://dx.doi.org/10.1086/309179;

[82] Lesgourgues, J. *The Cosmic Linear Anisotropy Solving System (CLASS) I: Overview.* (2011) ArXiv=https://arxiv.org/abs/1104.2932;

[83] Zumalacárregui, M., Bellini, E., Sawicki, I., Lesgourgues, J. & Ferreira, P. *hi_class: Horndeski in the Cosmic Linear Anisotropy Solving System.* Journal of Cosmology and Astroparticle Physics **2017**, 019-019 (2017) DOI=http://dx.doi.org/10.1088/1475-7516/2017/08/019;

[84] Burrage, C. & Sakstein, J. *Tests of chameleon gravity.* Living Reviews in Relativity **21** (2018) DOI=http://dx.doi.org/10.1007/s41114-018-0011-x;

[85] Babichev, E., Deffayet, C. & Ziour, R. *k-Mouflage gravity.* International Journal of Modern Physics D **18**, 2147-2154 (2009) DOI=http://dx.doi.org/10.1142/S0218271809016107;

[86] Vainshtein, A. *To the problem of nonvanishing gravitation mass.* Physics Letters B **39**, 393-394 (1972) DOI=https://doi.org/10.1016/0370-2693(72)90147-5;

[87] Babichev, E. & Deffayet, C. *An introduction to the Vainshtein mechanism.* Classical and Quantum Gravity **30** (2013) DOI=http://dx.doi.org/10.1088/0264-9381/30/18/184001;

[88] Alpher, R. & Herman, R. *Evolution of the Universe.* Nature **162**, 774-775 (1948) DOI=https://doi.org/10.1038/162774b0;

[89] Gamow, G. *The evolution of the Universe.* Nature **162**, 680-682 (1948) DOI=https://doi.org/10.1038/162680a0;

[90] Penzias, A. & Wilson, R. *A Measurement of Excess Antenna Temperature at 4080 Mc/s.* The Astrophysical Journal **142**, 419-421 (1965) DOI=https://doi.org/10.1086/148307;

[91] Dicke, R. *et al. Cosmic Black-Body Radiation.* The Astrophysical Journal **142**, 414-419 (1965) DOI=https://doi.org/10.1086/148306;

[92] Smoot, G. *et al. Structure in the COBE Differential Microwave Radiometer First-Year Maps*. Astrophysical Journal Letters **396**, L1-L5 (1992) DOI=https://doi.org/10.1086/186504;

[93] Hu, W. *CMB temperature and polarization anisotropy fundamentals*. Annals of Physics **303**, 203-225 (2003) DOI=http://dx.doi.org/10.1016/S0003-4916(02)00022-2;

[94] Peebles, P. *Recombination of the Primeval Plasma*. The Astrophysical Journal **153** (1968) Address=https://ui.adsabs.harvard.edu/abs/1968ApJ...153....1P;

[95] Rybicki, G. & Lightman, A. *Radiative Processes in Astrophysics*. Wiley-Vch, 400p. Revised edition, New York, NY (1991);

[96] Bartelmann, M. & Schneider, P. *Weak gravitational lensing*. Physics Reports **340**, 291-472 (2001) DOI=http://dx.doi.org/10.1016/S0370-1573(00)00082-X;

[97] Sunyaev, R. & Zeldovich, Y. *Small-scale fluctuations of relic radiation*. Astrophys Space Sci **7**, 3–19 (1970) DOI=https://doi.org/10.1007/BF00653471;

[98] Lewis, A. *Cosmological parameters from WMAP 5-year temperature maps*. Physical Review D **78** (2008) DOI=http://dx.doi.org/10.1103/PhysRevD.78.023002;

[99] Wise, J. *Cosmic reionisation*. Contemporary Physics **60**, 145-163 (2019) DOI=http://dx.doi.org/10.1080/00107514.2019.1631548;

[100] D. Lyth & A. Liddle. *The primordial density perturbation: Cosmology, inflation and the origin of structure*. Cambridge University Press, pp. 516, New York, NY (2009);

[101] Mukhanov. V. *Physical foundations of cosmology*. Cambridge University Press, pp. 442, New York, NY (2005);

[102] Tanabashi, M. *et al. Particle Data Group*. Phys. Rev. D **98**, 030001 (2018) and 2019 update;

[103] Sachs, R. & Wolfe, A. *Perturbations of a Cosmological Model and Angular Variations of the Microwave Background*. The Astrophysical Journal **147**, 73 (1967) DOI=http://dx.doi.org/10.1086/148982;

[104] Dodelson, S. *Modern Cosmology*. Academic Press. Massachusetts, USA (2003);

[105] Hu, W. & Sugiyama, N. *Small Scale Cosmological Perturbations: An Analytic Approach*. The Astrophysical Journal **471**, 542-570 (1996) DOI=http://dx.doi.org/10.1086/177989;

[106] Eisenstein, D. & Hu, W. *Baryonic Features in the Matter Transfer Function*. The Astrophysical Journal **496**, 605-614 (1998) DOI=http://dx.doi.org/10.1086/305424;

[107] Peebles, P. *The large-scale structure of the universe*. Princeton University Press. Princeton, N.J. (1980);

[108] Eisenstein, D. *et al. Detection of the Baryon Acoustic Peak in the Large?Scale Correlation Function of SDSS Luminous Red Galaxies*. The Astrophysical Journal **633** 560-574 (2005) DOI=http://dx.doi.org/10.1086/466512;

[109] Landy, S. & Szalay, A. *Bias and variance of angular correlation functions*. The Astrophysical Journal **412**, 64 (1993) DOI=http://dx.doi.org/10.1086/172900;

[110] Chevallier, M. & Polarski, D. *Accelerating Universes with Scaling Dark Matter*. International Journal of Modern Physics D **10**, 213-223 (2001) DOI=http://dx.doi.org/10.1142/S0218271801000822;

[111] Alcock, C. & Paczyński, B. *An evolution free test for non-zero cosmological constant*. Nature **281**, 358-359 (1979) DOI=https://doi.org/10.1038/281358a0;

[112] Percival, W. *et al. The 2dF Galaxy Redshift Survey: the power spectrum and the matter content of the Universe*. MNRAS **327**, 1297-1306 (2001) DOI=http://dx.doi.org/10.1046/j.1365-8711.2001.04827.x;

[113] Cole, S. *et al. The 2dF Galaxy Redshift Survey: power-spectrum analysis of the final data set and cosmological implications*. MNRAS **362**, 505-534 (2005) DOI=http://dx.doi.org/10.1111/j.1365-2966.2005.09318.x;

[114] Percival, W. *et al. Baryon acoustic oscillations in the Sloan Digital Sky Survey Data Release 7 galaxy sample*. MNRAS **401**, 2148-2168 (2010) DOI=http://dx.doi.org/10.1111/j.1365-2966.2009.15812.x;

[115] Blake, C. *et al. The WiggleZ Dark Energy Survey: testing the cosmological model with baryon acoustic oscillations at* $z = 0.6$. MNRAS **415**, 2892-2909 (2011) DOI=https://doi.org/10.1111/j.1365-2966.2011.19077.x;

[116] Beutler, F. *et al. The 6dF Galaxy Survey: baryon acoustic oscillations and the local Hubble constant*. MNRAS **416**, 3017-3032 (2011) DOI=https://doi.org/10.1111/j.1365-2966.2011.19250.x;

[117] Anderson, L. *et al. The clustering of galaxies in the SDSS-III Baryon Oscillation Spectroscopic Survey: baryon acoustic oscillations in the Data Release 9 spectroscopic galaxy*

sample. MNRAS **427**, 3435-3467 (2012) DOI=https://doi.org/10.1111/j.1365-2966.2012.22066.x;

[118] Pritchard, R. & Loeb, A. *21 cm cosmology in the 21st century*. Reports on Progress in Physics **75**, 086901 (2012) DOI=http://dx.doi.org/10.1088/0034-4885/75/8/086901;

[119] van de Hulst, H. *Radiogolven uit het wereldruim: II. Herkomst der radiogolvenRadiogolven uit het wereldruim: II. Herkomst der radiogolvenRadio waves from space*. Nederlandsch Tijdschrift voor Natuurkunde **11**, 210-221 (1945) https://ui.adsabs.harvard.edu/abs/1945NTvN...11..210V;

[120] Ewen, H. & Purcell, E. *Observation of a Line in the Galactic Radio Spectrum: Radiation from Galactic Hydrogen at 1,420 Mc./sec*. Nature **168**, 356 (1951) DOI=https://doi.org/10.1038/168356a0;

[121] Bharadwaj, S., Nath, B. & Sethi, S. *Using HI to probe large scale structures at z* 3. J Astrophys Astron **22**, 21-34 (2001) DOI=https://doi.org/10.1007/BF02933588;

[122] Battye, R., Davies, R. & Weller, J. *Neutral hydrogen surveys for high-redshift galaxy clusters and protoclusters*. MNRAS **355**, 1339-1347 (2004) DOI=https://doi.org/10.1111/j.1365-2966.2004.08416.x;

[123] Chang, T.-C. *et al. Baryon Acoustic Oscillation Intensity Mapping of Dark Energy*. Phys. Rev. Lett. **100**, 091303 (2008) DOI=https://link.aps.org/doi/10.1103/PhysRevLett.100.091303;

[124] Villaescusa-Navarro, F. *et al. Modeling the neutral hydrogen distribution in the post-reionization Universe: intensity mapping*. Journal of Cosmology and Astroparticle Physics **2014**, 050-050 (2014) DOI=http://dx.doi.org/10.1088/1475-7516/2014/09/050;

[125] Battye, R. *et al. HI intensity mapping: a single dish approach*. MNRAS **434**, 1239-1256 (2013) DOI=https://doi.org/10.1093/mnras/stt1082;

[126] Mo, H., van den Bosch, F. & White, S. *Galaxy Formation and Evolution*. Cambridge University Press, New York, USA (2010);

[127] Villaescusa-Navarro, F. *et al. Ingredients for 21 cm Intensity Mapping*. The Astrophysical Journal **866**, 135 (2018) DOI=http://dx.doi.org/10.3847/1538-4357/aadba0;

[128] Spinelli, M. *et al. The atomic hydrogen content of the post-reionization Universe*. MNRAS **493**, 5434-5455 (2020) DOI=https://doi.org/10.1093/mnras/staa604;

[129] Kaiser, N. *Clustering in real space and in redshift space*. MNRAS **227**, 1-21 (1987) DOI=https://doi.org/10.1093/mnras/227.1.1;

[130] Jackson, J. *A Critique of Rees's Theory of Primordial Gravitational Radiation*. MNRAS **156**, 1P-5P (1972) DOI=https://doi.org/10.1093/mnras/156.1.1P;

[131] Reid, B. *et al. The clustering of galaxies in the SDSS-III Baryon Oscillation Spectroscopic Survey: measurements of the growth of structure and expansion rate at z = 0.57 from anisotropic clustering*. MNRAS **426**, 2719–2737 (2012) DOI=https://doi.org/10.1111/j.1365-2966.2012.21779.x;

[132] Fisher, K., Scharf, C. & Lahav, O. *A spherical harmonic approach to redshift distortion and a measurement of Omega(0) from the 1.2-Jy IRAS Redshift Survey*. MNRAS **266**, 219–226 (1994) DOI=https://doi.org/10.1093/mnras/266.1.219;

[133] Song, Y.-S. & Percival, W. *Reconstructing the history of structure formation using redshift distortions*. Journal of Cosmology and Astroparticle Physics **2009**, 004–004 (2009) DOI=http://dx.doi.org/10.1088/1475-7516/2009/10/004;

[134] Lewis, A., Challinor, A. & Lasenby, A. *Efficient Computation of Cosmic Microwave Background Anisotropies in Closed Friedmann-Robertson-Walker Models*. The Astrophysical Journal **538**, 473-476 (2000) DOI=http://dx.doi.org/10.1086/309179;

[135] Maartens, R. *et al. Overview of Cosmology with the SKA*. PoS **AASKA14**, 016 (2015) DOI=https://doi.org/10.22323/1.215.0016;

[136] Bandura, K. *et al. Canadian Hydrogen Intensity Mapping Experiment (CHIME) pathfinder*. Ground-based and Airborne Telescopes V (2014) DOI=http://dx.doi.org/10.1117/12.2054950;

[137] Chen, X. *THE TIANLAI PROJECT: A 21CM COSMOLOGY EXPERIMENT*. International Journal of Modern Physics: Conference Series **12**, 256-263 (2012) DOI=https://doi.org/10.1142/S2010194512006459;

[138] Smoot, G. & Debono, I. *21 cm intensity mapping with the Five hundred metre Aperture Spherical Telescope*. Astronomy & Astrophysics **597**, A136 (2017) DOI=https://doi.org/10.1051/0004-6361/201526794;

[139] Newburgh, L. *et al. HIRAX: a probe of dark energy and radio transients*. Ground-based and Airborne Telescopes VI (2016) DOI=http://dx.doi.org/10.1117/12.2234286;

[140] Coles, P. & Jones, B. *A lognormal model for the cosmological mass distribution*. MNRAS **248**, 1-13 (1991) DOI=https://doi.org/10.1093/mnras/248.1.1;

[141] Hilbert, S., Hartlap, J. & Schneider, P. *Cosmic shear covariance: the log-normal approximation*. Astronomy & Astrophysics **536**, A85 (2011) DOI=https://doi.org/10.1051/0004-6361/201117294;

[142] Taruya, A. *et al. Lognormal Property of Weak-Lensing Fields*. The Astrophysical Journal **571**, 638-653 (2002) DOI=https://doi.org/10.1086/340048;

[143] Trotta, R. *Bayes in the sky: Bayesian inference and model selection in cosmology*. Contemporary Physics **49**, 71-104 (2008) DOI=http://dx.doi.org/10.1080/00107510802066753;

[144] Bayes, T. *An essay towards solving a problem in the doctrine of chances*. Royal Society **53**, 370–418 (1763) DOI=http://doi.org/10.1098/rstl.1763.0053;

[145] Riemer-Sørensen, S. *Statistics and model selection in cosmology*. Lecture notes, CANTATA Cost-Action Summer School (2017). Available in https://www.icg.port.ac.uk/cantata-summer-school-2017-corfu/, accessed in 24th March 2021;

[146] Heavens, A. *et al. No Evidence for Extensions to the Standard Cosmological Model*. Physical Review Letters **119** (2017) DOI=10.1103/physrevlett.119.101301;

[147] Vardanyan, M. *et al. Applications of Bayesian model averaging to the curvature and size of the Universe*. MNRAS: Letters **413**, L91-L95 (2011) DOI=https://doi.org/10.1111/j.1745-3933.2011.01040;

[148] Liddle, A. *et al. Present and future evidence for evolving dark energy*. Physical Review D **74** (2006) DOI=10.1103/physrevd.74.123506;

[149] Ghosh, J. *et al. An Introduction to Bayesian Analysis*. Springer, New York, (2006);

[150] Zyla, P. *et al. Particle Data Group*. Prog. Theor. Exp. Phys. **2020**, 083C01 (2020);

[151] Gamerman, D. & Lopes, H. *Markov Chain Monte Carlo: Stochastic Simulation for Bayesian Inference*. Chapman & Hall/CRC 2nd Ed., USA, (2006);

[152] Metropolis, N. *et al. Equation of State Calculations by Fast Computing Machines*. J. Chem. Phys. **21** 1087-1092 (1953) DOI=https://doi.org/10.1063/1.1699114;

[153] Hastings, W. *Monte Carlo sampling methods using Markov chains and their applications*. Biometrika **57** 97-109 (1970) DOI=https://doi.org/10.1093/biomet/57.1.97;

[154] Smith, A. & Roberts, G. *Bayesian Computation Via the Gibbs Sampler and Related Markov Chain Monte Carlo Methods*. J. R. Statist. Soc. B **55** 3-23 (1993);

[155] Hanson, K. *Markov Chain Monte Carlo posterior sampling with the Hamiltonian method*. M. Sonka and K. M. Hanson (Eds) Medical Imaging: Image Processing. **4322**, Proc. SPIE, 456-467 (2001);

[156] Skilling, J. *Bayesian Inference and maximum entropy methods in science and engineering*. Amer. Inst. Phys. Conference Proc. **735** 395 (2004);

[157] Feroz, F. & Hobson, M. *Multimodal nested sampling: an efficient and robust alternative to Markov Chain Monte Carlo methods for astronomical data analyses*. MNRAS **384**, 449-463 (2008) DOI=https://doi.org/10.1111/j.1365-2966.2007.12353.x;

[158] Rollins, R. *Chemical and Statistical Models of the Interstellar Medium and Star-Forming Regions*. University College London, London, UK (2015);

[159] Lewis, A. & Bridle, S. *Cosmological parameters from CMB and other data: A Monte Carlo approach*. Physical Review D **66** (2002) DOI=http://dx.doi.org/10.1103/PhysRevD.66.103511;

[160] Hinshaw, G. *et al. Five-Year Wilkinson Microwave Anisotropy Probe (WMAP) Observations: Data Processing, Sky Maps, and Basic Results*. The Astrophysical Journal Supplement Series **180**, 225-245 (2009) DOI=http://dx.doi.org/10.1088/0067-0049/180/2/225;

[161] Bellini, E. *et al. Constraints on deviations from ΛCDM within Horndeski gravity*. Journal of Cosmology and Astroparticle Physics **2016**, 053-053 (2016) DOI=http://dx.doi.org/10.1088/1475-7516/2016/02/053;

[162] Abdalla, F. & Rawlings, S. *Determining neutrino properties using future galaxy redshift surveys*. MNRAS **381**, 1313-1328 (2007) DOI=http://dx.doi.org/10.1111/j.1365-2966.2007.11919.x;

[163] de Rham, C. *et al. Positivity bounds for scalar field theories*. Physical Review D **96** (2017) DOI=http://dx.doi.org/10.1103/PhysRevD.96.081702;

[164] Alonso, D. *et al. Observational future of cosmological scalar-tensor theories*. Physical Review D **95** (2017) DOI=http://dx.doi.org/10.1103/PhysRevD.95.063502;

[165] Hu, B. *et al. Effective field theory of cosmic acceleration: An implementation in CAMB*. Physical Review D **89** (2014) DOI=http://dx.doi.org/10.1103/PhysRevD.89.103530;